Dissertation

submitted to the

Combined Faculty of Mathematics, Engineering and Natural Sciences

of Heidelberg University, Germany

for the degree of

Doctor of Natural Sciences

Put forward by

Olesia Bezrodnova

born in: Pskov, Russia

Oral examination: June 23, 2025

High-precision Penning-trap Measurement of the Helium-3 Atomic Mass

Referees: Prof. Dr. Klaus Blaum

Priv. Doz. Dr. Teresa Marrodán Undagoitia

Abstract

This work presents a high-precision atomic mass measurement of helium-3. The measurement was performed using the Penning-trap mass spectrometer LIONTRAP, where the cyclotron frequency of the helium ion was measured relative to that of a carbon ion, which serves as a standard in atomic mass units. With a relative uncertainty of 1.2×10^{-11}, this result represents the most precise mass measurement of helium-3 in atomic mass units to date. It contributes to resolving the "Light Ion Mass Puzzle" - inconsistencies in the measured masses of light nuclei, namely the proton, deuteron, and helium-3, reported by different Penning-trap mass spectrometers in the past. By demonstrating consistency between the results from LIONTRAP and those from the group at Florida State University, while simultaneously highlighting a discrepancy with the results from the University of Washington (UW), this work suggests that the earlier Penning-trap measurements by the UW group may have underestimated the uncertainty in their results. Consequently, confidence in Penning-trap measurements of light ion masses - fundamental constants used to test the validity of the Standard Model - is restored.

During the course of this work, the experimental setup was upgraded to allow for the production of helium-3 ions and an improved detection system. Additionally, a new analysis approach was introduced, which effectively suppresses the dominant systematic effect observed in previous LIONTRAP measurements, the lineshape effect, by a factor of more than 100. Furthermore, a phase-sensitive method for measuring the axial frequency has been developed, showing promising potential for improving the statistical precision achievable in Penning-trap experiments in general.

The measurement presented in this thesis concludes a series of studies on light ions conducted at LIONTRAP, and the experimental setup is now being repurposed for lepton symmetry tests at MPIK.

Zusammenfassung

Diese Arbeit präsentiert eine Messung der atomaren Masse von Helium-3. Die Messung wurde mit dem Penningfallen-Massenspektrometer LIONTRAP durchgeführt, wobei die Zyklotronfrequenz des Helium-Ions relativ zu der eines Kohlenstoff-Ions gemessen wurde, welches als Standard in atomaren Masseneinheiten dient. Mit einer relativen Unsicherheit von 1.2×10^{-11} stellt dieses Ergebnis die bislang genaueste Massenmessung von Helium-3 in atomaren Masseneinheiten dar.

Es trägt zur Lösung des "Light Ion Mass Puzzle" bei - Unstimmigkeiten in den gemessenen Massen leichter Atomkerne, nämlich des Protons, Deuterons und Helium-3, die in der Vergangenheit von verschiedenen Penningfallen-Massenspektrometer berichtet wurden. Durch die Übereinstimmung der Ergebnisse von LIONTRAP mit denen der Gruppe an der Florida State University und gleichzeitig die Aufdeckung einer Diskrepanz zu den Ergebnissen der University of Washington (UW) legt diese Arbeit nahe, dass frühere Penning-Fallen-Messungen der UW-Gruppe die Unsicherheit ihrer Ergebnisse möglicherweise unterschätzt haben. Folglich wird das Vertrauen in Penning-Fallen-Messungen leichter Ionenmassen - fundamentale Konstanten, die zur Überprüfung der Gültigkeit des Standardmodells verwendet werden - wiederhergestellt.

Im Verlauf dieser Arbeit wurde der experimentelle Aufbau erweitert, um die Produktion von Helium-3-Ionen zu ermöglichen und es wurde ein verbessertes Detektionssystem entwickelt und aufgebaut. Zudem wurde ein neuer Analyseansatz eingeführt, der den dominanten systematischen Effekt, den Linienformeffekt, der in früheren LIONTRAP-Messungen beobachtet wurde, um einen Faktor von mehr als 100 effektiv unterdrückt. Darüber hinaus wurde eine phasensensitive Methode zur Messung der axialen Frequenz entwickelt, die vielversprechendes Potenzial zur Verbesserung der statistischen Präzision in Penning-Fallen-Experimenten im Allgemeinen zeigt.

Die in dieser Dissertation vorgestellte Messung schließt eine Reihe von Untersuchungen zu leichten Ionen bei LIONTRAP ab, und der experimentelle Aufbau wird nun für Tests zur Leptonensymmetrie am MPIK umgewidmet.

Contents

Chapter 1

Introduction

Uncertainty, in the presence of vivid hopes and fears, is painful, but must be endured if we wish to live without the support of comforting fairy tales.

Bertrand Russell, *A History of Western Philosophy*

The atomic masses of the lightest nuclei, such as hydrogen and helium isotopes, as well as the neutron and electron, are considered fundamental physical constants [3]. These values are essential for testing the validity of our current understanding of fundamental physics as described by the Standard Model [4]. State-of-the-art mass measurements of the light ion masses with the highest precision are primarily achieved through single-ion measurements in a Penning trap [5]. In particular, mass ratio measurements performed by various Penning-trap mass spectrometers form an interconnected network of parameters, where new measurements continuously refine our understanding of fundamental interactions.

The LIONTRAP mass spectrometer was commissioned in 2015 to perform high-precision measurements of light ion masses. Since then, it has enabled high-precision determinations of the proton mass [6], the deuteron and HD molecule masses [7], and the α-particle mass [8]. In this work, I present the measurement of another helium isotope, helium-3 [1]. This measurement completes the series of mass determinations conducted within the LIONTRAP experiment, providing a conclusive consistency check for both the group's results and those of other experiments.

This chapter provides the general motivation for high-precision light ion mass measurements, with a particular focus on the discrepancies in literature values known as the "Light Ion Mass Puzzle". In Ch. 2, the fundamental principles of single-ion physics in a Penning trap are reviewed. Ch. 3 describes the experimental setup of LIONTRAP, including the construction of a new detection circuit developed for this

measurement campaign. Ch. 4 outlines the preparatory measurements preceding the mass determination, such as trap characterization and the minimization and analysis of trap imperfections. The following chapter (Ch. 5) introduces the phase-sensitive axial measurement technique developed during this work, aimed at overcoming the dominant systematic effects limiting our precision measurements. The measurement of the helium-3 atomic mass is detailed in Ch. 6, including an evaluation of systematic uncertainties and the limitations of this campaign. Finally, the implications of this measurement in the context of other high-precision mass determinations, along with the broader outlook of this research, are discussed in Ch. 7.

1.1 Precision Mass Measurements of Light Ions

Masses of light ions serve as fundamental input parameters for deriving various physical constants. A comprehensive review can be found in [4, 5]. Here, I present a few examples relevant to the mass measurements performed at LIONTRAP.

One such example involves the relationship between the Rydberg constant, R_∞, and the Rydberg constant of hydrogen, R_H, which is corrected for the finite mass of the hydrogen nucleus. They are related through the reduced mass of the electron in a hydrogen atom, where the proton-to-electron mass ratio enters [9].

Until recently, the relative atomic mass of the electron, $A_r(e)$, was determined from the ratio measurements of spin-precession and cyclotron frequency of the hydrogen-like $^{12}C^{5+}$ ion in a Penning trap [10, 11]. Advances in experimental techniques applied to lighter hydrogen-like ions, such as $^{4}He^{+}$, are expected to further reduce the uncertainty in the electron mass, provided that the ion's mass is determined with sufficient precision [12]. Such measurements are currently ongoing at the μTex Penning-trap experiment at MPIK [13].

Furthermore, the atomic mass of the neutron, m_n, can be determined from the mass of the deuteron m_d and the mass of the proton m_p, along with the neutron separation energy $S_n(d)$, which can be measured at neutron beam facilities [14]:

$$m_n = m_d - m_p + \frac{S_n(d)}{c^2}. \tag{1.1}$$

Additional motivations related to the mass of ^{3}He are discussed in the following sections.

1.2 Q-Value of the Tritium β-Decay: $\bar{\nu}_e$ Mass

Another important application of light masses concerns the determination of the neutrino rest mass. Although the Standard Model originally assumed neutrinos to be massless, solar neutrino oscillation experiments [15, 16] have demonstrated that neutrinos possess a finite mass. However, these oscillation experiments are sensitive only to the squared differences of neutrino mass eigenstates and do not provide information on the absolute mass scale.

Several methods exist for probing the absolute values of neutrino masses, including cosmological observations [17], studies of neutrinoless β-decay [18], and kinematic measurements of neutrino mass. The latter offer the most direct and least model-dependent approach, as it determines the neutrino rest mass by analyzing the kinematics of radioactive decay processes [19, 20].

Among these approaches are electron capture experiments [21] that are sensitive to $m(\nu_e)$ and studies of β-decay [22, 23, 24] that give limit on $m(\bar{\nu}_e)$. The KATRIN experiment (Karlsruhe Tritium Neutrino Experiment) has recently set the most stringent upper limit on the absolute antineutrino mass, constraining it to $m_\nu < 0.45$ eV/c^2 at a 90% confidence level [23]. In this experiment, a high-luminosity gaseous molecular tritium source is combined with a MAC-E filter spectrometer to measure the energy spectrum of decay electrons near the so-called endpoint, where the electron receives the maximum energy available in the decay $E_0 \approx 18.6$ keV [25]:

$$\mathrm{T}_2 \rightarrow {}^3\mathrm{HeT}^+ + e^- + \bar{\nu}_e. \tag{1.2}$$

The expected β-decay spectrum is shown in Fig. 1.1. The region near the endpoint of the spectrum is of particular interest, as the released energy is distributed among the electron's kinetic energy, the total neutrino energy, and the recoil energy of the daughter nucleus. A non-zero neutrino rest mass m_ν would distort the β-decay spectrum in this region. Additionally, the endpoint energy would be shifted to a lower value compared to the scenario in which the neutrino is massless.

At KATRIN, the primary constraint on the antineutrino rest mass is derived from the shape of the spectrum close to the endpoint. However, the endpoint energy also provides an essential consistency check, as the mass difference between T and ^{3}He can be used to predict the theoretical endpoint. In turn, the comparison of the measured and predicted endpoint energies, various systematic effects are considered, including the use of molecular rather than atomic tritium, rear-wall potentials, and plasma effects. Since these factors can also influence the spectral shape, verifying the accuracy of their modeling is of critical importance. At KATRIN, the impact on the experiment's response function is evaluated by calibration measurements with

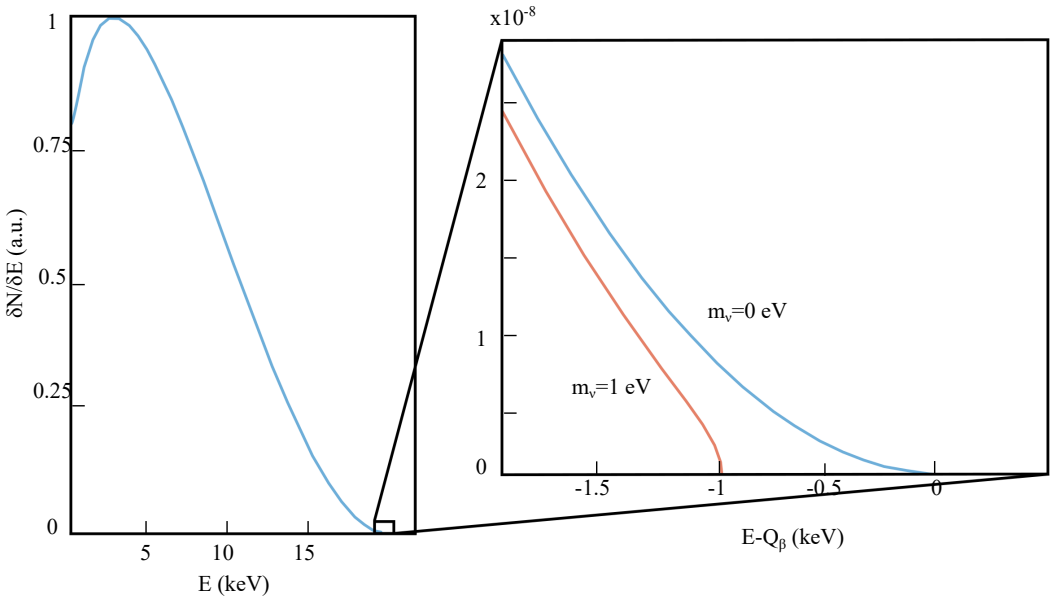

Figure 1.1. The electron energy spectrum of tritium β-decay for $Q \approx 18.6$ keV. Close to its endpoint, the maximum observable energy as well as the shape of the spectrum depend on the mass scale of neutrinos. The right zoom-in into the endpoint region of the spectrum illustrates the effect of a 1 eV neutrino mass indicated by the oranged line.

metastable ^{83m}Kr, since its spectrum consists of discrete mono-energetic lines and any shift or broadening of these lines reflects the spatial and temporal inhomogeneities in the plasma potential [26]. A Penning-trap measurement of the Q-value of the decay, given by the mass difference between T and ^{3}He, provides an independent cross-check of these systematic effects [4].

The mass difference $m(\mathrm{T}) - m(^3\mathrm{He})$ has been measured by the FSU group in the past [27, 28] by measuring the mass ratios of T and ^{3}He against molecular HD. By combining their result with the directly measured masses of the proton, deuteron, and electron, as well as the calculated molecular binding energy, the mass of ^{3}He in atomic mass units can be determined. However, these results revealed a significant discrepancy when compared with direct atomic mass measurements of $m\,(^3\mathrm{He})$ conducted by another experimental group. This inconsistency undermines the intended use of the mass difference obtained from Penning-trap experiments as a consistency check for KATRIN. A detailed discussion of this discrepancy follows in the next section.

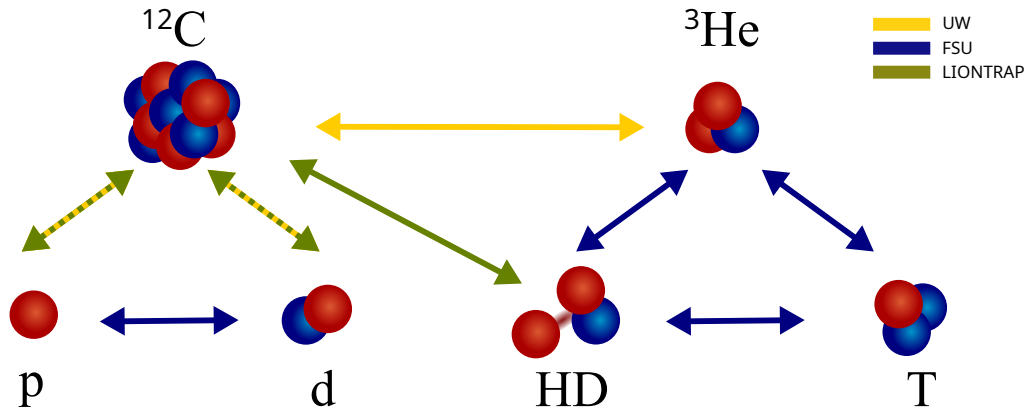

Figure 1.2. The puzzle of light-ion masses. The arrows indicate the cyclotron frequency ratios measured by various Penning-trap mass spectrometers prior to this work. Measurements using a carbon ion as reference are performed by the UW [29, 30] (yellow) and the LIONTRAP (green) [31, 6, 7] groups. The blue links are measured by the FSU group [27, 32, 33, 34, 28]. The comparison of $\Delta = m_p + m_d - m_{he}$ obtained from direct measurements against carbon and FSU results currently show a 4.8σ discrepancy, with the mass ratio of ^{3}He and ^{12}C being the primary candidate for the remaining inconsistency.

1.3 Light Ion Mass Puzzle

The masses of light nuclei, namely the proton (p), deuteron (d), triton (t), helion (he), and the alpha particle (α), are regarded as fundamental constants. The most precise mass measurements of these nuclei are conducted in Penning traps through the measurement of the ratio of cyclotron frequencies (R_{CF}) of two charged particles. This technique interconnects the masses and enables redundancy checks. Such tests have uncovered inconsistencies among the masses of ^{3}He obtained in various mass spectrometers in the past. This disagreement is recognized in the literature as the "Light Ion Mass Puzzle" [6, 7]. The discrepancy can be elucidated by examining $\Delta = m_p + m_d - m_{he}$, which represents the proton separation energy in the helion nucleus. Experimentally, this value can be obtained in two distinct ways, see Fig. 1.2. The masses m_p, m_d and m_{he} can be directly measured, using ^{12}C, the standard of atomic mass units (u), as a reference ion. Such measurements were conducted in the past by the group at the University of Washington (UW) [29, 30]. Another approach involves measuring the ratio of ^{3}He to HD^+ and utilizing the binding energy of the molecular ion HD^+ and the mass of the electron, both of which are known with sufficient precision [11]. Such measurements were carried out by the group at Florida State University (FSU) [27]. The comparison of the results from these two groups

showed a deviation at the 4.2σ (combined standard deviation) level: $\Delta_{\mathrm{UW}} - \Delta_{\mathrm{FSU}} = 860(210)$ pu. The identified discrepancy raised questions about the reliability of these values and motivated independent measurements. The LIONTRAP experiment was established to remeasure the masses of light ions relative to ^{12}C. We have measured the masses m_p [31, 6], m_d, and HD^+ [7] at this facility, showing consistency with the direct measurement of the mass difference between the molecular ion H_2^+ and d at the FSU facility [33, 34]. Additionally, LIONTRAP's measurements showed reasonable agreement with laser spectroscopy experiments that determine transition frequencies in the rovibrational spectrum of the molecular ion HD^+, providing the ratios of the involved masses [35, 36, 37, 38]. Prior to this work, due to the reduced uncertainty in the absolute mass values from the latest FSU [28] and LIONTRAP results [6, 7], the deviation in the value of Δ was 4.8σ: $\Delta_{^{12}\mathrm{C}} - \Delta_{\mathrm{FSU}} = 263(61)$ pu, with the primary candidate for the remaining deviation being the mass ratio between ^{3}He and ^{12}C.

While the mass of the α-particle does not directly contribute to the described puzzle, due to the persistent discrepancies between the LIONTRAP and UW groups, the mass of the ^{4}He nucleus was also measured at LIONTRAP [8]. This measurement revealed a 6.6σ deviation from the literature value [11], given by the measurement of the UW group [39]. This provided strong motivation to measure the mass ratio of ^{3}He to ^{12}C and thus to perform an independent check.

Chapter 2

Single Ion in a Penning Trap

The primary tool used in this thesis is the Penning trap. Such traps enable precision measurements on single ions, allowing for storage times on the order of months [40]. This chapter introduces the fundamental principles of trapped ion physics that are essential for understanding the measurements.

The Earnshaw's theorem states that the purely electrostatic or magnetostatic stable stationary confinement of charged particles in three dimensions is fundamentally impossible [41]. This result follows from Maxwell's equations [42], which imply the absence of a true three-dimensional potential extremum in a divergence-free field, allowing only the formation of saddle points.

However, stable three-dimensional confinement of charged particles can be achieved by superimposing a homogeneous magnetostatic field with a quadrupolar electrostatic potential. The concept of such a device was first described by Pierce in 1949 [43]. In 1989, Dehmelt was awarded the Nobel Prize for his pioneering work in atomic precision spectroscopy, which included the first experimental realization of such a trap in 1959 [44], that notably led to high-precision measurements of the g-factor of the free electron [45, 46]. Dehmelt also introduced the term "Penning trap" in recognition of F. M. Penning, whose work on radial particle confinement in an axial magnetic field contributed to the development of vacuum gauges, albeit without electrostatic trapping fields [47].

Today, Penning traps play a crucial role in high-precision measurements of fundamental particle and atomic properties, particularly in mass spectrometry and magnetic moment determinations [48, 49].

2.1 Ideal Penning Trap

In this section, the fundamental field configuration of an ideal Penning trap, which governs charged particle trajectories, is outlined [50]. In a homogeneous magnetic field $\vec{B} = B_0\vec{e}_z$ along the axial z-direction, a particle with charge q and velocity $\vec{v}$ is constrained to a circular orbit perpendicular to the magnetic field axis due to the Lorentz force,

$$\vec{F} = q(\vec{v} \times \vec{B}). \tag{2.1}$$

The angular frequency of this periodic motion for a particle with mass m is given by the free cyclotron frequency,

$$\omega_c = \frac{q}{m}B. \tag{2.2}$$

To achieve harmonic confinement in the z-direction, an electrostatic quadrupole potential is superimposed. An ideal quadrupolar potential can be realized using three hyperboloidal electrodes (see Fig. 2.1): a ring electrode and two endcap electrodes extending to infinity. The equation for a hyperboloid in cylindrical coordinates (z, r) is given by

$$\frac{r^2}{r_0^2} - \frac{z^2}{z_0^2} = \pm 1, \tag{2.3}$$

where the plus and minus signs correspond to the ring and endcap electrodes, respectively. Here, z_0 denotes half the distance between the endcaps, while r_0 is the inner radius of the ring, satisfying the relation $r_0 = \sqrt{2}z_0$ [51, 52].

The ideal quadrupolar electrostatic potential is given by

$$\Phi_{\text{ideal}}(r, z) = \frac{U_r C_2}{2d_{\text{char}}^2}\left(z^2 - \frac{r^2}{2}\right). \tag{2.4}$$

Here, U_r is the trapping voltage applied to the ring electrode, $r = \sqrt{x^2 + y^2}$ is the radial distance from the z-axis, and $d_{\text{char}} = \sqrt{\frac{1}{2}\left(z_0^2 + \frac{r_0^2}{2}\right)}$ is the characteristic trap dimension. The dimensionless coefficient C_2 quantifies the strength of the quadrupolar potential and depends on the electrode geometry.

2.1.1 Motion of the Particle

Here, the classical and non-relativistic motion of a single ion in an ideal Penning trap is formulated. The frequency shifts due to trap imperfections are considered perturbatively in Sec. 2.2 and relativistic shifts introduced in Sec. 2.4.

In the superposition of an electric and magnetic field, the equation of motion is governed by the total Lorentz force:

$$\vec{F} = q\left(\vec{E} + \vec{v} \times \vec{B}\right) = q\left(-\nabla\Phi + \vec{v} \times \vec{B}\right) = m\ddot{\vec{r}}. \tag{2.5}$$

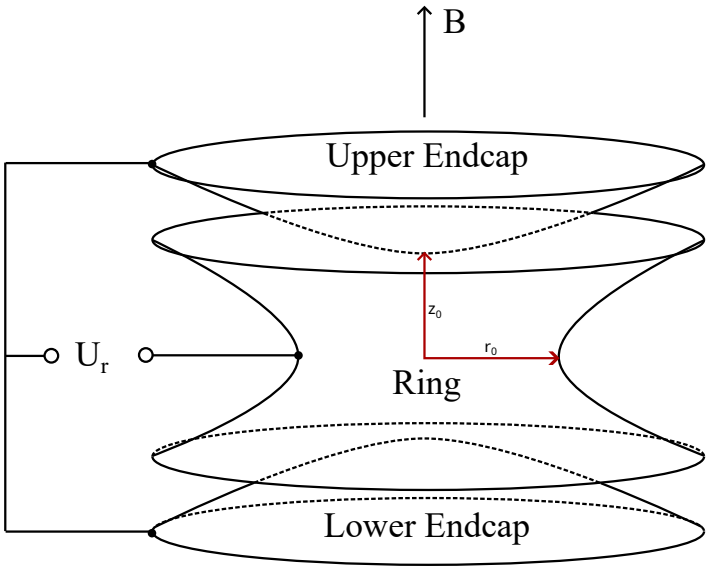

Figure 2.1. Sketch of the hyperboloid trap electrode structure. The inner radius of the ring electrode is denoted by r_0, and the distance from the trap center to the endcaps is z_0. The trapping voltage U_r is applied between the endcaps and the ring electrode, while the homogeneous magnetic field $\vec{B}$ is oriented along the axial direction.

From that, combined with Eq. (2.4), one can derive the classical equations of motion for a trapped particle:

$$\begin{pmatrix} \ddot{x} \\ \ddot{y} \\ \ddot{z} \end{pmatrix} = \frac{qB_0}{m} \begin{pmatrix} \dot{y} \\ -\dot{x} \\ 0 \end{pmatrix} + \frac{qU_r C_2}{2md_{\text{char}}^2} \begin{pmatrix} x \\ y \\ -2z \end{pmatrix}. \tag{2.6}$$

The solutions correspond to three independent harmonic motions. An illustration of the particle trajectories is shown in Fig. 2.2.

The axial oscillation of the charged particle between the trap endcaps is governed solely by the z-component of Eq. (2.4). In the radial direction, the free cyclotron frequency is altered due to the repulsive nature of Eq. (2.4), resulting in what is known as modified cyclotron motion. Additionally, a third type of motion emerges from an $\vec{E} \times \vec{B}$ drift in the radial plane, referred to as magnetron motion.

The eigenfrequencies of these motions are given by:

$$\text{Axial frequency:} \quad \omega_z = \sqrt{\frac{qC_2U_r}{md_{\text{char}}^2}}, \tag{2.7a}$$

$$\text{Modified cyclotron frequency} \quad \omega_+ = \frac{1}{2}\left(\omega_c + \sqrt{\omega_c^2 - 2\omega_z^2}\right), \tag{2.7b}$$

$$\text{Magnetron frequency} \quad \omega_- = \frac{1}{2}\left(\omega_c - \sqrt{\omega_c^2 - 2\omega_z^2}\right). \tag{2.7c}$$

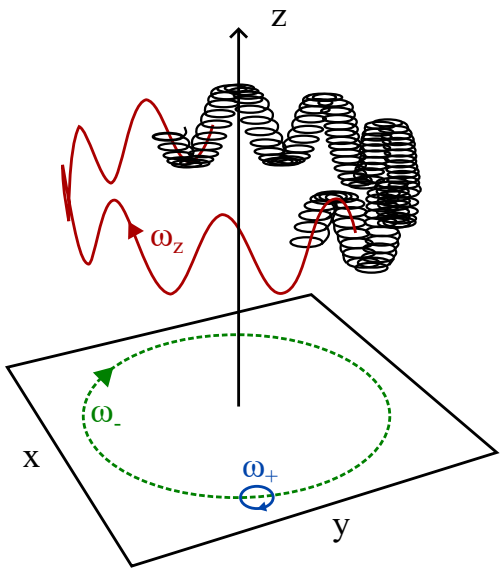

Figure 2.2. Sketch of the trajectory of a charged particle in an ideal Penning trap, illustrating its three independent eigenmotions. In the axial z-direction, the particle oscillates between the endcaps with the axial frequency ω_z (red). In the radial plane, two circular motions occur: the fast cyclotron motion with frequency ω_+ (blue) and the slow magnetron drift with frequency ω_- (green). The superposition of these eigenmotions results in a combined trajectory, shown by the black line.

The term under the square root in Eq. (2.7b) and Eq. (2.7c) must be real-valued to ensure bound solutions to the equations, thereby establishing the stability criterion for the trap:

$$\omega_c^2 - 2\omega_z^2 > 0 \quad \Rightarrow \quad B_0 > \sqrt{\frac{2mU_rC_2}{qd_{\text{char}}^2}}. \tag{2.8}$$

In a strong magnetic field and a relatively weak electric field, the eigenfrequencies follow the hierarchy

$$\omega_c > \omega_+ \gg \omega_z \gg \omega_-. \tag{2.9}$$

In an ideal Penning trap, the eigenfrequencies are related by

$$\omega_c = \omega_+ + \omega_-, \tag{2.10}$$

$$\omega_z^2 = 2\omega_+\omega_-, \tag{2.11}$$

$$\omega_c^2 = \omega_+^2 + \omega_z^2 + \omega_-^2. \tag{2.12}$$

Eq. (2.10) and Eq. (2.11) are valid only for an ideal Penning trap, whereas Eq. (2.12), known as the invariance theorem [50], holds even for certain deviations from the ideal trap characteristics, which will be discussed in detail in Sec. 2.2.

2.1.2 Energies of the Eigenmodes

The total energy of a spinless charged particle in the trap is defined as [50]:

$$E_{\text{tot}} = \underbrace{\frac{1}{2}m\omega_z^2\hat{z}^2}_{E_z(\text{pot,kin})} + \underbrace{\frac{1}{2}m\omega_+^2 r_+^2}_{E_+(\text{kin})} + \underbrace{-\frac{1}{2}m\omega_+\omega_- r_+^2}_{E_+(\text{pot})} + \underbrace{\frac{1}{2}m\omega_-^2 r_-^2}_{E_-(\text{kin})} + \underbrace{-\frac{1}{2}m\omega_+\omega_- r_-^2}_{E_-(\text{pot})}. \tag{2.13}$$

The energy associated with each eigenmode is then given by:

$$\text{Axial mode energy:} \quad E_z = \frac{1}{2}m\omega_z^2\hat{z}^2, \tag{2.14}$$

$$\text{Modified cyclotron mode energy:} \quad E_+ = \frac{1}{2}m\omega_+(\omega_+ - \omega_-)r_+^2 \approx \frac{1}{2}m\omega_+^2 r_+^2, \tag{2.15}$$

$$\text{Magnetron mode energy:} \quad E_- = -\frac{1}{2}m\omega_-(\omega_+ - \omega_-)r_-^2 \approx -\frac{1}{4}m\omega_z^2 r_-^2 \approx -\frac{1}{2}m\omega_+\omega_- r_-^2, \tag{2.16}$$

where $\hat{z}$, r_+, and r_- are the amplitudes of the corresponding motions.

The energy of the modified cyclotron mode is primarily kinetic, whereas the energy of the magnetron mode is predominantly potential, resulting in a negative magnetron energy. Since the electrostatic confining potential is radially repulsive, it pushes the ion outward, making the slow magnetron mode metastable. Consequently, an increase in the magnetron radius leads to a decrease in magnetron energy.

The total energy of the particle can also be expressed in quantum mechanical terms as the sum independent harmonic oscillators:

$$E_{\text{tot}} = \hbar|\omega_+|\left(n_+ + \frac{1}{2}\right) + \hbar|\omega_z|\left(n_z + \frac{1}{2}\right) - \hbar|\omega_-|\left(n_- + \frac{1}{2}\right), \tag{2.17}$$

where $\hbar$ is the reduced Planck constant, and n_k are the quantum numbers, typically greater than 10^5, resulting from the order of ion energies in the trap. This justifies the classical treatment of ion motion.

2.2 Penning Trap Imperfections

A real Penning trap deviates from the ideal case due to several imperfections:

- **Geometric imperfections**: Unlike ideal hyperbolic electrodes, real electrodes are truncated and finite in size. Hyperbolic geometries restrict access to the trap centre, necessitating modifications such as cylindrical electrodes, as used in our experiment (see Ch. 3). Additionally, machining tolerances and segmented electrodes for excitation introduce further deviations.

- **Electric field instability**: Applied voltages fluctuate due to limitations in the voltage source ($\delta U/U \sim 10^{-7}$ in about an hour timescale in our setup). Deviations from the ideal geometry introduce higher-order multipole components and potential ellipticity, leading to asymmetric radial fields. Patch potentials arise from surface irregularities, gas deposits, dielectric charging, and material impurities, causing non-uniform electrostatic fields.

- **Magnetic field instability**: The superconducting magnet typically undergoes slow flux decay over the course of several years. Local disturbances arise from magnetized materials, whose magnetization is influenced by fluctuations in pressure and temperature. Changes in liquid helium and nitrogen levels thereby affect field stability.

These imperfections cause oscillation frequencies to depend on ion motion amplitudes, leading to systematic frequency shifts that must be carefully characterised. The following sections discuss these effects in detail.

2.2.1 Electrostatic Anharmonicity

A ring and two endcaps generate a basic quadrupole potential in a simple ion trap, but this configuration is limited in its ability to minimize higher-order electrostatic anharmonicities, which is required for high-precision measurements. The quadrupole potential can be refined by incorporating correction electrodes and optimizing the lengths and length-to-radius ratios of all electrodes.

The general form of the electrostatic potential at the trap center [53], as described in Eq. (2.4), is given by:

$$\Phi(r,z) = \frac{U_r}{2}\sum_{n=0}^{\infty}\frac{C_n}{d_{\text{char}}^n}\sum_{k=0}^{n/2}(-4)^{-k}\frac{n!}{(n-2k)!(k!)^2}z^{n-2k}r^{2k}, \tag{2.18}$$

where r and z are the cylindrical coordinates. The series expansion of electric potential gives:

$$\begin{aligned}\Phi(z,r) = \frac{U_r}{2}\Bigg[&C_0 + \frac{C_1 z}{d_{\text{char}}} + \frac{C_2}{d_{\text{char}}^2}\left(z^2 - \frac{r^2}{2}\right)\\ &+ \frac{C_3}{d_{\text{char}}^3}\left(z^3 - \frac{3}{2}zr^2\right) + \frac{C_4}{d_{\text{char}}^4}\left(z^4 - 3z^2r^2 + \frac{3}{8}r^4\right)\\ &+ \frac{C_5}{d_{\text{char}}^5}\left(z^5 - 5z^3r^2 + \frac{15}{8}zr^4\right)\\ &+ \frac{C_6}{d_{\text{char}}^6}\left(z^6 - \frac{15}{2}z^4r^2 + \frac{45}{8}z^2r^4 - \frac{5}{16}r^6\right) + \dots\Bigg].\end{aligned} \tag{2.19}$$

The anharmonicity of the electrostatic potential, given by coefficients C_n ($n \neq 2$), arises from both even and odd C_n terms, the most relevant of which are considered below.

The first coefficient C_0 is an unobservable constant that does not influence the eigenmotions of a trapped particle. The most important electrostatic field imperfections arise from even-order terms C_4 and C_6. The corresponding frequency shifts to the axial eigenmotion are given by [54]:

$$\frac{\Delta\omega_z}{\omega_z}\{C_4\} = \frac{C_4}{C_2}\frac{3}{4d_{\text{char}}^2}\left(z^2 - 2r_+^2 - 2r_-^2\right), \tag{2.20}$$

$$\frac{\Delta\omega_z}{\omega_z}\{C_6\} = \frac{C_6}{C_2}\frac{15}{16d_{\text{char}}^4}\left(z^4 + 3r_+^4 + 3r_-^4 - 6r_+^2z^2 - 6r_-^2z^2 + 12r_+^2r_-^2\right). \tag{2.21}$$

The corresponding shift in radial frequencies are:

$$\Delta\omega_\pm\{C_4\} = \mp\frac{C_4}{C_2}\frac{3}{2d_{\text{char}}^2}\frac{\omega_+\omega_-}{\omega_+ - \omega_-}\left(2z^2 - r_\pm^2 - 2r_\mp^2\right), \tag{2.22}$$

$$\Delta\omega_\pm\{C_6\} = \mp\frac{C_6}{C_2}\frac{15}{8d_{\text{char}}^4}\frac{\omega_+\omega_-}{\omega_+ - \omega_-}\left(3z^4 + r_\pm^4 + 3r_\mp^4 - 6r_\pm^2z^2 - 12r_\mp^2z^2 + 6r_+^2r_-^2\right). \tag{2.23}$$

The ratios of the anharmonicity coefficients C_4, C_6 and C_2 therefore determine the overall strength of the frequency shifts (assuming odd-order C_n coefficients to be null). In practice, the coefficients C_4 and C_6 can be minimised by tracking the shift of the axial frequency $\Delta\omega_z$ after excitation of the magnetron motion on various radii r_-. The optimisation procedure is described in detail in Sec. 4.2.1. The minimised coefficients are sufficiently small ($C_4 \propto 10^{-6}$, $C_6 \propto 10^{-4}$) and the effect on the cyclotron frequency ratio, measured in our trap, becomes almost negligible (see Tab. 6.5). The higher-even order terms, such as C_8, C_{10}, ..., are small due to carefully optimised trap parameters, such as electrode lengths [55], and corresponding shifts in the eigenfrequencies are negligible.

Due to the axial symmetry of the electrostatic trap potential, the odd-order coefficients are often considered negligible. However, due to various trap imperfections, e.g. limited machining tolerances of the electrodes or surface contamination and patch potentials on the electrode walls, an asymmetry in the potential can arise and odd orders on the electrostatic potential need to be considered. Besides, asymmetric voltages can be intentionally applied to shift the ion position in the trap in a controlled way. The first odd-order term C_1 adds a constant force term in the axial equations of motion, which leads to a constant offset of the equilibrium position of the axial oscillation with no shift in ion's frequency:

$$\Delta z\{C_1\} = -\frac{C_1 d_{char}}{2C_2}. \tag{2.24}$$

In the case of the next leading order odd anharmonicity coefficient C_3, the potential term (Eq. (2.19)) also includes radial dependencies. The force components for the radial eigenmotions are proportional to the combination zr, which would only lead to frequency shifts for resonant interaction between the axial and radial modes. As these frequencies are well-separated, this effect does not occur. For the axial motion, however, the shift of the equilibrium position occurs depending on the motional amplitudes:

$$\Delta z\{C_3\} = \frac{3}{4}\frac{C_3}{C_2 d_{\text{char}}}\left(r_\pm^2 - z^2\right). \tag{2.25}$$

The electrostatic potential therefore has to be developed around the new equilibrium position. A series expansion of the potential around the new equilibrium of motion gives the relative frequency shift:

$$\frac{\Delta\omega_z}{\omega_z}\{C_3\} \approx -\frac{15}{16}\frac{C_3^2}{C_2^2 d_{\text{char}}^2}\hat{z}^2 + \frac{9}{8}\frac{C_3^2}{C_2^2 d_{\text{char}}^2}r_\pm^2. \tag{2.26}$$

It is notable that the scaling of the axial frequency shift due to C_3^2 for the radial amplitudes $r_\pm$ is similar to that of the even coefficient C_4 (Eq. (2.20)). The trap optimization process, described in Ch. 4.2.1, where the axial frequency shifts is measured as a function of r_-^2 , therefore, doesn't strictly lead to $C_4 \approx 0$, but rather a combination of C_4 and C_3 (from Eq. (2.20) and Eq. (2.26)):

$$C_4 = \frac{3}{4}\frac{C_3^2}{C_2}. \tag{2.27}$$

The frequency shifts from C_4 and C_3 must, therefore, cancel each other out or both be nulled. The natural size of C_3 in our trap is $\sim 10^{-3}$, given the electrode length tolerances and trap size. This leads into a C_4 in the range of $10^{-6} - 10^{-5}$ after the optimization process. The coefficient C_3 can be independently estimated from a dedicated measurement, where the shift in the axial frequency for the cold particle $(z, r_\pm \approx 0)$ is measured by applying an asymmetry of trapping potential by settings an offset of opposite sign on inner correction electrodes of the trap. The measurement is described in Sec. 4.2.2. It confirms our estimation of the C_3 coefficient on the basis of the trap size and mechanical tolerances of the electrodes.

Although only in the next order, other combinations of anharmonic coefficients of the electrostatic potential can also produce frequency shifts. Even-odd C_4C_3, even-even C_4C_6, and odd-odd C_3C_5 cross-terms and corresponding frequency shifts are further discussed in [56, 57]. Additionaly, a combination of electrostatic and magnetostatic imperfections leads to shifts and is considered in Sec. 2.2.3.

2.2.2 Magnetostatic Inhomogeneity

The magnetic field, expanded as a Legendre series in cylindrical coordinates, is given by

$$\begin{aligned} B(z,r) = B_0\hat{e}_z + B_1\left(z\hat{e}_z - \frac{r}{2}\hat{e}_r\right) + B_2\left((z^2 - \frac{r^2}{2})\hat{e}_z - zr\hat{e}_r\right) \\ + B_3\left(\left(z^3 - \frac{3}{2}zr^2\right)\hat{e}_z + \left(-\frac{3}{2}z^2r + \frac{3}{8}r^3\right)\hat{e}_r\right) \\ + B_4\left(\left(z^4 - 3z^2r^2 + \frac{3}{8}r^4\right)\hat{e}_z + \left(-2z^3r + \frac{3}{2}zr^3\right)\hat{e}_r\right) + \dots \end{aligned} \tag{2.28}$$

where $\hat{e}_z$ and $\hat{e}_r$ are unit vectors in the axial and radial directions, respectively. The strong axial field component generally suppresses the radial component. However, the dependence of the axial magnetic field on both axial and radial coordinates results in frequency shifts.

An ion undergoing circular motion (magnetron and cyclotron modes) in a plane perpendicular to the magnetic field is analogous to an electric current passing through a circular coil:

$$I = \frac{q}{t} = q\frac{\omega_\pm}{2\pi}. \tag{2.29}$$

This motion generates an orbital magnetic moment:

$$|\mu_z^{(\pm)}| = I\pi r_\pm^2 \quad \Rightarrow \quad \mu_z^{(\pm)} = -\frac{q}{2}\omega_\pm r_\pm^2. \tag{2.30}$$

The corresponding potential energy is given by:

$$U_{\text{mag}} = -\mu_z^{(\pm)} \cdot \vec{B}. \tag{2.31}$$

This leads to an additional force in the z-direction as the ion seeks to minimize its total energy:

$$F_z^{(\mu)} = -\frac{\partial U_{\text{mag}}}{\partial z} = \mu_z^{(\pm)}\frac{\partial B}{\partial z}. \tag{2.32}$$

The resulting equation of axial motion is:

$$\ddot{z} + \omega_z^2 z - \frac{\mu_z^{(\pm)}}{m}\frac{\partial B}{\partial z} = 0. \tag{2.33}$$

For a homogeneous magnetic field, the derivative term vanishes, and no additional force acts in the axial direction. The dominant magnetic field perturbations arise from the lower-order terms, specifically linear B_1 and quadratic B_2.

Unlike in the case of the electric imperfections, there is no reason to expect the low odd-order B coefficients to be naturally small. Considering the inhomogeneity B_1, the equation of motion simplifies to:

$$\ddot{z} + \omega_z^2 z - \frac{\mu_z^{(\pm)}}{m}B_1 = 0. \tag{2.34}$$

This additional term results in a shift of the equilibrium position:

$$\Delta z = \frac{\mu_z B_1}{m\omega_z^2} = -\frac{\omega_c \omega_\pm}{2\omega_z^2}\frac{B_1}{B_0} r_\pm^2. \tag{2.35}$$

At the displaced equilibrium position, the ion experiences a different magnetic field, leading to a shift in the radial frequencies. The magnetic moment associated with the modified cyclotron mode results in a relative shift in the magnetic field:

$$\frac{\Delta B}{B} \simeq \frac{B_1}{B_0}\Delta z = \frac{\Delta\omega_+}{\omega_+}, \tag{2.36}$$

$$\frac{\Delta\omega_+}{\omega_+} = -\frac{\omega_c \omega_+}{2\omega_z^2}\left(\frac{B_1}{B_0}\right)^2 r_+^2. \tag{2.37}$$

Similar to the case of electrostatic anharmonicity coefficients, odd-order magnetic inhomogeneity terms induce frequency shifts only at second order.

The next relevant magnetic inhomogeneity term is the even coefficient B_2, which modifies the equation of motion as:

$$\ddot{z} + \omega_z^2 z - \frac{\mu_z^{(\pm)}}{m} 2B_2 z = 0. \tag{2.38}$$

This additional term combines with the electrostatic force, resulting in an axial frequency shift given by:

$$|\Delta\omega_z| = \frac{\mu_z^{(\pm)} B_2}{\omega_z m}. \tag{2.39}$$

The corresponding relative axial frequency shift is:

$$\frac{\Delta\omega_z}{\omega_z} = \frac{\omega_+ + \omega_-}{\omega_+\omega_-}\frac{B_2}{4B_0}\left(r_-^2\omega_- + r_+^2\omega_+\right). \tag{2.40}$$

Similarly, the relative shifts in the modified cyclotron and magnetron frequencies are:

$$\frac{\Delta\omega_+}{\omega_+} = \frac{\omega_+ + \omega_-}{\omega_+ - \omega_-}\frac{B_2}{2B_0}\left(\hat{z}^2 - r_+^2 - r_-^2\left(1 + \frac{\omega_-}{\omega_+}\right)\right), \tag{2.41}$$

$$\frac{\Delta\omega_-}{\omega_-} = -\frac{\omega_+ + \omega_-}{\omega_+ - \omega_-}\frac{B_2}{2B_0}\left(\hat{z}^2 - r_-^2 - r_+^2\left(1 + \frac{\omega_+}{\omega_-}\right)\right). \tag{2.42}$$

A superconducting shim coil surrounding the trap chamber is used to minimize B_2 *in situ* [58]. The coefficient B_2 can be determined by studying the axial frequency shift as a function of various modified cyclotron radii r_+, as discussed in Sec. 4.3.2.

2.2.3 Combined Effects

Apart from the purely electrostatic and magnetostatic imperfections described in previous sections, a combination of these effects can cause frequency shifts. Due to the similarity in the scaling of the associated frequency shifts with motional amplitudes, their combination often poses a limit on the trap optimization process, where these imperfections are minimized.

Considering $r_+ \gg r_-, r_z$, the combination of odd-order coefficients of the electric and magnetic field imperfections C_3 and B_1 lead to a following shift in the axial frequency [59]:

$$\frac{\Delta\omega_z}{\omega_z} = -\frac{3B_1}{8B_0}\frac{C_3}{C_2}\frac{\omega_+}{\omega_-}\frac{r_+^2}{d_{\text{char}}}. \tag{2.43}$$

Comparing it with Eq. (2.40), one obtains the limit that uncertainty of C_3 and B_1 coefficients poses on the magnetic field optimisation:

$$B_2 = -\frac{3}{2}\frac{B_1 C_3}{C_2 d_{\text{char}}}. \tag{2.50}$$

Further limits arise from the combination of frequency shifts due to B_2 and leading order electrostatic anharmonicity, C_4:

$$\frac{\Delta\omega_z}{\omega_z} = \left(\frac{B_2}{4B_0}\frac{\omega_+}{\omega_-} - \frac{3}{2}\frac{C_4}{C_2 d_{\text{char}}^2}\right) r_+^2. \tag{2.44}$$

From optimizing the trap by nulling axial frequency shifts $\Delta\omega_z$ for excited r_+ amplitudes, one attains:

$$B_2 = \frac{6C_4}{C_2 d_{\text{char}}^2}\frac{\omega_-}{\omega_+}. \tag{2.45}$$

Further discussions on trap optimisation process and disentangling of the effects are given in Ch. 4.

2.2.4 Misalignment and Ellipticity

In the ideal trap, the z-axis of the electrostatic quadrupole potential aligns perfectly with the z-axis of the magnetic field. However, a small tilt θ between these axes is unavoidable in a real setup. Geometric and mechanical imperfections distort the azimuthal symmetry of the quadrupole electric field, which can be modeled as an effective ellipticity ϵ. These first-order imperfections cause frequency shifts even for a cold particle, while higher-order imperfections, scaling with energy, vanish with better cooling or at zero energy [60].

In the invariance theorem (See Eq. (2.12)), the shifts due to misalignment and ellipticity are suppressed, and the free cyclotron frequency is extracted from all three eigenfrequencies. The information about the tilt can be extracted from comparison of

the free cyclotron frequency determined from the sum of radial frequencies (Eq. (2.10)) and the one determined using a measurement of all eigenfrequencies via the invariance theorem (Eq. (2.12)):

$$(\omega_+ + \omega_-) - \sqrt{\omega_+^2 + \omega_z^2 + \omega_-^2} \approx \omega_- \left(\frac{9}{4}\theta^2 - \frac{1}{2}\epsilon^2\right). \tag{2.46}$$

The tilting mechanism of the LIONTRAP setup allows the adjusment of the angle between the z-axis of the electrostatic quadrupole potential and the magnetic field [58]. Further details are given in Sec. 4.5.

2.3 Methods

In this section, I provide an overview of the main experimental techniques used in trapped ion studies. This includes a non-destructive detection method based on image currents induced by a charged particle on the trap electrodes, various excitation and coupling mechanisms of eigenmodes, and the definition of temperature for a single trapped ion.

2.3.1 Induced Image Current Detection

The motion of ions inside a trap induces tiny currents in the order of $\sim$ fA in the electrodes. The Shockley-Ramo theorem states that the electric current i_{ind} induced by an ion with charge q moving with velocity $\dot{z}(t) = -\hat{z}\omega_z \sin(\omega_z t)$ between the plates of an infinitely extended capacitor is given by [61]:

$$i_{ind} = -q\hat{z}\omega_z \sin(\omega_z t) \cdot \frac{E_0}{U} = -\frac{q\hat{z}\omega_z \sin(\omega_z t)}{D}. \tag{2.47}$$

Here, $\hat{z}$ and ω_z are the amplitude and frequency of the motion, E_0 is the electric field of the capacitor plates at the position of the ion, and U is the bias potential of the plates in the absence of ion. $D = \frac{E_0}{U}$ corresponds to the distance of the capacitor plates and can be interpreted as an effective electrode distance for real cylindrical traps.

For a $^3He^+$ ion, with the typical $D \approx 10$ mm of the measurement trap, the thermal axial amplitude $\hat{z} = 40$ μm and $\omega_z = 2\pi \cdot 5 \cdot 10^5$ rad/s, one gets $\langle i_{ind} \rangle = i_{ind}^{rms} = \frac{q\hat{z}\omega_z}{D\sqrt{2}} \approx 1.4$ fA (10^{-15} A). In order to convert such small currents into measurable voltage, according to Ohm's law, the impedance Z of the detector should be as large as possible. This detection impedance can be realised by a coil with inductance L which, together with the parallel capacitance C_{total}, consisting of the trap capacitance

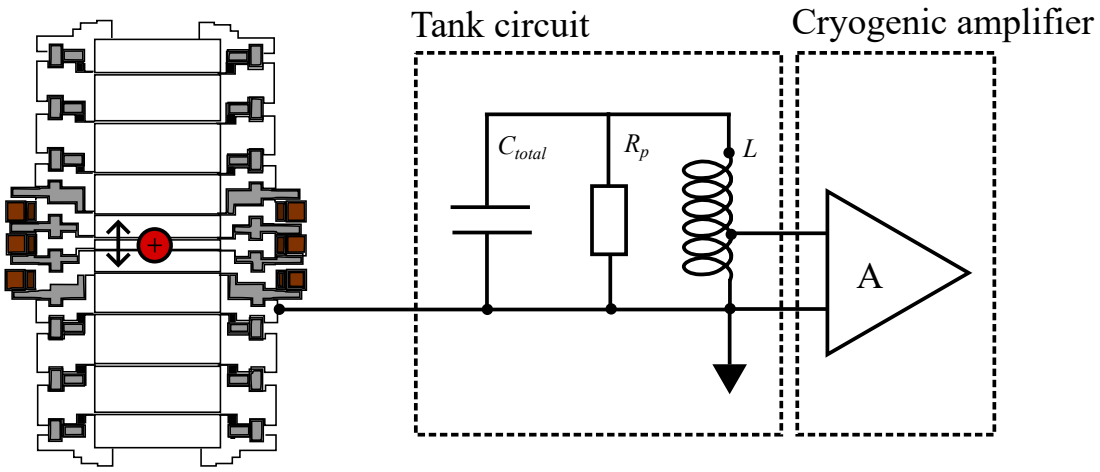

Figure 2.3. Schematic of the induced image current detection method. The current induced by ion oscillating in the trap is converted to a measurable voltage drop across the superconducting tank circuit, which is picked up by the low-noise cryogenic amplifier.

and parasitic self-capacitance of the coil and the wiring, forms a parallel resonance circuit, see Fig. 2.3. Such circuit exhibits resonance at a frequency:

$$\omega_{res} = \frac{1}{\sqrt{LC_{total}}}. \tag{2.48}$$

Resistive contributions in the resonator are expressed by an effective parallel resistance:

$$R_p = \omega_{LC} L Q. \tag{2.49}$$

Here, Q is a quality factor or $Q-$value, that quantifies the ratio of the stored electromagnetic energy to the energy loss per cycle. Experimentally, it is measured with a Vector Network Analyzer (VNA) as the ratio of the resonance frequency to the -3 dB width of the resonance line shape:

$$Q = \frac{\omega_{res}}{\Delta\omega_{-3dB}}. \tag{2.50}$$

The total impedance of such system is given by:

$$Z = \frac{1}{\frac{1}{i\omega L} + i\omega C_{total} + \frac{1}{R_p}} = \frac{R_p}{1 + iQ\left(\frac{\omega}{\omega_{res}} - \frac{\omega_{res}}{\omega}\right)}. \tag{2.51}$$

On resonance at ω_{res}, the imaginary part of the equation cancels out and the detection circuit acts as a real effective resistance R_p.

The resonance circuit will produce a thermal Johnson-Nyquist noise, given by the noise density at a frequency bandwidth $\Delta\nu$ (frequency resolution of the FFT) [62, 63]:

$$u_{th} = \sqrt{4k_B T \cdot \mathrm{Re}(Z)}. \tag{2.52}$$

Here, k_B is the Boltzmann constant and T is the temperature of the resonance circuit. Combining Eq. (2.52) and Eq. (2.51), we get the noise spectrum of the resonance circuit:

$$u_{res} = \sqrt{\frac{4k_B T R_p}{1 + Q^2 \left(\frac{\omega_{\mathrm{res}}}{\omega} - \frac{\omega}{\omega_{\mathrm{res}}}\right)^2}}. \tag{2.53}$$

The corresponding voltage signal is amplified by cryogenic amplifier, resulting in additional noise. This noise has several frequency components, which scale differently with the frequency (e.g. white noise or 1/f pink noise), however for small frequency range that we consider when detecting the resonator, it can be approximated as independent from frequency white noise u_{off} and linear frequency dependance given by the slope θ. After the cryogenic region, the signal is further amplified in the room temperature section, mixed down to the audio range (0-28 kHz) and Fourier transformed. The complete amplification factor of the system is given by a parameter A. The lineshape of the resonance is then given by:

$$u_{total} = A(1 + \theta(\omega - \omega_{res}))\sqrt{u_{res}^2 + u_{off}^2}. \tag{2.54}$$

In practice, the above expression is redefined and formulated in logarithmic units (dBVrms). The resulting lineshape is given in Eq. (6.8), and resonator fit plotted in Fig. 6.3b.

The lineshape above discussed describes the resonator spectrum in the absence of ion in the trap (or when ion's frequency is not in resonance with ω_{res}). The interaction of a single trapped ion with the resonator leads to a modified lineshape and allows for measurement of ion's motion frequency. When in resonance, the ion's motion is damped and thermalizes with the detection tank circuit. This effect is known as resistive cooling [64]. It is used to decrease the energy of trapped particles until they reach the thermal equilibrium with the tank circuit.

The small electric potential on the detection electrode u_{ind}, which is created by the induced image currents and the large resistance of the detection circuit, generates an additional damping force[1] acting on the ion, expressed as:

$$F_z = -m\gamma_z \dot{z} = -q\frac{u_{\mathrm{ind}}}{D} = -q\frac{Z i_{\mathrm{ind}}}{D} = -\frac{q^2 Z \dot{z}}{D^2}. \tag{2.55}$$

Now, using Eq. (2.47), the damping constant γ_z can be related to the particle and detector properties:

[1] The relations are derived for axial motion of an ion and can be applied to the other eigenmotions.

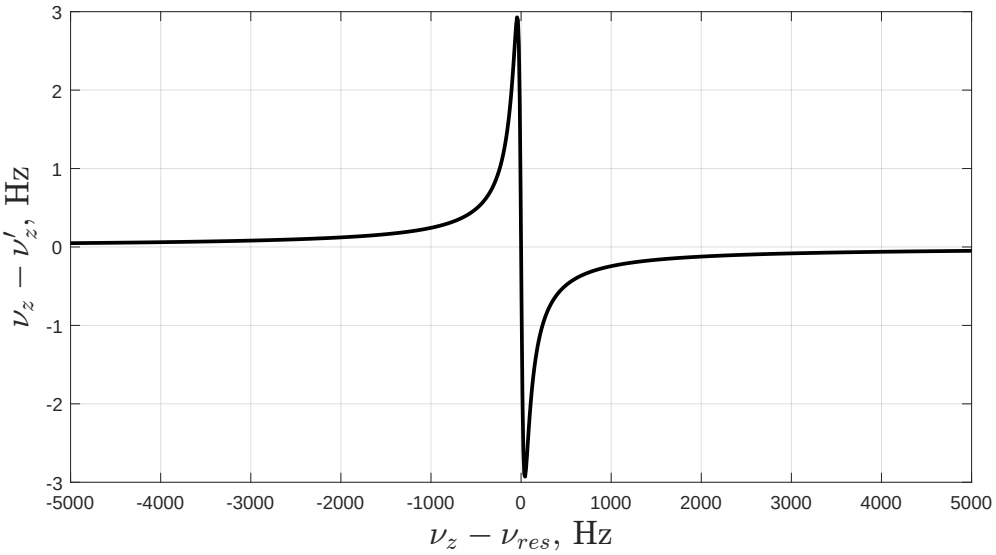

Figure 2.4. Shift in axial frequency, $\nu_z - \nu_z'$, caused by detuning from the resonance frequency, ν_{res}, due to the image current shift for a C^{4+} ion in the PT.

$$\gamma_z = \frac{Z}{m}\frac{q^2}{D^2}. \tag{2.56}$$

The equation of motion of the ion in the trap (see Eq. (2.6)) gets an additional damping term:

$$\ddot{z} + 2\gamma_z \dot{z} + \tilde{\omega_z}^2 z = 0. \tag{2.57}$$

Here, $\tilde{\omega_z}$ is the frequency of ion shifted due to complex nature of the impedance Z. The damping constant has both real and complex parts. The real part damps the axial motion of the ion. Through interaction with the resonator, the energy of the ion motion is dissipated in the latter and the ion loses its energy in an exponential decay on a time scale called the cooling time constant τ_z:

$$\tau_z = \frac{m\,D^2}{\mathrm{Re}(Z)q^2}. \tag{2.58}$$

The imaginary part of γ_z leads to an effective potential that results in shift in the eigenfrequency of the ion [65]:

$$\omega_z - \omega_z' = -\frac{q^2\,\mathrm{Im}(Z)}{2mD^2}. \tag{2.59}$$

This frequency shift, known as the *image current shift*, arises from the detuning of the ion's frequency relative to the resonator frequency, $\omega_z - \omega_{res}$. This detuning causes the ion's frequency to be either shifted further from the resonator's frequency, see Fig. 2.4. The magnitude of this shift can be minimized by either tuning the ion into exact resonance with the tank circuit or by ensuring that the resonator's frequency is sufficiently different from the ion's frequency [55].

2.3.2 Excitations and Couplings of the Eigenmotions

Several frequency detection and cooling techniques rely on modifying (exciting) and coupling the ion's eigenmotions by applying external oscillating electric fields. This section introduces the fundamental properties of dipole, quadrupole, and LC excitations.

Dipolar Excitation

Dipole excitation is used to directly and coherently excite an ion's motional mode. For the axial mode, the excitation exerts the following force on the ion:

$$\vec{F}_{\text{dipole}} = -q_{\text{ion}} \frac{U_{\text{exc}}}{D} \sin(\omega_{\text{rf}} t + \varphi_0)\vec{z}. \tag{2.60}$$

Here, q_{ion} is the ion's charge, U_{exc} is the voltage amplitude of the excitation signal, D is the effective electrode distance, ω_{rf} is the frequency of the excitation drive, and φ_0 is an arbitrary phase.

The corresponding oscillating potential is generated by applying an AC voltage to an off-center electrode, modifying the equation of motion (see Eq. (2.6)) and making it analogous to a forced harmonic oscillator.

Depending on the phase relation between the excitation drive and the ion's motion, the amplitude either increases immediately or initially decreases before growing in phase with the excitation. If the excitation amplitude is much larger than the ion's initial amplitude, the ion's motion amplitude or radius increases linearly. Thus, dipolar excitation of a cold ion can be used to imprint a specific amplitude and phase, which is extensively utilized in phase-sensitive measurements at LIONTRAP.

These results also apply to the radial modes. At LIONTRAP, such excitations are achieved by applying an oscillating voltage to one half of a split electrode of the trap.

Quadrupole Excitation

Quadrupole excitation in axial z and radial direction x acts on an ion with the force:

$$\vec{F}_{\text{quadrupole}} = -q_{\text{ion}} \frac{U_{\text{exc}}}{D} \sin(\omega_{\text{rf}} t + \varphi_0)(\vec{z} + \vec{x}). \tag{2.61}$$

Such a field configuration can be generated via a split off-centre electrode. Quadrupole excitation play crucial role in precision measurements in Penning traps in various ways:

- Excitation with frequency $\omega_{rf} = \omega_+ - \omega_z$ (the lower-sideband) couples axial and modified cyclotron motion of an ion, which leads to a coherent exchange of energy between the modes. This coupling is extensively used in phase sensitive

PnP measurement techniques and in the incoherent detection technique - double dip. Additionally, it is used to cool the modified cyclotron motion by coupling it to the axial mode, that is thermalised with the detector.

- Excitation with frequency $\omega_{rf} = \omega_+ + \omega_z$ (the upper-sideband) amplifies both modes and the amplitude in one mode determines the drive strength in the other mode. This excitation is used in the coherent measurement technique PnA, the main measurement method used at LIONTRAP.

- Coupling of axial and magnetron modes is performed with excitation on $\omega_{rf} = \omega_z + \omega_-$ frequency. The summation of frequency is the consequence of the fact that the energy associated with the magnetron motion is negative. This excitation is used to cool the magnetron motion by coupling it to the axial mode, which is in turn thermalised with the axial detection circuit. This method is called rf-sideband cooling.

LC Excitation - Electronic Feedback

Unlike dipole and quadrupole excitations, that act directly on an ion, LC excitation is applied on a resonator. The approach consists of creating a feedback loop, where the Johnson noise of the resonator is amplified, phase shifted and fed back capacitively to the resonator [66, 55]. Depending on the phase shift $\Delta\varphi$ between the feedback and the resonator signals, there are 3 important practical implementations of the technique:

- At $\Delta\varphi = 0°$, the so-called positive feedback occurs, It leads to an effective increase of Q-value and the temperature of the resonator.

- The feedback at $\Delta\varphi = 90°$ leads to shift in resonance frequency of the detection system.

- A phase shift of $\Delta\varphi = 180°$ results in the negative feedback. It leads to a decrease in the Q-value and the temperature of the resonator. This feedback is used the most at LIONTRAP in order to decrease the temperature of eigenmodes by coupling it to the axial mode that is thermalised to the axial resonator below the environment temperature of about 4.2 K. The resonator spectra with and without negative feedback are compared in Fig. 4.10.

At the start of the measurements, the feedback has to be *tuned*, meaning the suitable phase of the signal being fed back to the resonator line should be found. That is done by varying the phase and noting the resonance frequency ω_{res} and the its $Q-$ value. From comparing the characteristics of the resonator with and without negative

feedback applied, the achieved temperature of the resonator can be estimated, see Sec. 4.4 for details.

2.3.3 Temperatures of the Eigenmodes

In the studies of a single ion in a Penning trap, the term of ion's temperature is extensively used. In this section I define the term of ions eigenmode temperature and outline it's importance in regard to precision frequency measurements.

In atomic physics, temperature is typically defined through the energy distribution for a sample of particles. In case of a single trapped particle, the temperature can be statistically evaluated from the interaction of ion and the tank circuit. As described in Sec. 2.3.1, when oscillations of an ion in a trap resonate with the connected tank circuit, after a few cooling time constants τ, the ions motion gets in thermal equilibrium with the resonator. Then, by repeating the measurement of ions energy several times, an energy distribution is acquired, that corresponds to the expected temperature of the tank circuit. This is the result of the ergodic hypothesis, that states that the temperature can be evaluated not as an average over an ensemble, but rather as a time average over a single particle in thermal equilibrium with that ensemble [67]. In the case of a single ion in thermal equilibrium with a tank circuit, the ensemble is represented by the electron gas in the tank circuit.

At Liontrap, typically the axial motion is in thermal equilibrium with an axial tank circuit. The temperature of the circuit is at the environmental temperature of T = 4.2 K, or slightly lower by means of electronic feedback. The average axial energy is then given by:

$$\langle E \rangle = k_B T_{res}, \tag{2.62}$$

where T_{res} is the temperature of the electron gas of the resonator circuit. In thermal equilibrium, the axial temperature $T_z = T_{res}$.

Combining Eq. (2.17) and Eg. (2.62), the mean quantum number n_z can be estimated. Considering axial energy and axial temperature T_z =4.2 K, one gets $n_z \approx 1.8 \cdot 10^5$, that justifies the classical treatment of the system of an ion in a trap.

While at LIONTAP axial mode is cooled by coupling it to the resonator, the readial modes are cooled by coupling them to the axial mode using the resonant exchange of energy, that results in equal quantum numbers for the modes [55]. The temperatures are then given by the axial temperature times the frequency ratio:

$$T_{\pm} = \frac{\omega_{\pm}}{\omega_z} T_z. \tag{2.63}$$

2.3.4 Detection Techniques

At last, I discuss various detection techniques that are possible at LIONTRAP. There, the axial motion functions as an observational window into all modes of the ion within the trap, as it can be directly detected by an axial LC-resonance circuit. One can distinguish between thermalised dip detection method non-thermalised peak detection. The radial modes are, in turn, are coupled to the axial mode in order to be detected.

Thermalized Eigenfrequency Detection

As discussed in Sec. 2.3.1, the equation of motion of an ion thermalised with the tank circuit is expressed as a motion of a damped harmonic oscillator (see Eq. (2.57)). In order to describe the signal one gets from an ion which is in thermal equilibrium with a tank circuit, it is useful to develop a circuit representation of the ion. The equation of motion can be rewritten in terms of the induced current and voltage as [55]:

$$u_{\text{ind}} = \underbrace{\frac{m_D^2}{q^2}}_{L_{\text{ion}}} \frac{\partial i_{\text{ind}}}{\partial t} + \underbrace{\frac{m\omega_z^2 D^2}{q^2}}_{C_{\text{ion}}^{-1}} \int i_{\text{ind}}\, dt = \tag{2.64}$$

$$= L_{\text{ion}} \frac{\partial i_{\text{ind}}}{\partial t} + \frac{1}{C_{\text{ion}}} \int i_{\text{ind}}\, dt. \tag{2.65}$$

Hence, ion's motion can be represented by a series LC tank circuit with, where the impedance is given by:

$$Z_{\text{ion}} = i\omega L_{\text{ion}} + \frac{1}{i\omega C_{\text{ion}}}. \tag{2.66}$$

The total impedance of combined system of the ion and detection tank circuit is:

$$Z_{\text{tot}} = \left(\frac{1}{Z} + \frac{1}{Z_{\text{ion}}}\right)^{-1} = \left(\frac{1}{R_p}\left(1 + iQ\left(\frac{\omega}{\omega_{\text{res}}} - \frac{\omega_{\text{res}}}{\omega}\right)\right) + \frac{i}{\omega R_p \tau}\left(\frac{\omega_z^2}{\omega^2} - 1\right)^{-1}\right)^{-1}. \tag{2.67}$$

Taking into account, that only the real part of the total impedance influences the thermal noise spectrum, and considering Eq. (2.52), the lineshape resulting from interaction of an ion with the resonance tank circuit can be derived:

$$20 \log_{10} u_{\text{dip}}^n(\omega) = 10 \log_{10}\left[\tilde{A}\frac{\text{Re}(Z_{\text{tot}})}{R_p} + (\tilde{u}_{\text{ampl}}^n)^2\right] + \tilde{\kappa}_{\text{det}}(\omega - \omega_{\text{res}}) \quad (\text{dBV}_{\text{rms}}). \tag{2.68}$$

As the minimum impedance is achieved at resonance, the ion in thermal equilibrium with the resonator effectively shortens the detector impedance. This results in a sharp minimum in the thermal noise of the resonator and is called a *dip*, see Fig. 6.6. The frequency of the ion, therefore, can be measured in thermal equilibrium with the resonator by fitting the dip spectrum using the lineshape model (Eq. (2.68)).

The dip can be additionally characterized by its -3 dB width, $\Delta\nu_z$. It relates to the cooling time constant τ and the number of trapped ions N:

$$\Delta\nu_z = \frac{N}{2\pi\tau}. \tag{2.69}$$

This relation allows the determination of the number of thermalized trapped ions with the same ν_z.

The signal-to-noise ratio (SNR) of the dip is limited by the amplifier's voltage noise and the frequency resolution. For an ideal amplifier with no noise and a perfectly stable ν_z, the dip-depth would be infinite. The SNR is expressed as [66]:

$$\mathrm{SNR}_{\mathrm{dip}} = \frac{\sqrt{4k_BTR_p\kappa^2 + \left(i_{\mathrm{amp}}R_p\kappa^2\right)^2}}{u_{\mathrm{amp}}}, \tag{2.70}$$

where i_{amp} represents the current noise density of the amplifier and κ - total coupling constant of an ion with the detection circuit. According to this equation, increasing the temperature or current noise density improves the SNR; however, it also raises the ion's temperature, leading to systematic shifts. To optimize the SNR, it is necessary to minimize u_{amp} and i_{amp}, and to use a resonator with a higher Q-value.

The amplifier can be modeled with an input resistance R_{in} and capacitance C_{in}. The ion signal from the tuned circuit is coupled to the amplifier via a capacitance C_c and a tap on the coil's wire, which splits the coil into two sections. This configuration effectively forms an autotransformer with $N_1 + N_2$ primary turns and N_2 secondary turns. Consequently, the total coupling constant κ is defined as:

$$\kappa = \frac{N_2}{N_1 + N_2}\frac{C_c}{C_c + C_{\mathrm{in}}}. \tag{2.71}$$

The described approach works well for measuring ν_z, as long as the axial tank circuit is used for detection. However, for radial modes, the motion is first coupled to the axial mode, resulting in a modified detected signal, known as the *double-dip* [55]. For the modified cyclotron motion, as discussed in Sec. 2.3.2, the coupling drive at the lower sideband, $\omega_{\mathrm{rf}} = \omega_+ - \omega_z$, leads to a coherent exchange of energy between the axial and modified cyclotron modes. This can be seen as analogous to a driven quantum mechanical two-level system. During the rf-sideband coupling, the energy of both modes is continuously transferred between the two levels and oscillates with the Rabi frequency Ω, which depends on the excitation amplitude. The initial axial state becomes a superposition of two dressed states due to the modulation of the axial amplitude. The dip splits into two dips with frequencies given by:

$$\omega_{r,l} = \omega_z - \frac{\delta}{2} \pm \frac{1}{2}\sqrt{\delta^2 + \Omega^2}, \tag{2.72}$$

often denoted with indices l and r for the left and right dips. Here, δ is the detuning of the radio-frequency drive, defined as:

$$\delta = \omega_{\mathrm{rf}} - (\omega_+ - \omega_z). \tag{2.73}$$

Knowing the axial frequency measured by the dip technique and the coupling frequency ω_{rf}, one can deduce the modified cyclotron frequency by measuring the frequencies $\omega_{r,l}$:

$$\omega_+ = \omega_{\mathrm{rf}} + \omega_l + \omega_r - \omega_z. \tag{2.74}$$

This same principle can be applied to measure another radial frequency, the magnetron frequency ω_-. In this case, the upper sideband $\omega_{\mathrm{rf}} = \omega_z + \omega_-$ must be used. The magnetron frequency is extracted using:

$$\omega_- = \omega_{\mathrm{rf}} - \omega_l - \omega_r + \omega_z. \tag{2.75}$$

In a Penning trap, the corresponding drive frequency is relatively close to the axial frequency, leading to several complications. The dipolar component of the driving field will directly excite the axial motion, effectively increasing the ion's temperature. Additionally, the excitation can saturate the amplifiers, and may introduce noise into the resonator. Therefore, it is typically necessary to perform several double-dip spectrum measurements with decreasing coupling strength and extrapolate the resulting magnetron frequency to zero coupling strength, as described in Sec. 4.5.

Non-Thermalized Eigenfrequency Detection

In contrast to the thermalised dip detection method, where the particle is in thermal equilibrium with the resonator circuit, the signal from the excited ion (specifically axial motion) can be detected as a peak appearing on top of the resonator spectrum. The amplitude of this peak depends on the axial energy of the ion relative to the resonator's thermal noise. The ion is then detected through this peak, and the axial frequency is extracted from the maximum of the peak signal. The signal readout must be completed within a time shorter than a few cooling time constants τ. Otherwise, the axial energy will be dissipated into the tank circuit, preventing the peak from being observed. However, as the peak thermalizes quickly, the achievable precision in the measured axial frequency becomes limited. Moreover, due to the significant axial energy, the frequency measurements are subject to energy-dependent shifts.

Phase-Sensitive Detection Methods

The peak detection method described above not only allows for the determination of the axial frequency by identifying the peak position in the Fourier spectrum but also

provides access to the instantaneous phase of the ion. This capability enables phase-sensitive measurements of the axial frequency and, when combined with frequency coupling methods, allows for phase-sensitive measurements of the radial frequencies. For precision mass measurements, the measurement of the modified cyclotron frequency, ν_+, is of utmost importance. Therefore, this section focuses on phase-sensitive measurement techniques for this mode. Details of the axial phase-sensitive method are provided in Ch. 5.

The basic principle of the technique is to imprint a specific phase onto the ion's motion using dipolar excitation, allow the phase to evolve over a well-defined evolution time, T_{evol}, and then detect the resulting phase. The corresponding frequency can be determined from the phase difference, $\Delta\varphi$:

$$\nu_+ = \frac{\Delta\varphi}{360° T_{\mathrm{evol}}}. \tag{2.76}$$

This phase-sensitive measurement technique offers two main advantages over dip measurements. First, the relative uncertainty of the frequency exhibits an optimal inverse scaling with the measurement time, T_{evol}, whereas dip measurements, being noise-based, scale with $\sqrt{T_{\mathrm{meas}}}$. Second, in the case of peak detection, the phase is determined from the FFT bin with the largest amplitude, so there is no need for a line-shape model, as required for a dip spectrum. This approach avoids model-dependent systematic shifts and uncertainties. The phase of the cyclotron mode can be transferred to the phase of the axial mode using a second quadrupole excitation pulse, after which it is detected via axial peak detection. Depending on the frequency of the coupling pulse, one distinguishes between the PnP (Pulse aNd Phase) [68] and PnA (Pulse aNd Amplify) [66] techniques.

In the PnP technique, the coupling pulse at $\omega_{\mathrm{rf}} = \omega_+ - \omega_-$ is used to transfer frequency information from the modified cyclotron mode to the axial mode. The axial energy of the ion after the coupling pulse depends on the initial energy of the cyclotron mode. Since the signal-to-noise ratio (SNR) of the signal after coupling must be sufficiently high to unambiguously detect and extract phase information, the modified cyclotron mode needs to be excited to a relatively large orbit. However, this can introduce systematic shifts.

In contrast, the PnA technique is performed at the frequency $\omega_{\mathrm{rf}} = \omega_+ + \omega_-$. As described in Sec. 2.3.2, this leads to parametric amplification of both modes, enabling frequency measurements even at relatively low modified cyclotron excitation energies. This also allows for a much greater variation in excitation amplitudes compared to the PnP method, extending the accessible parameter range and mitigating systematic shifts caused by excitation amplitudes. Further details can be found in [66, 55] and

in the measurement analysis chapter (Ch. 6).

2.4 Further Frequency Shifts and Systematic Effects

Apart from the systematic shifts related to trap and field imperfections discussed earlier, several additional effects must be considered in precision measurements in Penning traps. These include relativistic mass increase and the image charge shift.

2.4.1 Relativistic Shift

The relativistic shift is a fundamental consequence of the special relativity effect, presenting itself in relativistic mass increase. It is present even in ideal trap and can not be tuned. The detailed analysis of the relativistic shift is given in [54].

For an ion with a rest mass m and velocity v that is much smaller than the speed of light c, the relativistic mass is given by:

$$\gamma m = \frac{m}{\sqrt{1-\left(\frac{v}{c}\right)^2}} \approx m\left(1+\frac{v^2}{2c^2}\right). \tag{2.77}$$

The mass increase, therefore, can be characterised by a value $\Delta m = \frac{v^2}{2c^2 m}$. Considering corresponding frequency shifts, only the shift in the modified cyclotron motion plays a role. Considering Eq. (2.77) and Eq. (2.7b), and using energy- amplitude relation from Eq. (2.15), the shift can be expressed as:

$$\frac{\Delta\omega_+}{\omega_+} = -\frac{\omega_+}{\omega_+-\omega_-}\frac{\Delta m}{m} = -\frac{\omega_+}{\omega_+-\omega_-}\frac{v^2}{2c^2} \approx \frac{E_+}{mc^2} = -\frac{\omega_+^2 r_+^2}{2c^2}. \tag{2.78}$$

For $^3He^+$ ion at the excitation amplitude $r_+ = 80$ μm, the modified cyclotron energy is $E_+ \approx 1.4$ eV, and the rest mass $mc^2 \approx 2.7$ GeV. The relative shift then becomes $\Delta\omega_+/\omega_+ \approx 5\cdot 10^{-10}$ and has to be considered.

2.4.2 Image Charge Shift

As described in Sec. 2.3.1, the image charges induced on the electrodes by the ion's oscillation enable non-destructive ion detection. However, these image charges generate an additional outward electric force, resulting in a frequency shift known as the *image charge shift*. In cylindrical traps, this effect primarily influences the radial motion, lowering the modified cyclotron frequency while increasing the magnetron frequency by the same amount.

This effect can be quantified through numerical COMSOL simulations of the trap geometry using finite element methods. Such simulations have been performed for our setup and verified to a relative precision of 5% by measuring the magnetron frequency difference between a proton and a $^{12}C^{6+}$ ion [69]. The relative shift of the cyclotron motion is given by:

$$\frac{\Delta\omega_c}{\omega_c} \approx -1.95\frac{m}{8\pi\epsilon_0 r^3 B^2}, \tag{2.79}$$

where r is the trap radius and ϵ_0 is the vacuum permittivity. A larger trap reduces this shift but also weakens the signal for image current detection, making measurements more challenging. Therefore, while designing the LIONTRAP precision trap, an optimal trap size with r =5 mm was determined to balance these effects [55].

Chapter 3

The Liontrap Experiment

In this chapter, I present an overview of the LIONTRAP experimental apparatus and various hardware components. The details on the setup can be found in several PhD theses [70, 58, 59]. The setup is an upgraded version of the predecessor g-factor experiment in Mainz, which was in operation until 2016 [71, 72, 66, 55]. Since then, to enable precision mass measurements of light ions, the setup has undergone several upgrades, including the implementation of a new trap system, the addition of a compensation coil to minimize magnetic field inhomogeneities, and the development of new ion sources that enable the production of helium ions, including the glass sphere source installed in the course of this work (see Sec. 3.3). Additionally, as part of this work, the detection system, including superconducting resonator coil and cryogenic amplifier, was upgraded (see Sec. 3.4), showing improved characteristics and enabling phase-sensitive axial frequency measurements, as described in Ch. 4.

3.1 Experimental Apparatus

The sketch of the experimental setup is presented in Fig. 3.1. The complete setup is placed inside a thermally insulated box. There, the heaters stabilize the temperature to 30 °C, and a fan system creates a constant airflow, ensuring even temperature distribution monitored by several PT-100 temperature sensors placed at different spots of the experiment. The setup consists of the superconducting magnet, cryostats, and the experimental apparatus. The magnetic trapping field of 3.76 T is generated by a superconducting NMR magnet from Oxford Instruments. The magnet was charged in 1995 and remained in continuous operation (persistent mode) until early 2024, when the measurements presented in this work were completed.

The experimental apparatus, placed inside the bore of the magnet, is cooled to cryogenic temperatures. The cooling system includes cryostats, namely an outer liquid

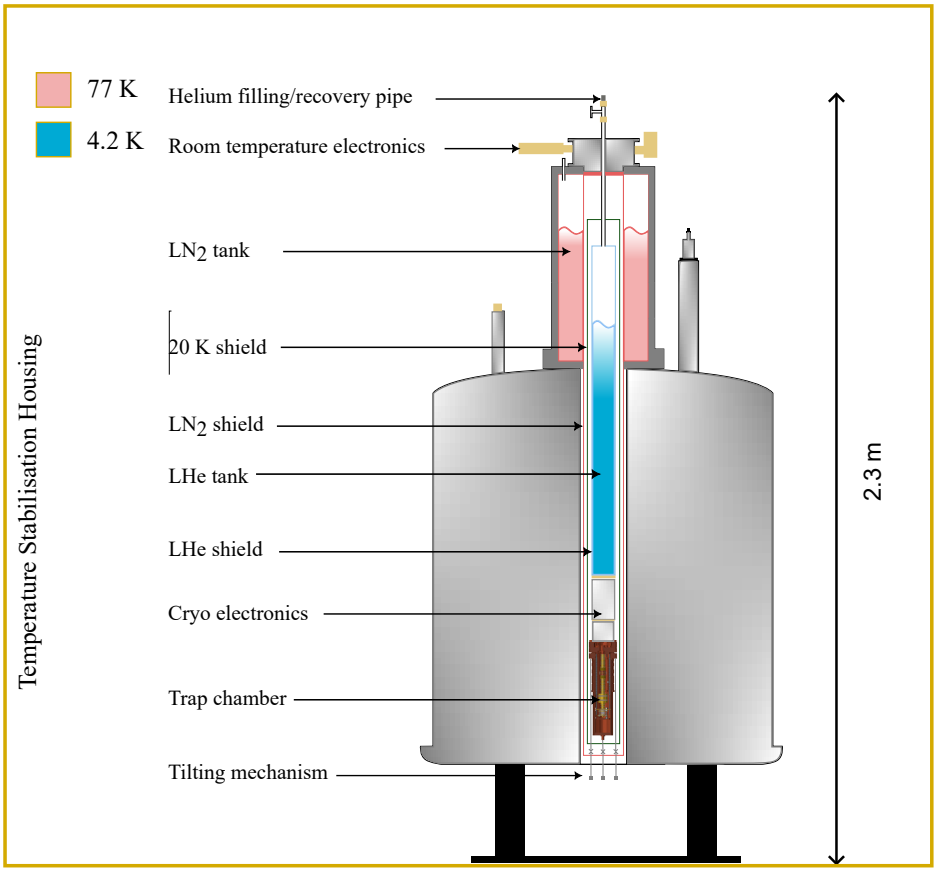

Figure 3.1. A sketch of the experimental setup. The apparatus includes cryostats filled with liquid nitrogen and helium, room-temperature and cryogenic electronics, and the trap tower that is placed in the sealed trap chamber. The apparatus is placed in the superconducting magnet. The complete experimental setup is placed in a temperature-stabilised environment.

nitrogen (LN_2) reservoir and an inner reservoir of liquid helium (LHe). The boil-off temperatures at normal pressure are 77 K for nitrogen and 4.2 K for helium. The thermal radiation and subsequently the evaporation rate of the helium are reduced by installation of a gas-cooled '20 K' shield in a 10^{-7} mbar vacuum between these reservoirs. This shield is fixed to the filling steel pipe of the helium reservoir of the apparatus.

On top of the apparatus, above the magnet, a so-called 'Hat flange' is located, where various boxes with room temperature electronics are connected. The voltage sources are also located in the temperature stabilized region, placed inside a copper isolation box. The precision DC trap voltages are supplied by two UM1-14 voltage sources by Stahl-Electronics. Other voltages, e.g. bias voltages of cryogenic amplifiers, are provided by self-built voltage sources [73].

3.2 Multi Penning-Trap System

The heart of the experiment is the trap tower, which consists of seven interconnected traps, totaling 38 electrodes. A schematic of the trap tower is shown in Fig. 3.2. Three traps are specifically dedicated to precision measurements: two storage traps (ST-I and ST-II) and the precision trap (PT). The rest of the tower comprises the Magnetometer Trap (MT) and a miniature electron beam ion source (mEBIS), which includes a Creation Trap (CT) and a field-emission point (FEP). Below is a detailed list of all the traps and their respective functions.

1. **Precision Trap** The Precision Trap (PT) is the main trap of the experiment, specifically designed for LIONTRAP [55, 6]. It has an increased trap radius of $r = 5$ mm to reduce the image charge shift. In the PT, high-precision measurements of the ions' eigenfrequencies are performed. It is a seven-electrode cylindrical trap with two pairs of correction electrodes, which allow achieving an orthogonal and compensated trap potential with minimized anharmonicity coefficients C_4 and C_6. The geometry, namely electrode lengths, are optimized such that the higher even-order coefficients, C_8 and C_{10}, are effectively null. The two end-cap electrodes are segmented, enabling reliable adiabatic transport of the ions. The inner upper correction electrode[1] and the ring electrode are azimuthally split for eigenmodes excitations. Three excitation lines were connected to the PT during the helium-3 measurement campaign:

[1]Normally, the lower inner correction electrode is split as well, but for helium-3 measurement campaign the two halves were shorted to connect the axial detector to the two lower correction electrodes.

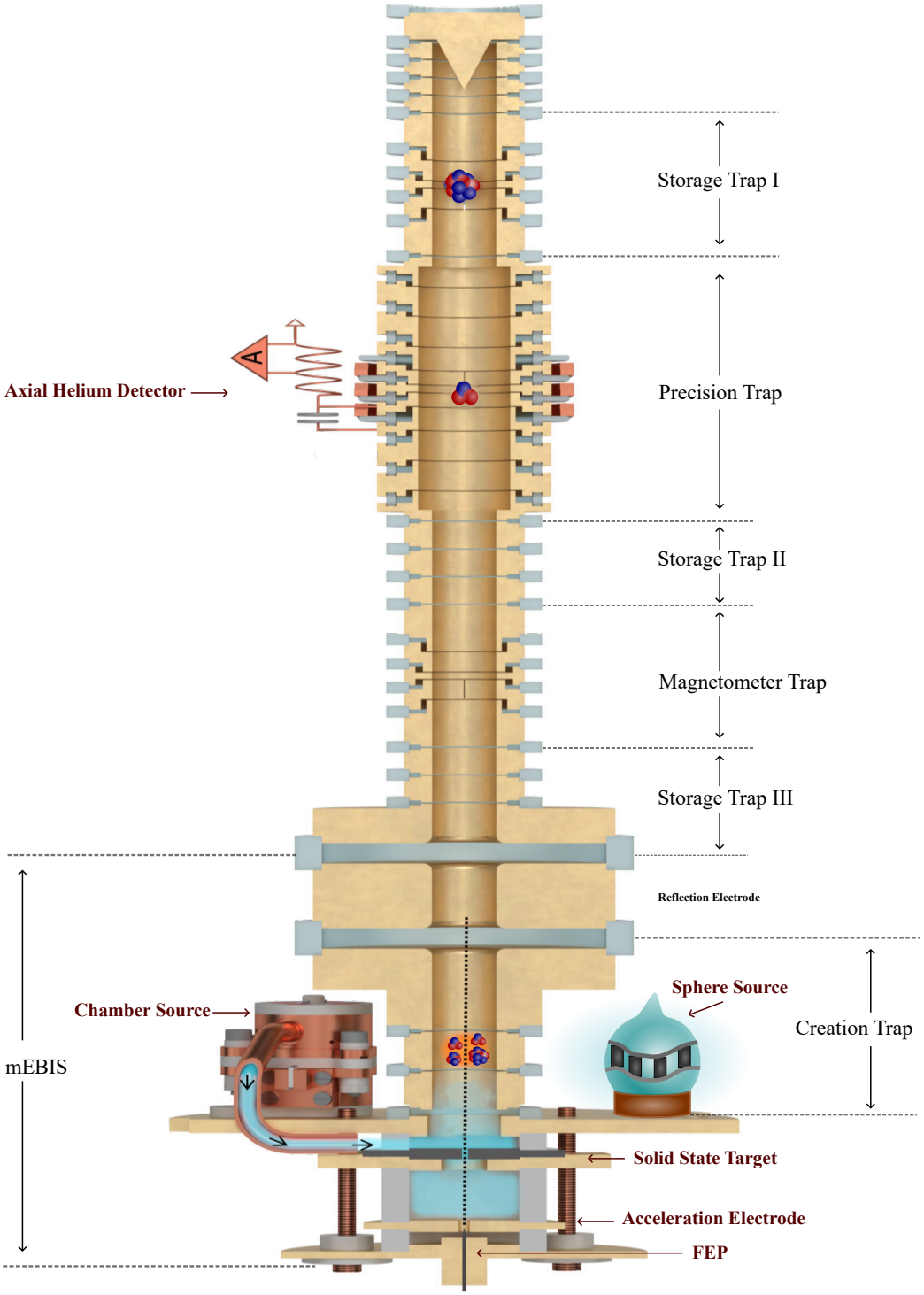

Figure 3.2. Sketch of the multi Penning-trap system of LIONTRAP. See text for details

- The **Dx** line is connected to one-half of the split ring electrode, and is intended for strong dipolar excitations in the radial direction with no nominal Qxz contribution. It is used, for example, during ion production process (see Sec. 4.1).
- The **Dz** excitation line is connected to the innermost upper endcap electrode and is intended for axial dipolar excitations. This line was used during ion production and axial phase sensitive measurement development, described in Ch. 4.
- The **Qxz** excitation line is connected to one half of the inner upper correction electrode. It is intended for quadrupolar excitations, which couple the axial and radial directions, however the excitations are not purely quadrupolar and exhibit additional dipolar components in both radial and axial directions (Dx and Dz) and can therefore be used universally. During the phase sensitive PnA measurements, the Qxz is used exclusively to provide the PnA ν_+ and $\nu_+ + \nu_z$ excitation pulses. Due to an additional dipolar component of this excitation line, during the second PnA pulse the resonant quadrupole excitation at the sideband frequency $\nu_+ + \nu_z$ competes with an off-resonant dipole excitation at ν_+ [55]. This effect can lead to a systematic shift in a read-out phase depending on the phase relation between the modified cyclotron phase of the ion and the starting phase of the second PnA pulse. To mitigate such effect, a randomised starting phase is implemented for the first PnA pulse, leading to an enhanced jitter of the measured phase, but not to any systematic phase shift.

The newly developed "helium" axial detector (see Sec. 3.4) was connected to both lower correction electrodes during the helium-3 campaign and used to measure the ions' frequencies in the mass measurement campaign. In contrast, apart from the new resonator, the second axial detector (labeled as the silicon detector) was connected to the outermost upper correction electrode but was not used during the campaign (see Fig. 3.6).

2. **Storage Traps**

Two storage traps (ST-I and ST-II) are located on both sides of the PT and serve as storage units for ions during the time that the frequency measurement is performed on one ion in the PT. The traps are essential for the shuttling measurement technique utilised at LIONTRAP, aimed at minimising the time between frequency measurements of two ions, which are performed in PT. The technique is detailed in Sec. 6.1. In the helium-3 measurement campaign, the

lower correction electrode of ST-I trap was grounded, so only the lower endcap of this trap was used for storage.

3. **Magnetometer Trap**

   The initial purpose of the Magnetometer Trap (MT) was to monitor magnetic field fluctuations concurrently with the main frequency measurements performed in the PT by conducting independent phase-sensitive measurements of the cyclotron frequency of a third ion. However, the magnetic field fluctuations in the PT and MT were found to be largely independent [70], and this technique did not yield the anticipated improvements in statistical precision. Therefore, this trap now serves as a storage trap during the ion production process.

4. **mEBIS: miniature Electron Beam Ion Source**

   LIONTRAP is an off-line experiment, which means that ions cannot be injected from an external source into the trap. Instead, the ions are produced *in situ*, within the cryopumped, hermetically sealed trap chamber. The production occurs in the mEBIS—miniature Electron Beam Ion Source [74, 75]. This part of the trap tower consists of the Field Emission Point (FEP), Creation Trap (CT), acceleration and reflection electrodes, and a solid-state target. Electrons are emitted from the FEP and accelerated by a high voltage difference applied between the FEP and the acceleration electrode. They are then reflected multiple times by the voltage on the reflection electrode, oscillating along the magnetic field lines as they pass through a $\sim 750\,\mu m$ hole in the target. Due to a space-charge build-up, the beam widens, and the electrons eventually strike the target surface, ablating atoms and molecules. These particles are subsequently ionized by the electron beam and captured in the CT, later being transported to the PT for further manipulation.

3.3 Ion Sources

The described above production method worked reliably for atoms that can be bond to a solid-state target at room temperature. This is, however, not the case for ^{4}He and ^{3}He. For these elements, gas has to be contained and stored inside a closed system and loaded into the trap chamber at room temperature. Additionally, the gas should not deteriorate the cryogenic vacuum quality and controlled release of gas in the production section of the trap tower should happen on demand. New ion sources, namely chamber and glass sphere sources, have been developed for respective ion

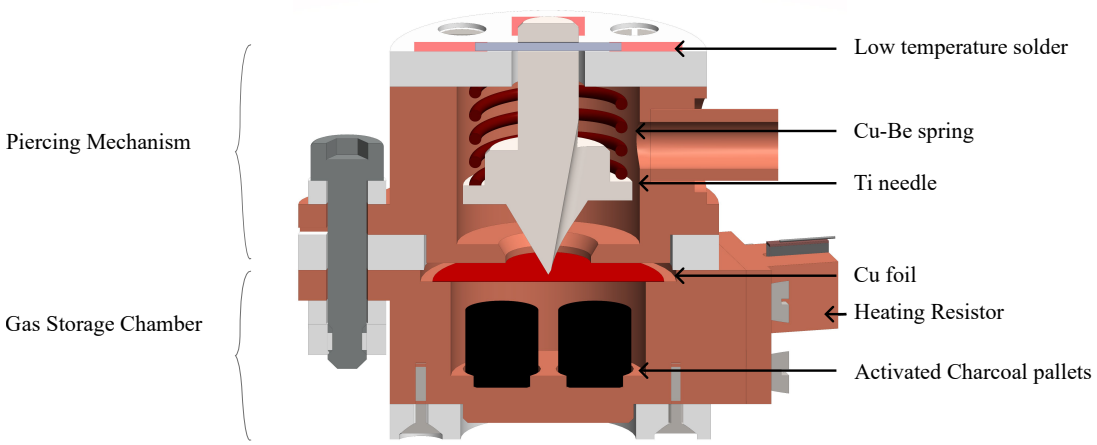

Figure 3.3. Cross-sectional view of the chamber source for gaseous species. The lower chamber that contains charcoal pellets is filled with gas at room temperature and sealed. The piercing mechanism is activated when the source is cooled down to cryogenic temperatures, piercing the foil sealing the lower chamber. The gas that is adsorbed by the pellets can be released by heating the chamber with the voltage applied across a heating resistor.

candidates, described in the next section. Additionally, within this work a new solid state deuterated target has been produced, enabling production of HD^+ ions.

3.3.1 Chamber Source

The chamber source, illustrated in Fig. 3.3, was developed by S. Sasidharan [59] for the ^{4}He mass measurement campaign. Initially, it was filled with ^{3}He gas; however, at that time, the triggering mechanism failed, preventing the production of ^{3}He. Instead, ^{4}He ions were generated by heating the chamber surface. For this campaign, the source has been modified to ensure proper functioning of the triggering mechanism.

The working principle of the source is based on the adsorption properties of gases on an adsorption agent, such as activated charcoal, at cryogenic temperatures. The highly porous structure of activated charcoal provides a large surface area for adsorption. In this source, the gas is initially contained within a small chamber filled with activated charcoal pellets. At room temperature, gas adsorption by the charcoal is negligible. However, when cooled to 4 K, the gas predominantly adsorbs onto the charcoal surface [76]. At this stage, the chamber can be pierced with minimal gas release into the trap chamber. By heating the chamber, the gas is desorbed and released into the trap, where it can be ionized by the electron beam.

The preparation of the source consists of two main stages. First, the chamber

containing the charcoal pellets must be prepared. After securing the pellets inside the chamber with heat-conductive glue, a copper foil is soft-soldered onto the top of the chamber to seal it. The gas storage chamber includes a tube for filling the gas, which is later pinched off to completely seal the chamber. To remove residual gases from the surfaces, the chamber and charcoal pellets are baked before filling with the gas of interest at approximately 100 mbar pressure.

Next, the piercing mechanism is prepared. In the initial source design, a wire was threaded through a titanium needle that was held in place by a copper-beryllium spring. The wire was then soldered on both sides of the source hat using low-temperature solder. One end of the wire was connected to a heating resistor, which was intended to melt the solder, releasing the needle to pierce the copper foil. However, this method failed during the previous helium-4 measurement campaign. The wire detached completely on only one side, while the other remained intact, preventing the piercing head from being released.

The likely cause of this failure was that only a single heating resistor was attached to one end of the wire, relying on heat conduction through the wire to melt the solder on the opposite side. In practice, however, as soon as the resistor-heated side detached, thermal contact was lost, and no further heat reached the opposite side, leaving the connection intact and preventing the piercing mechanism from activating.

To address this issue in the present campaign, the triggering mechanism was redesigned by removing the wire that held the piercing head. Instead, the titanium needle is now directly held in place by low-temperature solder on both sides of the source hat. To eliminate reliance on heat conduction for melting both solder joints, the heating resistors have been placed at both contact points of the piercing head, ensuring that both joints melt simultaneously and do not obstruct the triggering process.

To ensure the production of ^{3}He ions in this campaign, in addition to the chamber source we added a glass sphere source described in the next section. The chamber source, however, was later successfully tested (see Sec. 4.1) and allowed production of $^3He^+$ ions.

3.3.2 Glass Sphere Source

An alternative ion source consists of a fused silica glass sphere filled with ^{3}He gas. This type of source has been successfully developed and implemented in the µTEX experiment at MPIK [77]. The glass sphere exhibits permeability to helium, which strongly depends on temperature. At extremely low temperatures of around 4 K, the permeation rate is negligible. However, as the temperature increases, a significant

release of helium atoms from the sphere's walls into the trap region occurs [59]. These atoms can then be ionized and trapped using the mEBIS.

The glass sphere was fabricated and filled at the MPIK glassblowing workshop. The filling procedure is illustrated in Fig. 3.4. The process follows a similar scheme to that of the chamber source, but instead of a charcoal-filled copper chamber, a glass cell was integrated into the filling setup and filled with 150 mbar of ^{3}He gas. The glass was then melted using a heat torch to seal the gas inside.

After preparation, SMD thin-film heating resistors were attached to the glass sphere using ultrasonic soldering. The resistors, with a total resistance of approximately 100Ω, were selected to withstand power levels on the order of 1 W. Once assembled at room temperature, the glass sphere was carefully mounted outside the trap tower at a position providing a direct line of sight to the center of the electrodes in the production section, where the electron beam ionizes the helium atoms, see Fig. 3.2. At 4 K, the negligible gas permeation rate allows the sphere to be stored in the trap chamber for extended periods, requiring heating only when loading ^{3}He ions.

This source was extensively used during the helium-3 measurement campaign, see Sec. 4.1, enabling the reliable production of $^3He^+$ ions. Although the glass sphere technique is slightly less versatile than the adsorption chamber method, since not all gases permeate glass efficiently, it is particularly well-suited for helium gas.

3.3.3 Solid State Target

For the production of the reference ion, $^{12}C^{4+}$, the conventional solid-state target source is used. Prior to the helium-3 measurement campaign, the solid-state target located in the creation section of the trap tower was a polyetheretherketone (PEEK) target filled with carbon nanotubes to ensure electrical conductivity. A layer of deuterated molecules was printed on top of the target surface using a Drop-on-Demand inkjet printing system in cooperation with the Institute for Nuclear Chemistry in Mainz [58, 78].

In a previous helium-4 measurement campaign, we detected a decreased yield of deuteron and HD ions produced with this target. To ensure a sufficient deuteron content in the target for potential tests with HD molecular ions, we decided to produce a new solid-state target made from deuterated polyethylene. For target production, the steel press mould has been produced (see Fig. 3.5) and the Laboratory Hot Press from Specac was used to achieve the necessary pressure and temperature to melt the PE powders.

For the main target component, equal amounts of 0.2 g of high-density polyethylene (HDPE) and medium-density polyethylene (MDPE) were mixed, heated to 160°C,

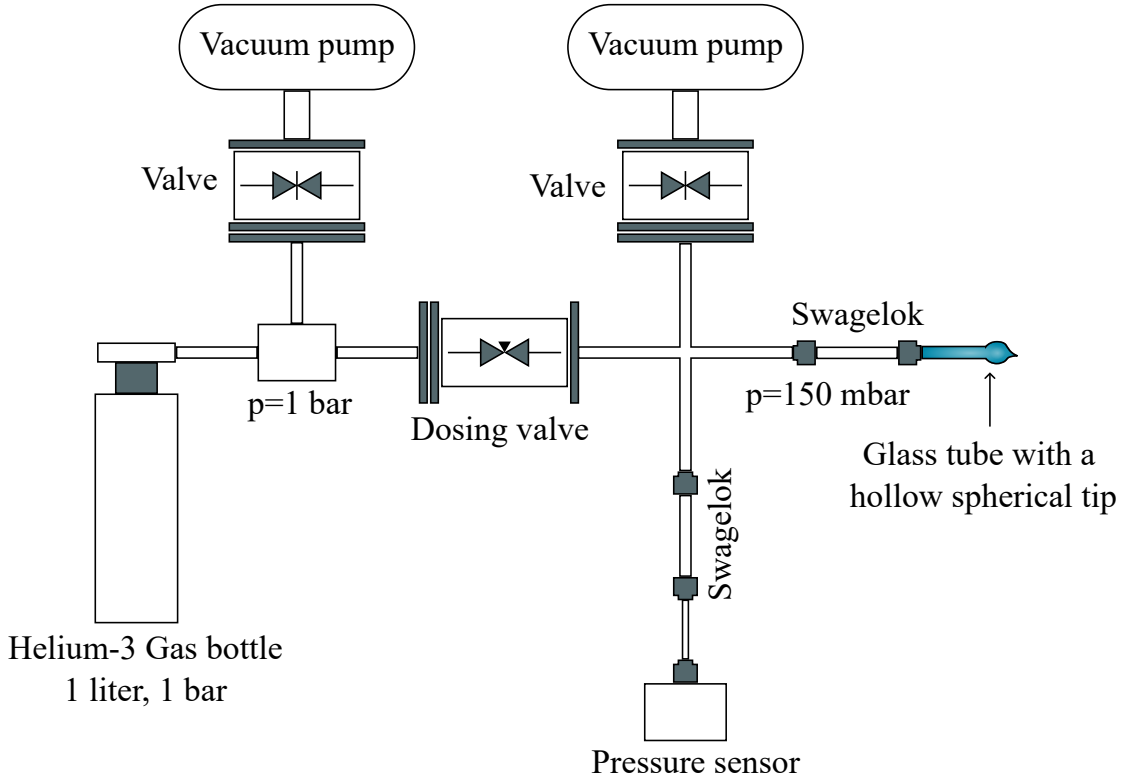

Figure 3.4. Schematics of the glass sphere source filling setup. A fused silica glass tube (radius $r = 5$ mm, wall thickness $d = 0.5$ mm) with a hollow spherical tip is connected to the filling system. The vacuum pumps are initially activated to evacuate all components. After that, both vacuum valves at the pumps are closed, and the gas bottle is opened to introduce gas into the small volume of the setup. The gas bottle is then closed again. Subsequently, the dosing valve is carefully adjusted to introduce approximately 150 mbar of gas into the source, with the pressure precisely monitored using a highly sensitive Paroscientific pressure sensor. Once the desired pressure is achieved, the tube is sealed by melting it with a heat torch, enclosing the gas within the sphere.

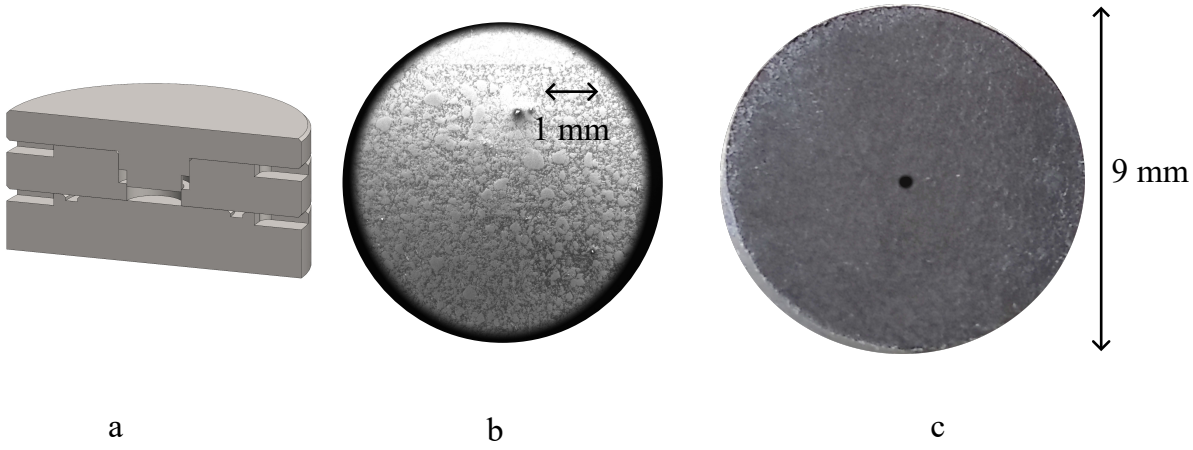

Figure 3.5. Production of the deuterated polyethylene target. Inset (a) shows a steel mould designed and manufactured for target pressing. Inset (b) presents an enlarged electron microscope image of the probe target surface at 20 kV electron energy, while inset (c) displays a photograph of the target with a 750 μm centre hole drilled to allow the electron beam to pass through during ion production.

and stirred until no clumps of HDPE remained. The mixture was then placed under vacuum while hot to allow air bubbles to escape. This procedure was repeated 3–4 times until no further air bubbles appeared. Subsequently, multi-walled carbon nanotubes (MWCNT) were added. Varying amounts of MWCNT were tested, and corresponding targets were examined using a scanning electron microscope (SEM), where charging effects appeared as bright spots. It was necessary to balance sufficient electrical conductivity with the reduction in proton and deuteron content caused by increasing the MWCNT concentration. For the final target 31% MWCNT was used. The mixture was heated and stirred again until a homogeneous mass was achieved. It was then placed into a preheated mould that had been treated with mould release spray. The mould was closed, and pressure was gradually applied, typically reaching an equivalent of 1 ton. The target was cooled while maintaining constant pressure. After removal and surface grinding, a hole of approximately ~ 0.7 mm was drilled at the center of the target. The produced target was successfully used during helium-3 measurement campaign to produce carbon, deutron and HD^+ ions, see Sec. 4.1.

3.4 Detection System

There are several axial detectors connected to the multi-trap system of LIONTRAP. An overview is presented in Fig. 3.6. The main detector used for all frequency measurements in the mass measurement campaign is located in the PT, connected to

lower correction electrodes. The detector utilised in previous measurement campaigns showed a gradual decrease in its Q-value (from 4400 [6] to 2300 [59]), despite the electrical connection remaining essentially unchanged in between. This is a often observed effect of Q-value degradation over time after multiple cooldowns, that likely stems from the differing thermal expansion behaviour of various materials used in resonators.

Moreover, the precision of the most recent measurement campaigns of the LIONTRAP experiment was limited by a systematic effect associated with the interaction of an ion's axial motion with the detector, referred to as the image current effect. To minimise the uncertainty associated with this effect, the resonance frequency must be precisely known at the time of the axial frequency measurements. A higher Q-value, combined with more frequent resonance frequency measurements, could be advantageous in this regard.

Additionally, for the development of the phase-sensitive axial frequency measurement technique detailed in Ch. 5, it was necessary to implement the ability to rapidly change the resonance frequency by approximately $\sim$ 1 kHz, that can be done by implementing a cryogenic switch mechanism that adds additional capacitance to the LC-detector, subsequently changing it's frequency. Consequently, we decided to replace the detector used in previous campaigns with an upgraded version, referred to as the Helium detector. The development process and the characteristics of the detector are detailed in the next section.

3.4.1 Helium Detector

The detection system consists of two main parts: the superconducting resonance coil and the low-noise high-input-impedance cryogenic amplifier (see Sec. 2.3.1 and Fig. 2.3). In the following sections, the experimental realization of the new axial detection system is discussed. The designs for both the coil and the amplifier are based on the old detection system designs, developed at previous g-factor Penning-trap experiments in Mainz [66, 79, 80].

Resonator

The design of the resonator coil sets the detector's and subsequently ions axial frequency, since the latter only depends on its charge-to-mass ratio and on the trapping voltages applied to the trap electrodes, see Eq. (2.7a). Several effects have to be taken into account to find the most suitable frequency [81]. Among them - the favourable suppression of axial frequency relative contribution in the invariance theorem with

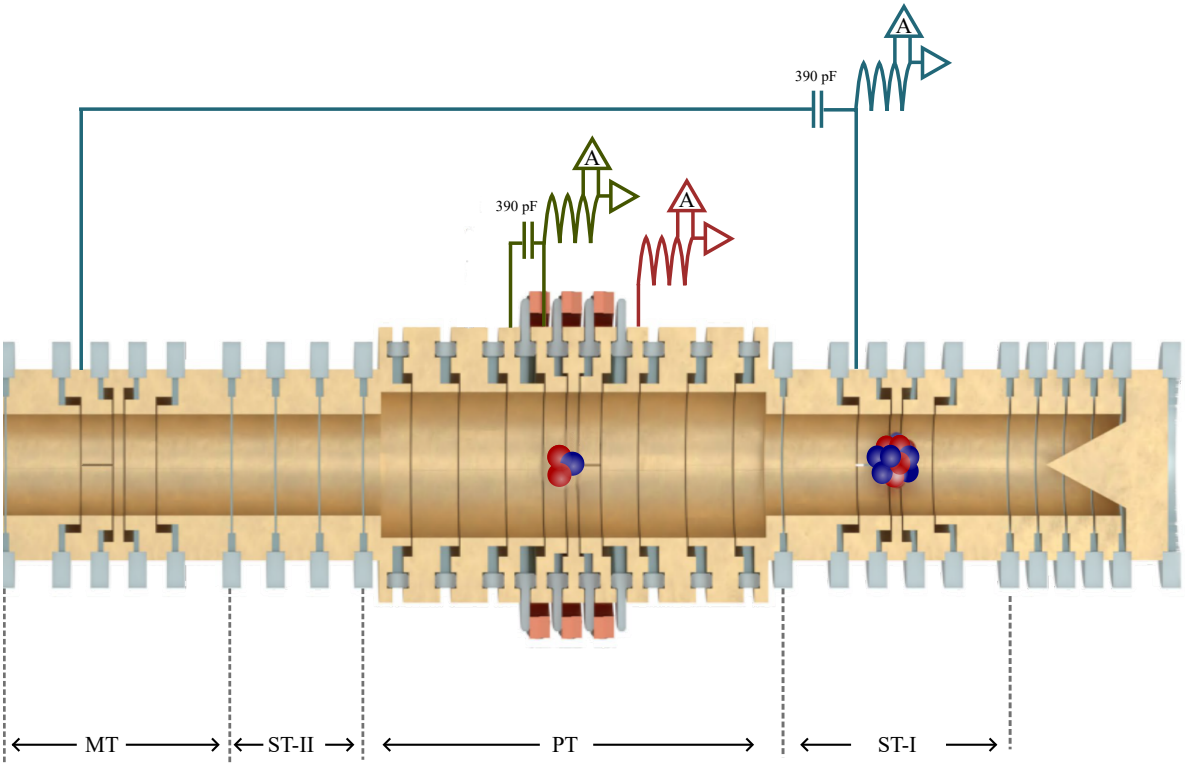

Figure 3.6. A sketch of the axial detectors connections to the traps. The newly developed Helium detector (depicted in green) and the Silicon detector (red) are connected to the PT. The Carbon detector (blue) is connected to the MT and ST-1.

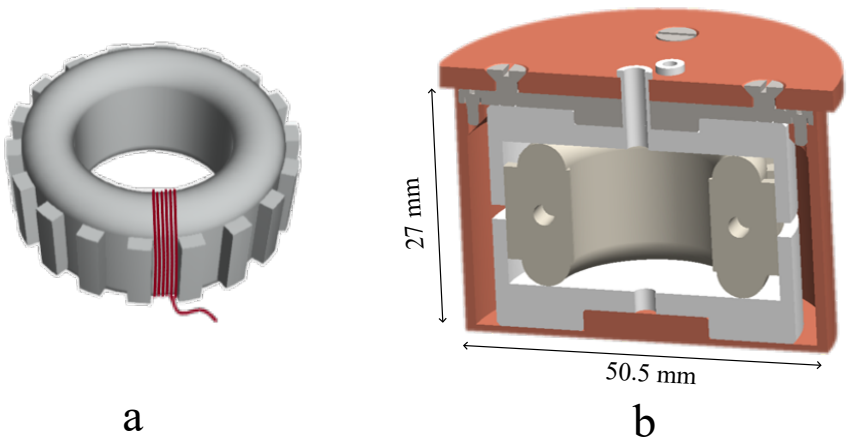

Figure 3.7. Sketch of the axial Helium resonator assembly. The toroidal coil body made of PTFE, on which the superconducting NbTi wire is wound (indicated with the red lines) is shown on the inset (a). The inset (b) shows the assembly of the coil body, supported by PTFE rings and placed inside a conducting OFHC housing.

lower ν_z, stable voltage range of a voltage source, the reduced relative influence of parasitic patch potentials on the trap electrodes and others. The voltage sources used at LIONTRAP operate in the range from 0 to -14 V and pose a limit on ν_z for particular $\frac{q}{m}$. With all of the above considered, the aimed frequency of the resonance coil is set to 500 kHz.

The schematic of the resonator design is presented in Fig. 3.7. The resonator consists of a toroidal coil body made of PTFE. The body is composed of two halves, each wound separately with superconducting 0.075 mm NbTi wire (PFA insulated, GVL Cryoengineering) in multiple layers, separated by PTFE tape. The halves are then connected, and a joint connection is made by twisting two uninsulated wire ends around each other. A small spring, made from copper wire, serves as a sleeve into which the twisted NbTi wires are inserted, and the sleeve is then filled with solder. In total, the coil has four layers of wire. The ratio of wire windings separated by tap wire is $R_{\text{coil}} = 1104/112 = 9.86$.

The toroidal design ensures that the magnetic flux is confined within the coil, which results in a low coupling to the resonator shield. Compared to the frequently used helical design, it offers higher performance at a lower form factor. After winding of the coil is complete, it is placed inside supporting PTFE rings and positioned within a conductive OFHC housing. Holes are made in the top of the housing to accommodate copper rods, allowing the housing to be fixed below the trap tower inside the trap chamber.

To determine the coil inductance L and self-capacitance C, the resonance frequency

$\omega_{\text{res}}^{\text{free}}$ of a free coil is first measured in the coldhead. Then, an external capacitance C_e is connected to the coil, and the resulting resonance frequency ω_{res}^{c} is measured. The inductance is then derived from[1]:

$$L = \frac{1}{C_e}\left(\left(\frac{1}{\omega_{\text{res}}^{c}}\right)^2 - \left(\frac{1}{\omega_{\text{res}}^{\text{free}}}\right)^2\right), \tag{3.1}$$

and the self-capacitance C (the parasitic capacitance of the coil and the housing) is given by:

$$C = \frac{1}{\omega_{\text{res}}^2 L}. \tag{3.2}$$

The derived parameters of the helium resonator coil are $L = 3.09$ mH and $C = 6.84$ pF.

Amplifier

In addition to the coil, a new cryogenic amplifier has been designed and produced. As outlined in Ch. 2, the amplifier must feature low-noise characteristics and high-input impedance to achieve a high signal-to-noise ratio of the detected signal. Parasitic feedback must be avoided through careful amplifier design. Furthermore, the amplifier should be positioned near the resonator within the cryogenic region to minimize the total system capacitance, reduce dielectric losses, and mitigate interference from external noise sources. A low power consumption is also essential to prevent heating in the cryogenic area. The design of the helium amplifier is based on the amplifier board developed in [66].

The schematic of the amplifier is shown in Fig. 3.8, and a photograph of it is provided in Fig. 3.9. The amplifier design is divided into three stages: amplification, cascode, and source follower.

1. The input of the amplifier is formed by two parallel metal-semiconductor field-effect transistors (MESFETs) of the model NE25129 from NEC. The common source topology provides high-input resistance and voltage amplification of the signals. The MESFETs are high-electron-mobility transistors (HEMT) based on Gallium Arsenide (GaAs), which continue to function under cryogenic conditions. The parallel configuration of dual-gate MESFETs suppresses incoherent

[1] A more careful approach involves multiple measurements with different external capacitors [82]. This helps to avoid problems arising from significantly different electrical lengths between a free coil and one with a capacitor connected in parallel. However, since we do not need to predict the resonance frequency exactly, a simplified measurement is performed.

noise sources by a factor of $1/\sqrt{2}$[1]. The used MESFET is a dual-gate transistor. By shortening the gates of both transistors, the total drain-to-source channel length extends from the source of the first transistor to the drain of the second and the flicker 1/f noise is decreased [83]. In addition, a varactor diod (a voltage controlled capacitor MA46H204-1056) and a cryogenic switch (SW-239) are connected, that allow to tune the frequency of the resonator. They form an additional tuning stage of the amplifier.

2. To suppress feedback at the amplifier's input caused by the parasitic gate-to-drain Miller capacitance of the input MESFETs with shorted gates, a *cascode* stage is formed using the transistor 3SK124 (NEC). In this configuration, the gate is held at a constant voltage (Voltage Gate2), and the transistor serves as a low impedance load to the first stage and a high parallel impedance to the resistive load R_{work}. This arrangement effectively reduces the voltage between the first stage and the cascode, while the amplified signal appears across R_{work}.

3. The third stage of this amplifier is formed by a source follower configuration (3SK124) to match the output impedance of the amplifier to the 50 Ω impedance of the transmission lines. This prevents reflections that could potentially cause amplifier oscillations.

The amplifier is DC-biased using external voltages, which are filtered on the amplifier's board. In the test designs, we attempted to separate gate biasing: instead of being shorted, the two gates (marked G1 and G2 in Fig. 3.8) of the amplification stage MESFET were supplied by two separate voltage lines, while G1 of the cascode MESFET was supplied by a third bias line, and G2 remained self-biased. With this configuration, we explored the possibility of fine-tuning the transistor biasing settings to reduce voltage noise at optimal amplification settings by increasing transconductance of the transistor. However, the described configuration did not significantly improve the amplifier's performance. To simplify the design and eliminate additional bias lines, we reverted to a connected-gate design, incorporating a combination of a cryogenic switch and a varactor to tune the resonance frequency.

In previous cryo-amplifiers of LIONTRAP, a single varactor was used to adjust the resonance frequency, as described in [84]. A varactor, along with tuning capacitors, forms an effective series resistance that acts as the primary loss contribution to the resonance circuit. To mitigate this effect, the new design combines the varactor with

[1]The choice of the number of transistors connected in parallel at the first amplification stage is part of the cryoamp noise matching procedure, connected to the tap ratio of the coil [66].

the cryogenic switch, so that the largest frequency difference between resonator settings needed for two ions with similar q/m is covered by a rapid change, on or off, in the switch state ($\sim$ 850 Hz at $\nu_{res} \approx$ 500 kHz), while only fine-tuning in the range of 300 Hz is performed with the varactor network. Despite the fact that the switch also poses limitations on the quality factor due to it's finate resistance in both *on* and *off* states, the tuning of the coupling of two frequency shifting methods allows for the loss minimization.

The board itself is made from Rogers RO4350B material. After milling the connections for the electronic components, the board is de-oxidized using H_2SO_4, then polished and placed in an ultrasonic bath with distilled water.

The amplifier's input-related voltage-noise density was measured at cryo-temperatures during cold head tests [85, 84]. The measurements were performed using a spectrum analyzer noise measurement function by detecting the base noise of the resonance spectrum and extracting the contribution of the cryo-amplifier noise with the known total amplification factor of the setup (an additional room temperature amplifier was connected in series). From this, the voltage noise density was found to be $u_{amp} \approx 1\ \mathrm{nV}/\sqrt{\mathrm{Hz}}$ around the expected frequency of 500 kHz.

The characteristics of the coupled tank circuit and amplifier system, connected to the trap, are presented in Tab. 3.1. With the new system, we improved the Q-value of the detection system by more than a factor of 2 compared to the detector used in the previous campaign [59]. However, the resulting Q-value remains significantly lower than the one measured in tests performed in the coldhead in the absence of a magnetic field and trap biasing (by approximately a factor of 4). This observation suggests that the response of the amplifier's electronic components to the magnetic field (such as the varactor diode) or the trap biasing might be the limiting factors for the achievable Q-value of the system.

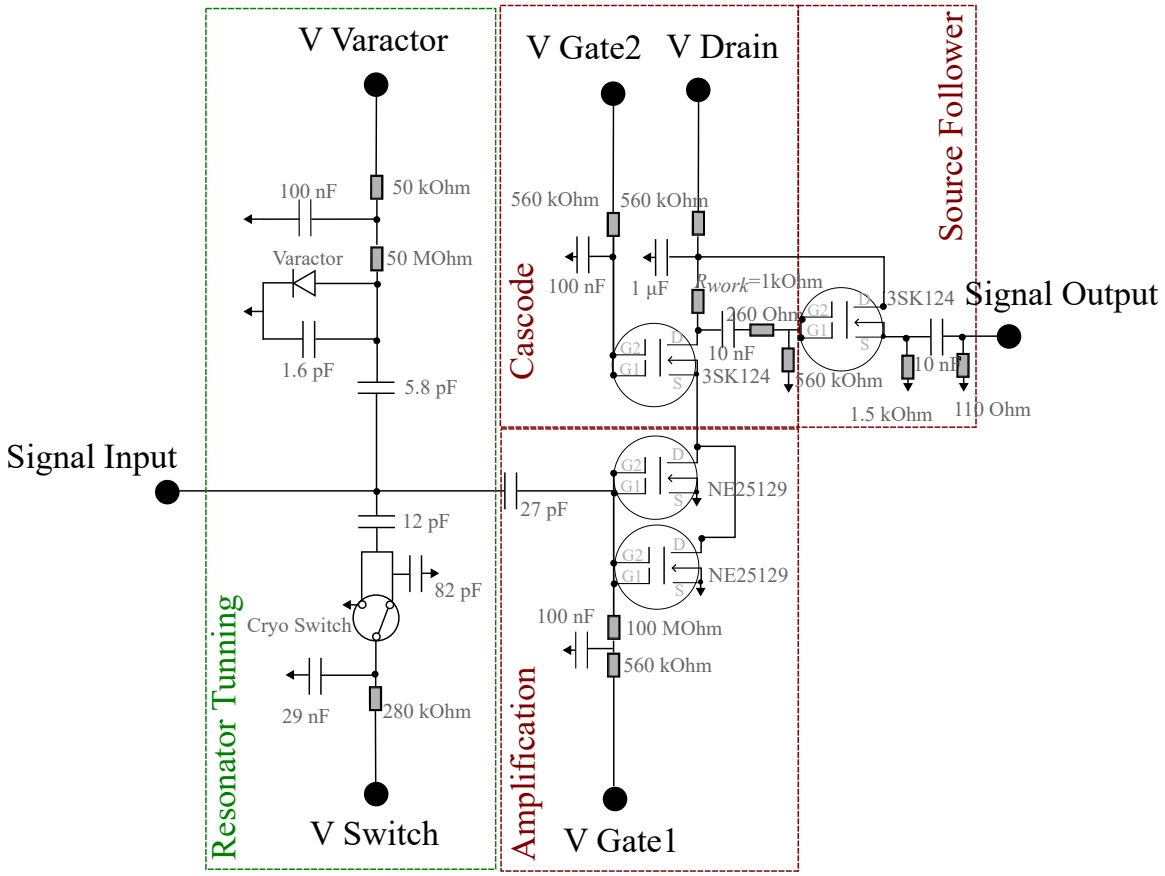

Figure 3.8. Schematic of the cryogenic axial amplifier. See text for details.

Table 3.1. The characteristics of the helium detection system connected to the PT at cryogenic temperatures. The characteristics include inductance L, capacitance C, signal-to-noise ratio SNR, resonance frequencyν_{res}, measured quality factor Q-value, and parallel resistance R_p. For ν_{res}, a range of frequencies is provided, which can be achieved through different varactor and cryo-switch settings.

Parameter	Value
L, mH	3.0891
C, pF	6.84
ν_{res}, Hz	507799 - 508871
Q-value	6000
R_p, MΩ	57

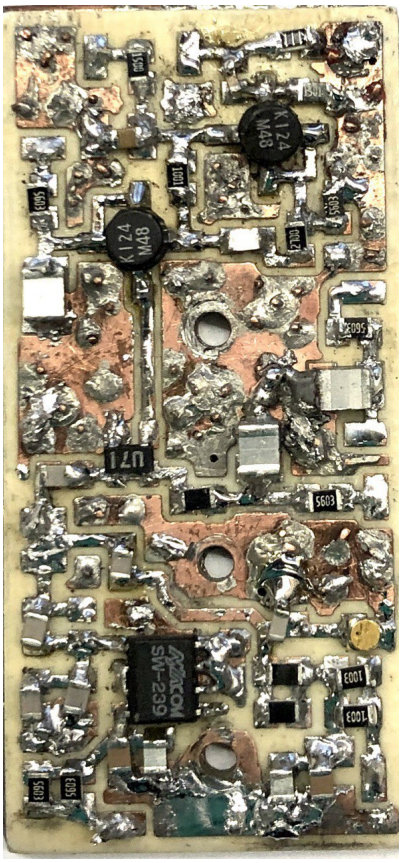

Figure 3.9. Photo of the cryogenic axial amplifier.

Chapter 4

Preparatory Measurements and Trap Optimisation

After making the necessary adjustments to the apparatus at room-temperature, the experiment was placed inside the magnet and cooled to 4 K. Once the system reached thermal equilibrium, typically after about a day, the resonator spectra were investigated. The resonance frequencies of all connected resonators were then identified based on their expected inductance and capacitance values. The parameters of the primary axial helium resonator developed during this campaign are detailed in Sec. 3.4.

After cooldown, the Carbon resonator, connected to the lower correction electrodes of the ST1 and MT traps, was not detected at the expected frequencies. By applying a white noise signal through the LC excitation line and scanning a broader frequency range, the resonator was located at a much lower frequency (120 ± 12 kHz), which corresponds to a 390 pF capacitor connected in parallel to the resonator. Indeed, such a capacitor exists between the two traps to decouple the DC lines with trap voltages (see Fig. 3.6).

This observation suggested that the lower correction electrode of the ST1 trap was grounded, which was confirmed by measuring a leakage resistance of approximately 1 GΩ to ground from one of the test pins of the UM voltage source. The ST1 trap is typically extensively used in the mass measurement campaign as a storage trap for the "upper" ion, while the cyclotron frequency of the second ion was measured in the Precision Trap (PT). However, even with the lower correction electrode grounded, the "upper" ion could still be stored in a potential well created by the lower endcap electrode of the ST1 trap.

Simulations of the trap voltages confirm that using the ST1 endcap electrode does not affect the harmonicity of the electrostatic potential beyond compensation capabilities in the PT. Therefore, no additional shifts in the measured ion frequencies

are introduced by this configuration.

4.1 Ion Loading

The next step involves the production of single trapped ions to fully test the setup's functionality, characterize the trap, and perform the mass measurement. As described in Ch. 3, for this campaign, the solid-state target and chamber source were replaced, and a fused silica sphere source was installed for the production of $^3He^+$ ions. The production process can generally be divided into two steps: the first involves trapping a cloud of ions produced by an electron beam in the CT, typically of different species and charge states, with the yield of the desired charge state optimized by adjusting the electron beam energy. Ideally, the production rate of ions of the desired type should be kept sufficiently low, as it is easier to clean the trap of contaminant ions when they differ in species and charge state from the desired ions. Additionally, producing large clouds of charged ions and performing the subsequent cleaning process, which involves ejecting ions out of the trap, might alter patch potentials of the trap walls, thereby affecting the trap's electrostatic potential profile. The second step consists of a cleaning process, resulting in a single isolated ion of the desired species and charge state being trapped.

4.1.1 Trapping Ions

The ions are produced in the miniature electron beam ion source (mEBIS) through charge breeding by consecutive electron-impact ionization [86]. The two outermost electrons of the ^{12}C electron shell are bound with energies of 11.26 eV and 24.38 eV, respectively [87]. To produce $^{12}C^{4+}$ ions, a potential difference of approximately 1.2 kV was applied between the field emission point (FEP) and the accelerator electrode for about 15 seconds, with the reflector voltage set to approximately 1.15 times the FEP voltage. The emitted electrons are reflected multiple times until they hit the solid-state target, where they are reabsorbed, consequently ablating atoms from the surface. These free atoms are then ionized by the electron beam and trapped in the creation trap (CT). The ion cloud is subsequently transported to the precision trap (PT), where a single ion is isolated through a cleaning process described in the following section.

For $^3He^+$, with the $1s^2$ electron bound at 24.58 eV, the atoms are first released from either the glass sphere or the chamber source by applying voltage across heating resistors attached to them. In the case of the sphere source, 0.5 W of heating power is

applied for approximately 8 seconds, with the FEP and reflector voltages already set. The accelerator voltage is then applied, creating a differential potential of about 1.2 kV between the FEP and the accelerator. The electron beam is turned on for about 15 seconds, after which it is switched off along with the heating, and a cloud of ions is trapped in the CT, followed by the adiabatic transport to the PT.

The heating process necessary for $^3He^+$ production caused quenching of the axial detector in the PT, indicating that parts of the superconducting resonator coil were heated beyond the critical temperature of NbTi (10 K). Initially, the quality factor (Q-value) of the resonator decreased significantly, followed by the complete disappearance of the resonator peak. Recovery of the system took approximately 15 minutes, and the entire process was monitored in real-time using the SR1 audio analyzer. Since the ion production procedure often needs to be repeated due to the high risk of losing the desired ion during the cleaning process, the delay caused by resonance quenching posed a significant inconvenience. Additionally, repeated heating of the resonator risks inducing irreversible changes to its characteristics, such as the parasitic capacitance of the trap, caused by slight movements of the electrodes. The production process was later optimized to avoid unnecessary heating and the generation of contaminant ions. Once the trap was characterized and the exact potentials required to bring $^3He^+$ into resonance with the axial detector were determined, it became possible to produce ions directly in the PT trap instead of the CT. In this case, the PT is set to the expected $^3He^+$ trapping voltage, while all other electrodes in the trap tower, including the reflector electrode, are kept at 0 V. Once heating of the sphere begins, the voltage difference between accelerator and FEP electrodes is set to 1.2 kV, and the resonator spectrum of the axial detector in the PT is monitored via the SR1. Often, the produced $^3He^+$ ion exhibits a high axial energy, resulting in a strong signal peak that appears on the resonator spectrum, "chirps" over it, and then disappears, as ion's kinetic energy is dumped onto the resonator. Afterward, the heating and accelerator voltage are switched off, and further cleaning is applied. This production procedure has the advantage of typically yielding a single ion of the desired species and charge state, significantly facilitating the trap cleaning process.

The procedure for creating He ions using the chamber source is similar to that of the glass sphere source, with the primary difference being that the chamber must be activated once per cooldown by piercing the copper foil sealing the chamber with charcoal, as described in Ch. 3. The source is then heated with 0.6 W of power for about a minute while the accelerator voltage is on, until the peak signal of the axially hot ion is detected on the resonator spectrum in the PT.

During the course of this work, we also successfully produced d^+ and HD^+ ions

using a new deuterated polyethylene target, following the same procedure as for $^{12}C^{4+}$ ions but with slightly lower electron beam energies. Notably, the time that the electron beam was applied for d^+ production appeared to be longer than for HD^+, likely reflecting the fact that a longer electron beam exposure time is required for the dissociation of the compound target molecule and the subsequent production of single-atom ions.

4.1.2 Trap Cleaning

Once the ion cloud is in the PT, the task is to isolate a single ion of the desired species and charge state while ejecting all other ions onto the trap walls. First, to ensure that the ion of interest is present in the ion cloud, the trap is set to the expected voltage for this ion type. A dipolar excitation at the expected modified cyclotron frequency, ν_+, is applied, followed by a quadrupolar pulse at the $\nu_+ - \nu_z$ frequency. Since ν_+ - unlike ν_- and ν_z - differs significantly between ion species with similar charge-to-mass ratios (by several kHz), exciting this mode and subsequently coupling it to the axial motion, produces a characteristic peak signal on the resonator, indicating the presence of the desired ion in the trap.

Several techniques can be employed to isolate the ion of interest [58]. In this campaign, we primarily used axial excitation sweeps, combined with lowering the trapping potential, to remove unwanted ions. Initially, the trapping potential is set to bring the ion of interest into resonance with the detector ($\nu_z \approx \nu_{res}$), thereby thermalizing its axial motion with the cryogenic LC circuit. Next, axial excitation sweeps are performed over the lower [30 kHz - (ν_z - 0.7 kHz)] and upper [(ν_z + 0.7 kHz) - 900 kHz] frequency ranges using the Dz excitation line. After these sweeps, the trap potential is lowered to approximately -1 V, allowing excited ions with different axial frequencies to escape. This procedure is repeated several times, leaving us with only ions of one particular type. However, this method does not allow for the isolation of a single ion from a cloud of ions with the same species and charge state.

To achieve single-ion isolation, axial excitation sweeps are conducted across the resonator in the $\nu_z \pm 1.5$ kHz range. Axially hot ions appear as peaks on the resonator, moving across it as their motion re-thermalizes with the detector. Before this re-thermalization occurs, the trap potential is lowered, enabling the hottest ions to escape. This method carries a high risk of losing all ions of interest, so it is crucial to maintain a low overall ion yield. The number of ions of the same species is controlled by measuring the width of the dip signal (see Ch. 2).

An additional method for determining the composition of the ion cloud is through the acquisition of a mass spectrum. This technique utilizes the axial peak detection

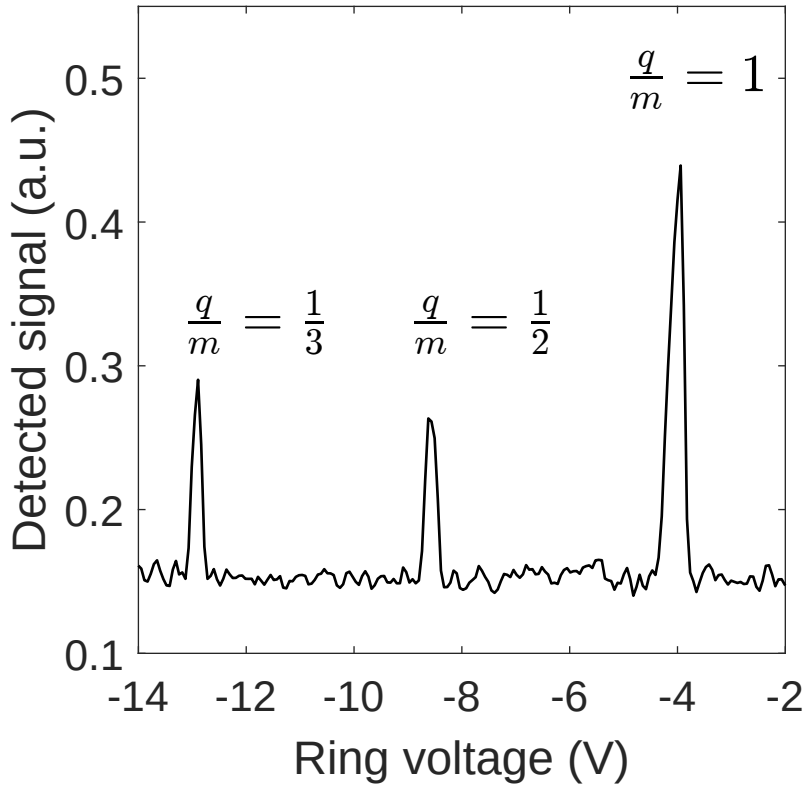

Figure 4.1. Exemplary mass spectrum, acquired after the $^3He^+$ ion production procedure described in Sec. 4.1.1, prior to cleaning of the trap. The peaks corresponding to $\frac{q}{m} = 1$ (protons), $\frac{q}{m} = \frac{1}{2}$ (possibly $^4He^{2+}$, d^+) and $\frac{q}{m} = \frac{1}{3}$ ($^3He^{1+}$, possibly HD^+ and $^{12}C^{4+}$) are visible.

method and the fact that the trap voltage at which the ion comes into resonance with the tank circuit is characteristic of the ion species, as the axial frequency depends on the charge-to-mass ratio. During acquisition, the resonance spectrum is continuously recorded as the trapping voltage is ramped down from the maximum voltage of the UM source to a minimum (typically [14 - 2] V), ensuring that the potential is not too shallow to avoid losing ions of interest. Simultaneously, a continuous axial dipolar drive at a frequency slightly above the tank circuit is applied, so that ions are first excited and then get into resonance with the tank circuit. The resolution of this method does not allow for distinguishing between ions with similar charge-to-mass ratios, but it helps to detect unwanted contaminant ions that differ significantly in their axial frequency.

Once the first ion, also referred to as the upper ion, is isolated in the PT, it is transported to the ST1 trap, while the second ion is produced and isolated in the PT. The upper ion is then regularly shuttled back to the PT to ensure that no contaminants have appeared and no heating has occurred during the cleaning process of the second

ion cloud in the neighbouring trap.

4.2 Electrostatic Field Optimisation

In a real Penning trap, the electrostatic potential deviates from the ideal quadrupole field due to machining tolerances of the electrodes and spacers, as well as contamination and patch potentials on the surface of the electrodes [66]. These field imperfections result in energy-dependent eigenfrequency shifts [54] (see Ch. 3).

4.2.1 Even-Order Anharmonicity: C_4, C_6

In the 7-electrode PT with two pairs of correction electrodes and grounded endcaps, the quadratic coefficient C_2 is given by the following equation:

$$C_2 = D_{21}\frac{U_{C1}}{U_r} + D_{22}\frac{U_{C2}}{U_r} + E_2, \tag{4.1}$$

where U_{C1} and U_{C2} are the voltages of the respective correction electrodes, U_r is the ring voltage, and D_{ik} are dimensionless coefficients of the electric potential. In our trap design, the so-called combined orthogonality criterion holds:

$$D_2^{\text{comb}} \equiv D_{21}\frac{U_{C1}}{U_r} + D_{22}\frac{U_{C2}}{U_r} = 0. \tag{4.2}$$

The ratios of the correction electrode voltages to that of the ring electrode are defined as the tuning ratios T_1 and T_2, and are expressed through a combined tuning ratio T_{comb} to facilitate the simultaneous adjustment of the correction electrode voltages, ensuring that the axial frequency, which is proportional to $\sqrt{C_2}$, remains unshifted:

$$T_1 = \frac{U_{C1}}{U_r} := T_{\text{comb}} \cdot T_1^{\text{start}}, \tag{4.3}$$

$$T_2 = \frac{U_{C2}}{U_r} := T_{\text{comb}} \cdot T_2^{\text{start}}. \tag{4.4}$$

The characterisation of the PT begins with the optimisation of the tuning ratio. To evaluate the harmonicity of the electrostatic potential, the dependence of the axial frequency shift $\Delta\nu_z$ on the magnetron excitation strength is studied, see Fig. 4.2. From Ch. 2, the shift in axial frequency due to an excited magnetron motion can be described by:

$$\Delta\nu_z \approx -\frac{3\nu_z}{2d_{\text{char}}^2}\frac{C_4}{C_2}r_-^2 + \frac{9\nu_z}{8d_{\text{char}}^2}\frac{C_3^2}{C_2^2}r_-^2 + \frac{45\nu_z}{16d_{\text{char}}^4}\frac{C_6}{C_2}r_-^4. \tag{4.5}$$

The shifts due to both C_4 and C_3^2 scale with r_-^2. Due to the inherent symmetry of the PT, in the initial optimisation procedure we assume $C_3 = 0$. A dedicated measurement is later performed to confirm the validity of this assumption (see Sec. 4.2.2). The optimisation procedure is described in detail in [6, 58, 59]. The steps of the optimisation process are as follows:

1. The values T_1^{start}, T_2^{start}, and T_{comb} are set to their expected optimal values. For our trap, $T_1^{\text{start}} \approx 0.963139$, $T_2^{\text{start}} \approx 0.818111$, and $T_{\text{comb}} \approx 0.999797$. The ring voltage U_r is adjusted so that $\nu_z \approx \nu_{res}$.

2. We select a range of T_{comb} around the expected optimal value. Typically, $C_4 \approx 10^{-4}$ in a not yet in situ optimised trap, so T_{comb} is varied accordingly. We then excite the magnetron motion by applying a dipolar pulse at the ν_- frequency, varying the excitation strength, and measure shifts in the axial frequency $\Delta\nu_z$ caused by the excitation. The shift is measured by taking dip spectra before and after the excitation pulse. The strength of the excitation is defined by the value $\#_{\text{cycl}} = \nu_- \cdot t_{exc}$, where t_{exc} is the duration of the dipolar excitation pulse at a fixed amplitude U_{exc} and frequency ν_-. It is preferable to vary the pulse length t_{exc}, rather than the amplitude U_{exc}, because of potential non-linearities in the calibration of the function generator used for excitation. The resulting two-parameter scan is depicted in Fig. 4.2 a. The shift in axial frequency for a fixed T_{comb} can be fitted with a low even-order polynomial:

$$\Delta\nu_z = \sum_{i=1}^{l} P_i \left(\#_{\text{cycl}}\right)^{2i}. \tag{4.6}$$

   Initially, the excitation is performed at a small amplitude, so that the effect of C_6 and higher-order anharmonicities is negligible, and $l = 1$ in Eq. (4.6). From Eq (4.6) and Eq. (4.5), an expression for the lowest-order anharmonicity coefficient can be derived:

$$C_4 = -\frac{2}{3}\frac{C_2 d_{\text{char}}^2}{\nu_z \kappa_-^2} P_1 = E_4 + D_4 T_{\text{comb}}. \tag{4.7}$$

   The slope coefficient D_4 is determined from solutions of the Laplace equation within the nominal electrode geometry: $D_4 = -0.79$ [59].

3. The magnetron radii after excitation and $\#_{\text{cycl}}$ are related by a calibration constant κ_-:

$$r_- = \kappa_- \cdot \#_{\text{cycl}}. \tag{4.8}$$

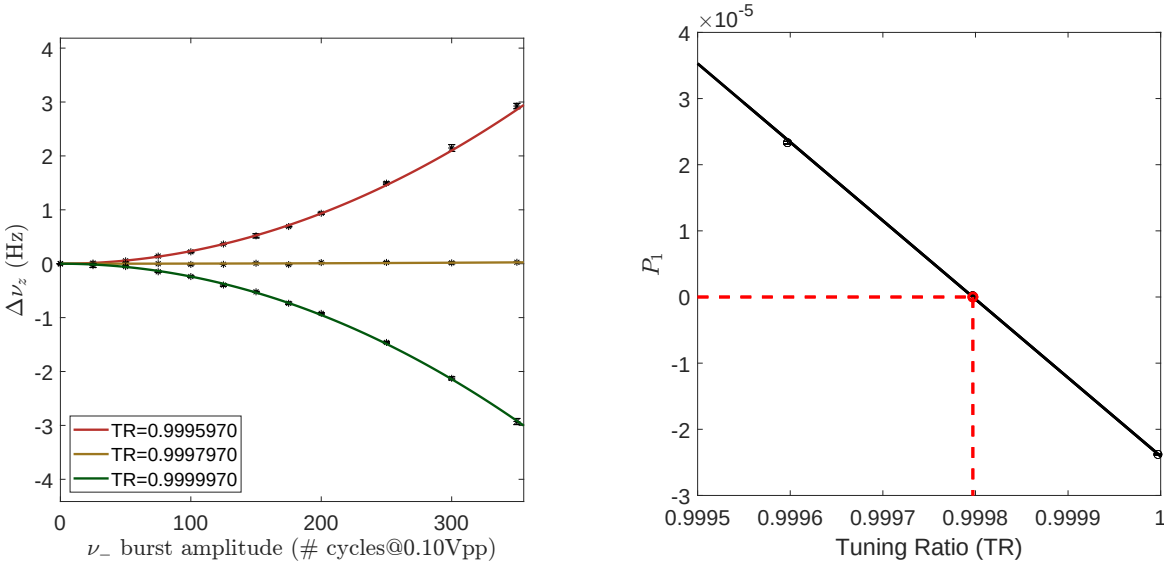

(a) (b)

Figure 4.2. An exemplary tuning ratio optimisation process. In (a), the axial frequency shift $\Delta\nu_z$ is taken as a function of the magnetron excitation strength and fitted with a function $f(x) = P_1 \cdot x^2$ for different tuning ratios. In (b), the coefficient P_1 is plotted versus the tuning ratio. The intersection of the resulting linear function with zero gives the tuning ratio where $C_4 = 0$, and the slope provides a calibration of the excitation strength κ_-.

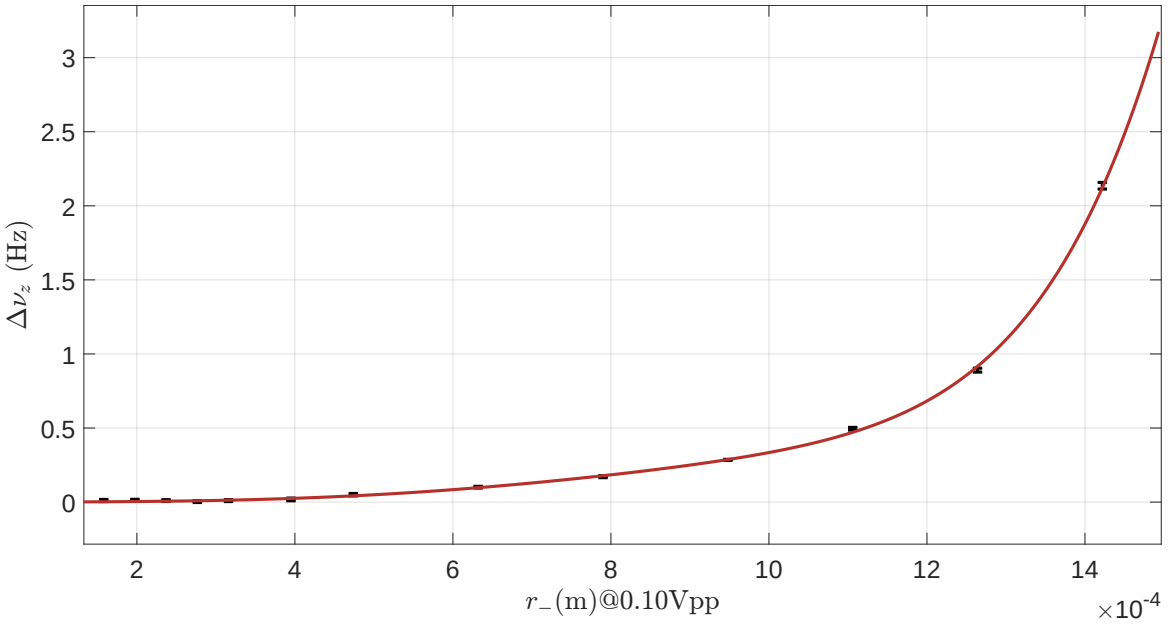

Figure 4.3. The axial frequency shift $\Delta\nu_z$ as a function of magnetron excitation for the optimal tuning ratio (TR). The data, plotted in black, is fitted with an even-order polynomial function (red line), up to the 8th order in this case.

For each value of T_{comb} used, the corresponding P_1 coefficient is extracted, and the dependency is fitted linearly, as shown in Fig. 4.2b. From Eq/ (4.7), the slope of the fit is given by:

$$n = \frac{\partial P_1}{\partial T_{\text{comb}}} = -\frac{3}{2}\frac{\nu_z \kappa_-^2}{d_{\text{char}}^2 C_2} D_4. \tag{4.9}$$

The fit point where $P_1 = 0$ determines the optimal T_{comb}, at which C_4 is nulled. Simultaneously, the slope coefficient enables the calculation of the calibration constant κ_-:

$$\kappa_- = \sqrt{\frac{-2nP_1 C_2 d_{\text{char}}^2}{3\nu_z D_4}} = 1.58 \cdot 10^{-6} \frac{m}{\#_{\text{cycl}}} \text{ @ } 0.1 V_{pp}. \tag{4.10}$$

The tuning of the electrostatic potential is repeated after each ion production cycle to account for the formation or modification of patch potentials on the electrode surfaces. If, after nulling C_4, the higher-order anharmonicity coefficient C_6 is large, the individual tuning ratios T_1 and T_2 can be varied, and the procedure can be repeated.

4. Afterwards, the measurement is repeated with this fixed tuning ratio but with an increased amplitude of the excitation. By fitting the dependence of $\Delta\nu_z$ on the calibrated excited radii of the magnetron motion (see Fig. 4.3), the coefficients C_4 and C_6 can be extracted using Eq. (4.5). Here, different ranges of magnetron radii are fitted with different polynomial order functions, and using the reduced χ^2 as a marker of the fit's goodness, we select a dedicated fit range for the extraction of C_4 and C_6 [58, 59].

Such measurements were repeated for all the ions used in the measurement campaign. For the final analysis, we give a combined conservative limit on C coefficients:

$$C_4 = 0(5) \cdot 10^{-6}, \tag{4.11}$$

$$C_6 = 0(3) \cdot 10^{-4}. \tag{4.12}$$

4.2.2 Odd-Order Anharmonicity: C_3

The described approach, however, assumes that odd C_i coefficients are 0. In practice, if there is a significant C_3 present, the optimisation process results in $C_4 = \frac{3C_3^2}{4C_2}$ when minimizing the axial shift after r_- excitation, as both C_4 and C_3^2 scale with r_-^2. Since the voltages of the trap are applied symmetrically, we usually assume $C_3 \leq 10^{-3}$,

given the manufacturing tolerances of the electrode lengths ($\pm 10\ \mu m$)[59]. To verify that this assumption is valid, we perform a dedicated measurement.

The expansion of the electrostatic potential in the axial direction with shifted equilibrium position with an offset Δz can be expressed in the following (see Eq. (2.19)):

$$\begin{aligned}\Phi(z) &= k_1(z+\Delta z) + k_2(z+\Delta z)^2 + k_3(z+\Delta z)^3 + ... \\ &\approx a + (k_2 + 3k_3\Delta z)z^2.\end{aligned} \tag{4.13}$$

Here, k_i are expansion coefficients that depend on trap voltage of a ring electrode U_r and the characteristic trap dimension d_{char}. In the second line of the equation, a includes terms that do not lead to shifts in ion's frequencies, and higher order terms are neglected.

If one artificially introduces an asymmetry of trapping potential by settings an offset of opposite signs on inner correction electrodes of the PT, ΔU_{cor1}, the potential from Eq. (4.13) is modified leading to linear change in first order expansion coefficients:

$$\tilde{\Phi}(z) = \Phi(z) + \Delta U_{cor1}\sum_i \Delta k_i z^i \approx \tilde{a} + (k_2 + \Delta U_{cor1}\Delta k_2 + 3\Delta z(k_3 + \Delta k_3 \Delta U_{cor1}))z^2. \tag{4.14}$$

Here, similarly to Eq. (4.13), the term $\tilde{a}$ includes terms that do not affect frequencies. Additionally, in a trap with $k_3 \approx 0$, the term Δk_2 should be 0. The axial frequency ν_z, which is proportional to the square root of the coefficient preceding z^2, is therefore modified. Analogous to Eq. (2.24), the $\tilde{\Phi}(z)$ has minimum at a following axial offset:

$$\Delta z = -\frac{\Delta U_{cor1}\Delta k_1}{2(k_2 + \underbrace{\Delta U_{cor1}\Delta k_2}_{\to 0})} \approx -\frac{\Delta U_{cor1}\Delta k_1}{2k_2}. \tag{4.15}$$

By altering the applied voltage asymmetry ΔU_{cor1} and finding the minimum of ν_z corresponding to an offset ΔU_{cor1}^{min}, one, therefore, attains the minimum of $\tilde{\Phi}(z)$, corresponding to a following equation:

$$\Delta U_{cor1}^{min}\Delta k_2 - \frac{3\Delta k_1}{2k_2}\left(k_3 + \Delta k_3 \Delta U_{cor1}^{min}\right) = 0. \tag{4.16}$$

From here, the residual k_3, or, alternatively, $C_3 = 2k_3 d_{\text{char}}^3/U_r$, can be obtained from:

$$k_3 = -\Delta k_3 \Delta U_{cor1}^{min} + \frac{2\Delta k_2 k_2}{3\Delta k_1}. \tag{4.17}$$

Although the second term in this equation is not known, the estimation from the trap geometry and natural size of Δk_2 suggests that it can be neglected for determination of an upper limit on k_3 (with the natural size of $\Delta k_3 \sim 1/d_{\text{char}}^3$).

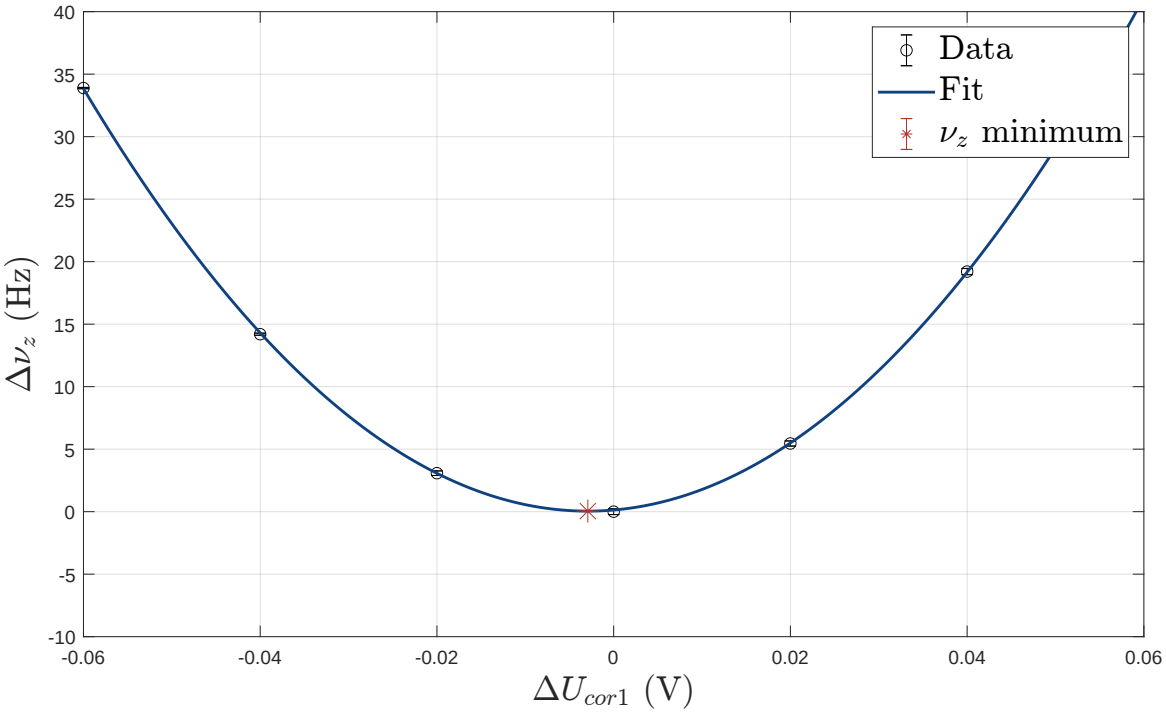

Figure 4.4. Measurement of the C_3 anharmonicity coefficient. In the trap, asymmetrical voltages are introduced by setting offsets on innermost correction electrodes ΔU_{cor1}. Consequently, the shift in axial frequency $\Delta\nu_z$ is measured. The minimum in axial frequency corresponds to an offset voltage $\delta U_{cor1} = 3$ mV and residual electrostatic anharmonicity $C_3 \approx 4 \cdot 10^{-4}$. See text for details.

In the measurement, the axial frequency shift $\Delta\nu_z$ for a cold ion is measured as a function of an offset ΔU_{cor1}, see Fig. 4.4. By extracting the offset in the trapping potential from the real value ($\Delta U_{cor1}^{min} = 3$ mV), we can give a limit on a C_3 present in the trap: $C_3 \approx 4 \cdot 10^{-4}$ - sufficiently low to neglect it in the consideration of electrostatic anharmonicities.

4.3 Magnetic Field Optimisation

The quadratic component of the magnetic field, B_2, causes leading-order frequency shifts. The compensation shim coil (referred to as the B_2 coil) allows for the suppression of B_2 down to a single mT/m^2. Typically, the coil remains discharged during the initial steps of trap optimization, specifically during tuning ratio optimization. As noted in (2.44), we nullify the combination of B_2 and C_4 in this optimization process. Therefore, after activating the coil, the optimization of the electrostatic field should be repeated.

The B_2 can be minimised even when its nominal value is unknown. By exciting modified cyclotron motion to an arbitrary, reasonably large radius with a dipolar excitation pulse, the axial frequency is shifted. In a trap with a small C_4, the shift is primarily caused by parasitic B_2, see Eq. (4.19). Therefore, a current is applied to the compensation coil to nullify the shift $\Delta\nu_z$. In this campaign, a coil current of 28.0(1) mA was applied. However, the connection of the current supply to the coil introduced significant noise on the resonator, where the axial frequency was monitored, thereby increasing the error in the minimisation of B_2.

After calibrating the cyclotron radius, as described in Sec. 4.3.1, the uncompensated B_2 was measured to be $B_2^{\text{uncomp.}} = -78(3)\cdot 10^{-3}$ T/m^2, see Sec. 4.3.2. From a series expansion of the simulated field of the coil around the minimum position of the PT, the quadratic field of the compensation coil per unit current is $B_{2,I} \approx 3.6\,\text{mT/mA/m}^2$ [58]. Therefore, to compensate for the measured B_2^{uncomp}, a coil current of $I \approx 21.7\,\text{mA}$ should, in principle, be applied to activate the coil, which significantly differs from the value used in this campaign. However, the simulation is based on measurements in the test set-up in the absence of the external magnetic field. The magnetic flux produced by the coil induces currents in the shim coils of the superconducting magnet, complicating the estimation of the exact field-current relation. Interestingly, the measured uncompensated value $B_2^{\text{uncomp.}}$ agrees well with the value observed in the previous mass measurement campaign [59], although the coil current required for compensation was lower then, namely 25.22 mA.

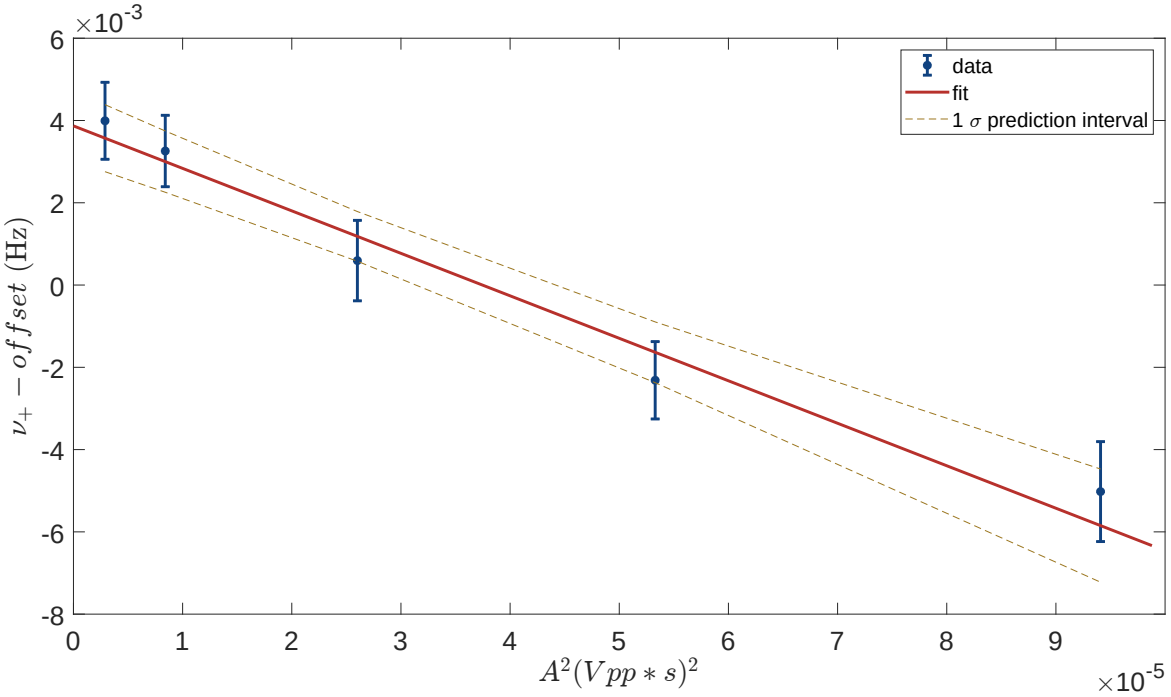

Figure 4.5. Exemplary calibration of the modified cyclotron radius performed with the $^3He^+$ ion. The calibration constant κ_+ is derived by measuring the shift in the modified cyclotron frequency as a function of excitation strength A.

4.3.1 Cyclotron Radius Calibration

To quantify the residual value of B_2, the modified cyclotron radius r_+ needs to be calibrated. In a trap with optimized C_4 and B_2, the shifts in modified cyclotron frequency as a function of modified cyclotron radius are primarily due to the relativistic shift, see Eq. (2.78). The calibration is performed by varying the strength of the dipolar excitation using the PnA method. The excitation strength $A = U \cdot t$, where U is the excitation amplitude and t is the excitation time, relates to the radius through the calibration constant: $r_+ = \kappa_+ A$. By fitting the cyclotron frequency shift linearly as a function of A^2, we extract the slope coefficient a and calculate the calibration constant:

$$\kappa_+ = \sqrt{-\frac{2ac^2}{\omega_+^2 \nu_+}}\,\mathrm{m\,Vpp^{-1}\,s^{-1}}. \tag{4.18}$$

Such data can also be extracted from the mass measurement, which is found to be reasonably consistent with preparatory measurements, see Tab. 6.4. The measured value is $\kappa_+ = 0.0086(2)\,\mathrm{m\,Vpp^{-1}\,s^{-1}}$. This value differs significantly (by more than a factor of 2) from the one obtained in a previous mass measurement campaign [59],

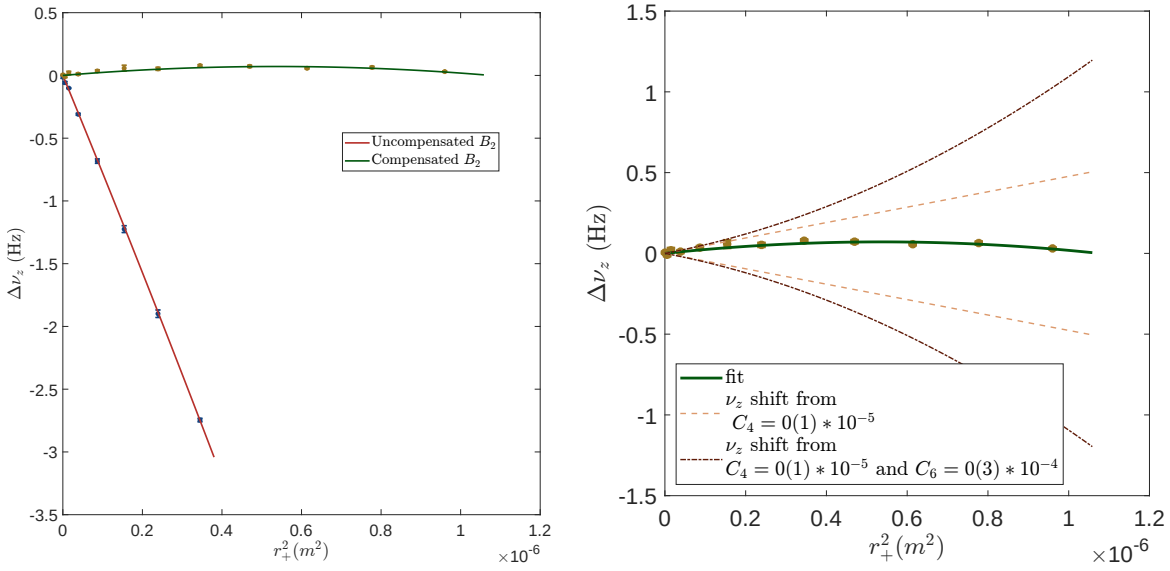

(a) (b)

Figure 4.6. Measurement of the quadratic magnetic field component B_2. The axial frequency shift $\Delta\nu_z$ is measured as a function of the modified cyclotron radius r_+. In (a), the shift is compared for cases with the B_2 shim coil discharged (red) and charged (green). In (b), a zoom-in on the compensated B_2 case is shown, illustrating the limitation due to residual electrostatic anharmonicity and the limit of further optimization of the magnetic field.

which likely relates to the exchange of the excitation filter board in the cryogenic region.

4.3.2 B_2 Compensation and Measurement

With the calibrated r_+, the residual magnetostatic inhomogeneity can be evaluated by measuring axial frequency shifts as a function of the modified cyclotron radius. The total shift can be expressed as follows:

$$\frac{\Delta\nu_z}{\nu_z} = \left(-\frac{C_4}{C_2}\frac{3}{2d_{\text{char}}^2} + \frac{B_2}{4B_0}\frac{\nu_+ + \nu_-}{\nu_-} - \frac{\omega_+^2}{4c^2} + \frac{9}{8}\frac{C_3^2}{C_2^2 d_{\text{char}}^2} \right) r_+^2. \tag{4.19}$$

Here, the relativistic mass increase term can be neglected, as the shift is ≤ 10 mHz for $r_+ \leq 500\ \mu m$. The contribution of the odd-order $C_3 \propto 10^{-4}$ is also negligible. With a large B_2, specifically when it is not yet compensated by the shim coil, the contribution of the electrostatic anharmonicity C_4 can be neglected. In this case, B_2 can be extracted from the linear term of a polynomial fit to $\Delta\nu_z(r_+^2)$, see Fig. 4.6a. When the B_2 coil is activated, the contribution from the C_4 term becomes significant and essentially limits the optimization of B_2, see Fig. 4.6b.

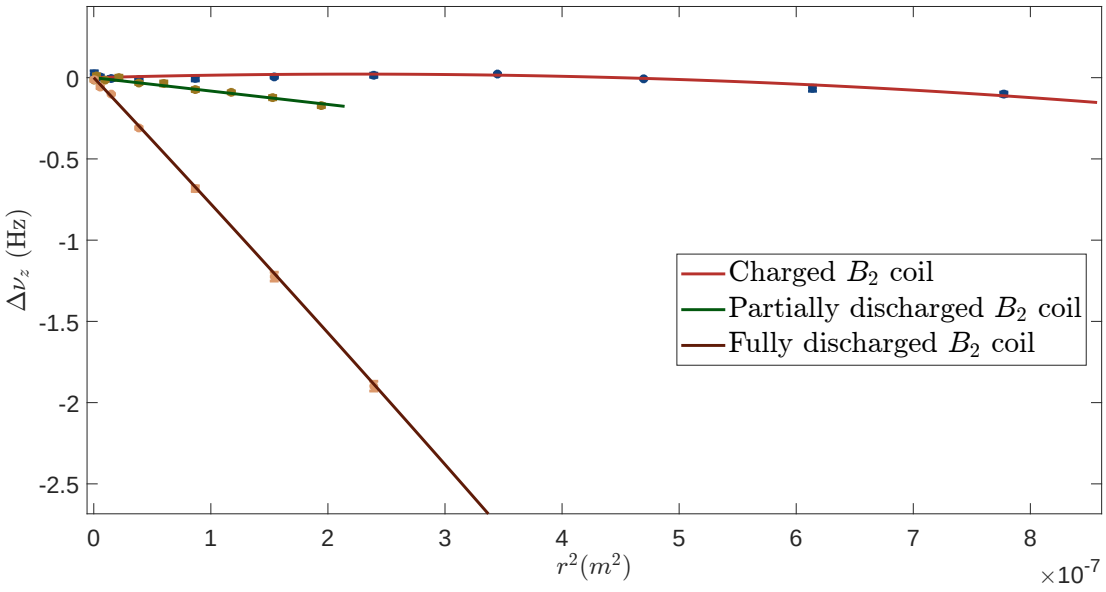

Figure 4.7. Partial discharge of the B_2 compensation coil. The axial frequency shift $\Delta\nu_z$ is measured as a function of the modified cyclotron radius r_+. The measurement taken right after charging the coil is shown in red, with the extracted residual $B_2 = 2.0(3) \cdot 10^{-3}$ T/m^2, assuming $C_4 = 0$. The measurement was repeated after about a month, shown in green, with the estimated $B_2^{\text{part. disch.}} = -8.0(4) \cdot 10^{-3}$ T/m^2. Finally, the shift with the fully quenched compensation coil is shown in brown, with the measured $B_2^{\text{uncomp.}} = -78(3) \cdot 10^{-3}$ T/m^2.

After the activation of the B_2 coil, the magnetic field inhomogeneity was monitored regularly by performing single excitations at $r_+ \approx 1$ mm and measuring the shift in the axial frequency. In this campaign, we detected a partial discharge of the coil about a month after charging it, see Fig. 4.7. The cause is unclear, and this effect was not observed in previous measurement campaigns [58, 59]. The observed change in the B_2 component is $8.0(4) \cdot 10^{-3}$ T/m^2 within a month. The existence of a small leakage resistance could cause a gradual decay of the coil current. Alternatively, changes in the external magnetic field, such as movements of the compensation coil in the high magnetic field of the superconducting magnet, could cause transient losses. It is also unclear whether the change occurred gradually over time or abruptly, e.g., after mechanical disturbances during the cryogenic liquid filling process. Based on several observations of such discharges during the measurement campaign, we conclude that the B_2 likely did not exceed the value measured right before recharging the coil, meaning the change was always towards a more negative "uncompensated" B_2. For the final analysis, we set a conservative estimate of the quadratic component of the magnetic field:

$$B_2 = 0(10) \cdot 10^{-3} \text{ T/m}^2. \tag{4.20}$$

The B_2 was continuously monitored and the compensation coil was recharged throughout the campaign using a constant coil current of $I = 28.0 \pm 0.1$ A.

4.3.3 Residual B_1

The linear magnetic field gradient B_1 is estimated by measuring the cyclotron frequency shifts of the ion at different positions along the z-axis in the trap. The position of the ion is shifted by applying asymmetric voltages to the correction electrodes. The offset z-positions of the ion in the trap are calculated by simulating the trap potential. The free cyclotron frequency of the ion at different positions is determined by measuring dip and double-dip spectra to extract ν_z and ν_+. The results of the measurement are plotted in Fig. 4.8. By fitting the slope through the frequency shifts at three different positions in the trap, B_1 can be extracted (if B_2 is sufficiently small):

$$\frac{\Delta B}{B} \approx \frac{B_1}{B_0} \Delta z \approx \frac{\Delta \omega_c}{\omega_c}. \tag{4.21}$$

The linear inhomogeneity is measured to be $B_1 = 0.0025(2)\,\text{T m}^{-1}$ when the B_2 shim coil is charged. The corresponding shift in the cyclotron frequency ratio is $\Delta R_{CF} < 10^{-14}$, which can be neglected.

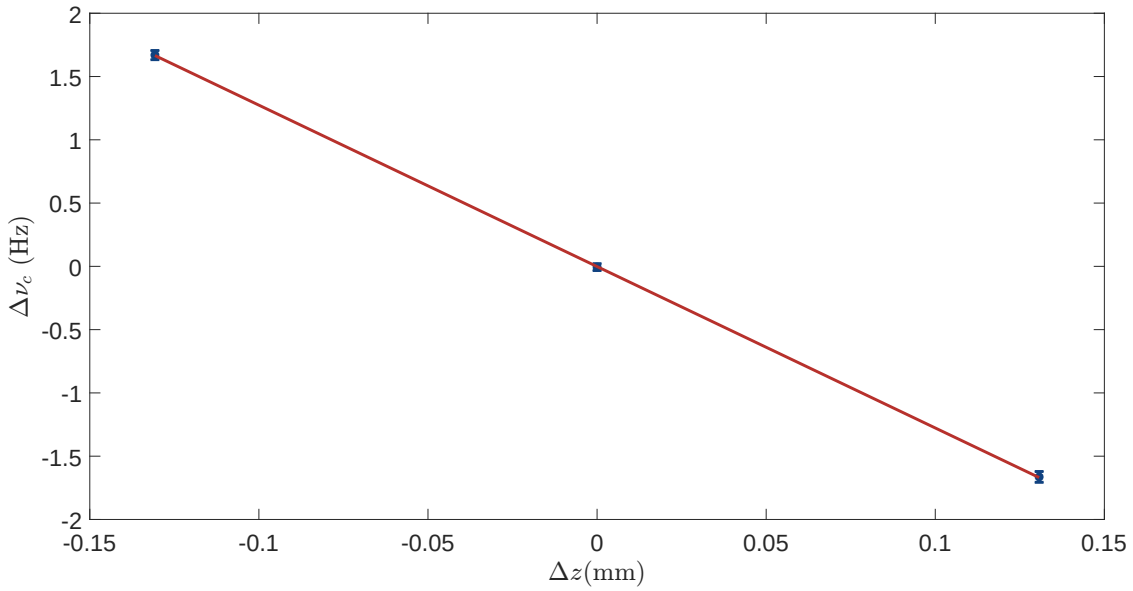

Figure 4.8. Linear magnetic field gradient B_1 measurement. The cyclotron frequency ν_c is measured at shifted ion positions along the axial direction z, resulting from different offset voltages on the correction electrodes. In this measurement, the voltages of the correction-1 electrodes of the PT are shifted by ± 0.4 V, from which the shift Δz is derived using a simulation of the trap potentials.

4.4 Temperature Measurement

According to the ergodic hypothesis, the energy distribution of a single ion in the trap follows the thermal energy distribution of an ensemble of ions (see Ch. 2). The cyclotron temperature of a single trapped ion, thermalised with the tank circuit, can thus be measured through repeated measurements of the temperature-related frequency shifts. In the currently utilized temperature measurement scheme at LIONTRAP, the modified cyclotron motion of an ion is excited to different radii r_{exc}, with the corresponding axial frequency shift measured. The shifts are amplified by the introduction of an additional $C_4 \approx 10^{-4}$ anharmonicity of the electrostatic potential by changing the optimal T_{comb}. The radius of an ion's motion after dipolar excitation depends on the phase relation between the excitation pulse and the ion's thermal motion in the following way [58]:

$$r_+^2 = r_{\mathrm{exc}}^2 + r_{\mathrm{therm}}^2 + 2 r_{\mathrm{exc}} r_{\mathrm{therm}} \cos(\phi). \tag{4.22}$$

The corresponding average frequency shift is then proportional to the squared excitation amplitude (see Eq. (2.20)):

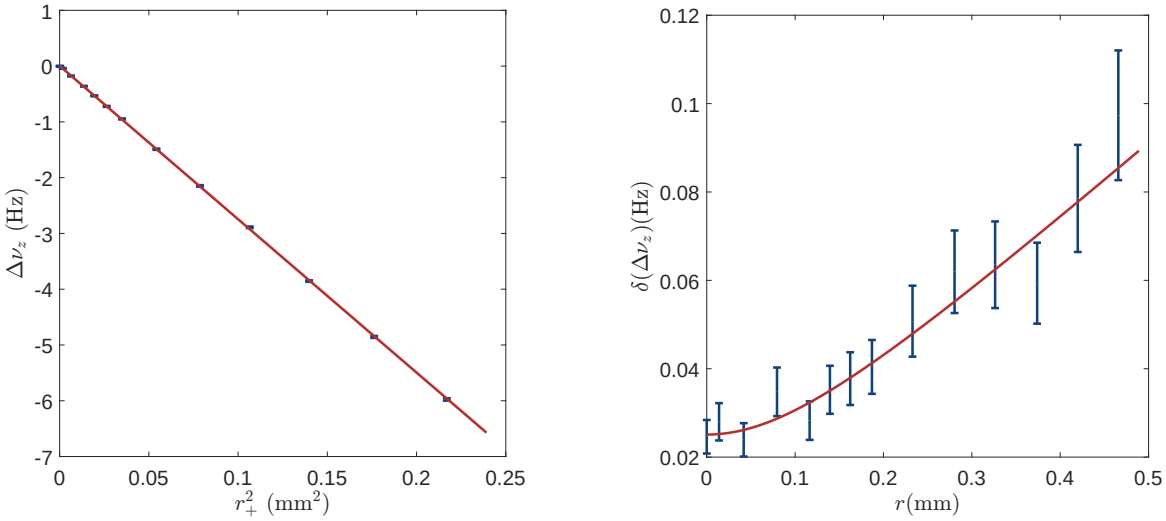

(a) (b)

Figure 4.9. An exemplary temperature measurement performed with the $^3He^+$ ion, with electronic feedback applied. The T_{comb} was changed so that $C_4 \approx -5 \cdot 10^{-4}$. In (a), the shift in axial frequency, resulting from the excitation of the modified cyclotron mode, is plotted against r_+^2. By fitting a linear function, the proportionality constant a is extracted; see the text for details. In (b), the jitter, specifically the standard deviation δ of each frequency shift $\Delta\nu_z$, is plotted against r_+. By fitting the data with the function described in the text (see Eq. (4.24)), the parameter b, which is proportional to the combination of a and T_+, is extracted. This measurement results in the equivalent axial temperature $T_z^{\mathrm{Fb\ on}} = 1.14(17)$ K. For the final combined temperature value (see Eq. (4.27)) a weighted average of multiple measurements is taken.

$$\langle \Delta\nu_z \rangle = a \cdot \langle r_+^2 \rangle = a \cdot \left(\langle r_{\mathrm{exc}}^2 \rangle + 2 \underbrace{\langle r_{\mathrm{exc}} r_{\mathrm{therm}} \cos(\phi) \rangle}_{=0} + \underbrace{\langle r_{\mathrm{therm}}^2 \rangle}_{\text{negligible}} \right) \approx a \cdot r_{\mathrm{exc}}^2. \tag{4.23}$$

Here, the term containing $\cos(\phi)$ becomes negligible since the angle ϕ is random for recurrent excitations. The proportionality constant a depends on the introduced C_4 and its value is cross-checked by a dedicated measurement, see Fig. 4.9a.

The jitter of the frequency shift originates from several effects. The uncertainty of the dip measurement and fluctuations in the voltage sources are independent of the amplitude of the ion's motion. The jitter that depends on the excitation radius contains information about the ion's temperature. Therefore, the jitter can be expressed by the following function:

$$\delta(\Delta\nu_z) = \sqrt{(b \cdot r_{\mathrm{exc}})^2 + c^2}. \tag{4.24}$$

The proportionality constant b extracted from the measurement relates to a and

the cyclotron temperature of the ion, T_+, via [58]:

$$b \approx 2a \cdot \underbrace{\sqrt{\frac{4}{\pi} - \frac{1}{2}}}_{\approx 0.88} \cdot \sqrt{\frac{\pi k_B T_+}{2m\omega_+^2}}. \tag{4.25}$$

Hence, the modified cyclotron temperature is derived as follows:

$$T_+ = \left(\frac{b}{1.76 \cdot a}\right)^2 \frac{2m\omega_+^2}{\pi k_B}. \tag{4.26}$$

For convenience, the temperature is expressed as the equivalent axial temperature, $T_z = \frac{\omega_z}{\omega_c} T_+$. Measurements are performed for both particles under two electronic feedback settings: on and off. For the final analysis, the weighted average for both ion species is used:

$$\begin{aligned} T_z^{\text{Fb on}} &= 1.3(3)\ \text{K}, \\ T_z^{\text{Fb off}} &= 3.8(8)\ \text{K}. \end{aligned} \tag{4.27}$$

Without feedback, the expected temperature is, in principle, the ambient temperature of the cryogenic environment, which corresponds to the temperature of the liquid helium - 4.2 K. However, the cryogenic amplifier of the detection circuit provides a slight intrinsic negative feedback, which can result in a temperature slightly below the ambient level [66]. For an additional cross-check, we compare the signal-to-noise ratios (SNR) of the resonator spectra with and without feedback, see Fig. 4.10. The parallel resistance of the detection circuit, as well as the temperature of the resonator scale with the feedback gain γ[1]:

$$R_{\text{RLC}}^{\text{FB}} = R_{\text{RLC}} \cdot \gamma, \tag{4.28}$$

$$T_z^{\text{FB}} = T_z \cdot \gamma. \tag{4.29}$$

Therefore, by taking a ratio of SNR, which are proportional to R_{RLC}, we can estimate the temperature change caused by the feedback. The measured $\gamma = \frac{1}{4.2}$ agrees well with the measured temperatures within their uncertainties.

4.5 Trap Alignment, Magnetron Measurement

The tilting mechanism is utilised to align the z-axis of the electrostatic quadrupole potential with the magnetic field. The axial frequency is maximized when the misalignment angle, θ, is minimized:

[1] These relations (Eq. (4.28) and Eq. (4.29)) are valid while the electronic noise of the cryogenic amplifier, which limits the lowest achievable temperature, is negligible. The temperature decreases monotonically with increasing feedback gain until a minimum value, after which the electronic noise is added and the temperature rises.

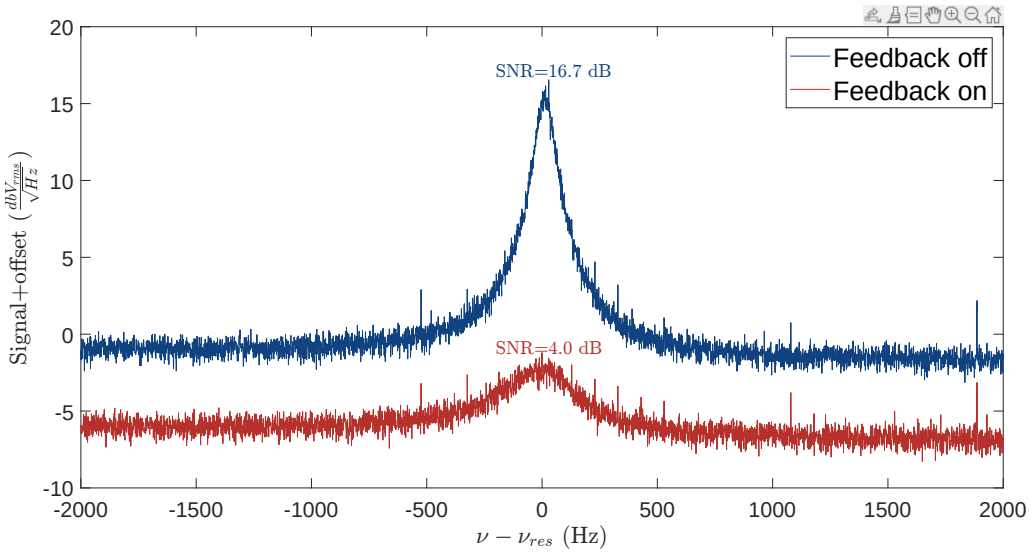

Figure 4.10. Two spectra of the resonator, with and without feedback. The signal level is decreased by about 5 dB when feedback is applied, since the mixer of the feedback loop changes impedance depending on a local oscillator connection. Without feedback, the signal-to-noise ratio (SNR) is about 16.7 dB, decreased down to 4 dB when feedback is applied. The estimated feedback gain is then $\gamma = \frac{1}{4.2}$, which agrees with the measured temperatures within their uncertainties.

$$\nu_{z,\theta} = \nu_{z,0}\sqrt{1 - \frac{3}{2}\sin^2\theta} \approx \nu_{z,0}\left(1 - \frac{3}{4}\theta^2\right) \implies \nu_{z,0} = \frac{\nu_{z,\theta}}{1 - \frac{3}{4}\theta^2}. \tag{4.30}$$

Therefore, the shift in the axial frequency is monitored by adjusting the three screws of the tilting mechanism. If the compensation B_2 coil is activated during the alignment process, the residual B_2 value must be checked afterwards, and if necessary, the coil must be recharged. This is because the movement of the trap system in the magnetic field causes the coil to change its angular position, altering the magnetic field in the trap region or potentially quenching the coil. The adjustment mechanism is described in [58]. During the ^{3}He mass measurement campaign, as a result of the alignment process, the axial frequency of the ion shifted by about +23.4 Hz relative to the starting value ($\nu_z^{start} = 498937$ Hz). Further adjustments were limited by the tension built up in the fiberglass rods of the tilting mechanism.

Interestingly, during the adjustment process, we noticed a change in the liquid helium consumption rate of the experimental apparatus. The position of the trap with the optimal θ corresponded to a higher consumption rate, suggesting a possible contact between the helium isolation shield and the nitrogen shield, which increased the boil-off rate of the liquid helium. After warming up and taking the experimental apparatus out of the magnet, we discovered that one of the tilting rods was broken,

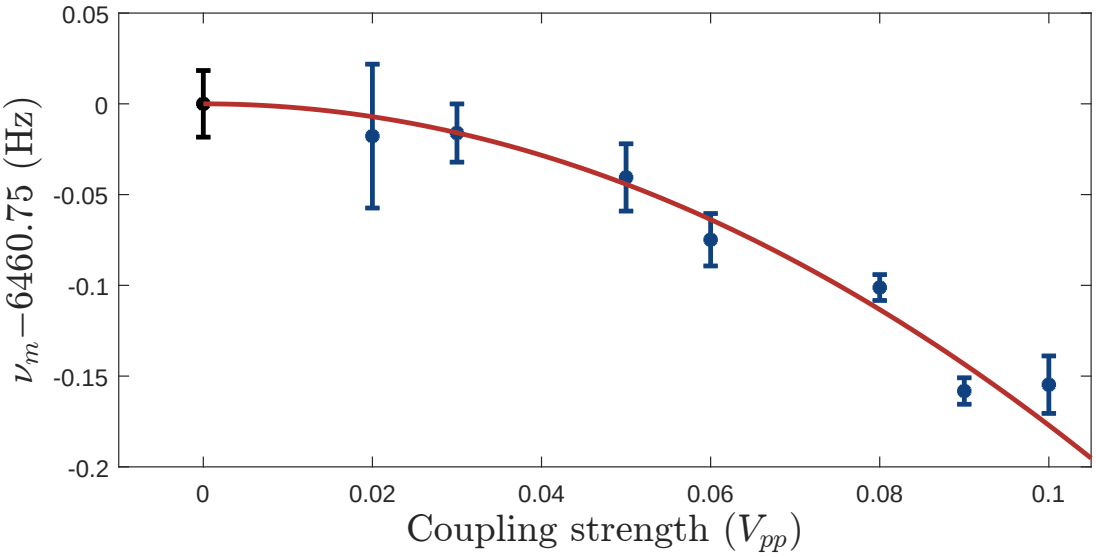

Figure 4.11. The magnetron frequency measurement of the helium ion. The magnetron double-dip spectra are recorded at different coupling strengths, expressed as the voltage of the coupling pulse, V_{pp}. The data is fitted with a quadratic[1] function to extrapolate the results to zero coupling energy, $V_{pp} = 0$ V. This measurement results in $\nu_- = 6460.75(2)$ Hz.

potentially causing the thermal contact.

Additionally, an effect previously observed in [58], involving a change in the resonator frequency ($\Delta\nu_{res} \approx 18$ Hz), was detected, along with the appearance of large noise peaks in the resonator spectrum.

The residual misalignment was estimated by comparing the magnetron frequency, ν_-, calculated from the axial and modified cyclotron frequencies using the relation that holds for an ideal trap: $\nu_-^{ideal} = \frac{\nu_z^2}{2\nu_+}$, with the value extracted from a dedicated ν_- measurement (see Fig. 4.11). A scan of magnetron double-dip measurements was performed at different coupling strengths to extrapolate the result to zero coupling energy. The measured value, in turn, contains information about the trap imperfections, θ and ϵ [60]:

$$\nu_-^{real} = \frac{\nu_z^2}{2\nu_+} \cdot (1 + \frac{9}{8}\theta^2 - \epsilon^2) = \nu_-^{ideal} \cdot (1 + \frac{9}{8}\theta^2 - \epsilon^2). \tag{4.31}$$

Assuming $\epsilon = 0$, the estimated misalignment is $\theta = 0.179(9)°$. Based on the trap manufacturing precision of approximately 10 μm and a trap diameter of 10 mm, the expected ellipticity is $\epsilon \approx 1 \cdot 10^{-3}$. Taking a conservative estimate of $\epsilon = 0.01$, one arrives at $\theta = 0.324(9)°$.

[1]The non-linearity of the shift is likely caused by the interaction between the Qxz and Dz components of the excitation drive.

The magnetron frequency measurements described above were performed several times throughout the campaign; however, unlike ν_+ and ν_z, ν_- is not measured regularly during the mass measurement. Instead, for the determination of the cyclotron frequency, ν_- is calculated from ν_+ and ν_z using the ideal trap relation. The effect of the estimated θ and ϵ is negligible in the ratio of the cyclotron frequencies of the two ions.

Chapter 5

Axial Phase Sensitive Method Development

The precision of the last measurement campaigns of the LIONTRAP experiment was limited by the systematic effect associated with the axial frequency determination - the image current effect, also known as the "dip lineshape" [7, 8]. The effect stems from the interaction of an ion with the detection LC-circuit. If the detection circuit is not perfectly tuned to the ion's axial frequency, the latter is "pushed", resulting in a systematic shift. While this effect is nominally corrected for by the lineshape model employed to fit the dip spectra, the model needs the exact parameters of the resonator as input. The uncertainty of these parameters introduces an error in the corrected axial frequency, which is subsequently transferred to the cyclotron frequency via the invariance theorem (see Eq. (2.12)).

To address this issue in the helium-3 measurement campaign, several options were considered. First, a new detection system was installed, consisting of a cryogenic low-noise amplifier and a resonator coil, see Sec. 3.4. This upgrade resulted in an increased Q-value of the detector. It is important to note that an increased Q-value itself does not reduce the effect. Actually, the effect is stronger for larger Q-values. However, a resonator with a higher Q-value offers better control, as the Q-value can, in principle, be decreased during a dip measurement using negative electronic feedback. Additionally, a combination of higher Q-value and more frequent resonator spectrum acquisition can lead to more precise determination of the resonator frequency. Although a higher Q-value might cause a shift in the axial frequency, such a shift can be accurately calculated and compensated for.

Another approach concerns data analysis. The lineshape shifts can be strongly suppressed by calculating the axial frequency of one ion from the axial frequency of the other, obtained from the dip fit, using the literature mass ratio (or, iteratively, the

measured ratio obtained classically using dip fits of both ions). This approach allows the transfer of the image current shift in equal strength to the other ion, resulting in maximum suppression in the ratio. In the helium-3 mass analysis, we ultimately employed this approach, which led to the suppression of the lineshape effect by a factor of more than 100. The analysis method is discussed in detail in Sec. 6.5.6. However, such treatment is only valid under the assumption that both ions are placed in the same electrostatic potential during the measurement. The limit that we can place on the possible voltage drifts during measurements imposes a limit on this analysis method, which is on the same level as the next most significant systematic uncertainty, arising from the image charge effect (see Tab. 6.5).

A completely new approach, however, would be to eliminate the need for the lineshape model entirely and measure the axial frequency analogously to the modified cyclotron frequency - namely, by implementing a phase-sensitive measurement. By shifting the resonator away from the ion's frequency for the phase evolution time, the image current effect is strongly suppressed (see Fig. 2.4). In such conditions, by replacing the noise-averaging dip measurement with peak detection for phase determination, we would shift the focus from accounting for image current shifts to addressing systematic effects that may arise when the particle has an excited axial radius. However, due to the highly compensated anharmonicities of the trap fields, these effects are not expected to be significant.

In this chapter, I describe the axial phase-sensitive (APS) method that I have implemented at LIONTRAP. It was not used in the final helium-3 mass measurement due to axial frequency shifts caused by the measurement technique. The source of these shifts, that will be detailed at the end of this chapter, is the voltage applied to the voltage-controlled capacitors of the axial cryogenic amplifier, which was used to shift the resonator away from the particle's frequency during phase evolution. However, this technical issue can be resolved by ensuring the proper filtering on the amplifier board. The proof-of-principle has been demonstrated, and the method can be implemented in next-generation Penning-trap experiments to overcome the limitations of the lineshape model.

5.1 Measurement Scheme

The idea behind the APS measurement is similar to the phase-sensitive methods used for ν_+ measurements. However, unlike PnP or PnA, only the initial excitation drive that imprints the phase is required, as the axial signal can be directly read out using the axial resonator. To suppress the image current shift and prevent cooling of the

axial motion during the phase evolution period, the coupling between the ion's axial motion and the resonator must be minimized. The measurement scheme is illustrated in Fig. 5.1.

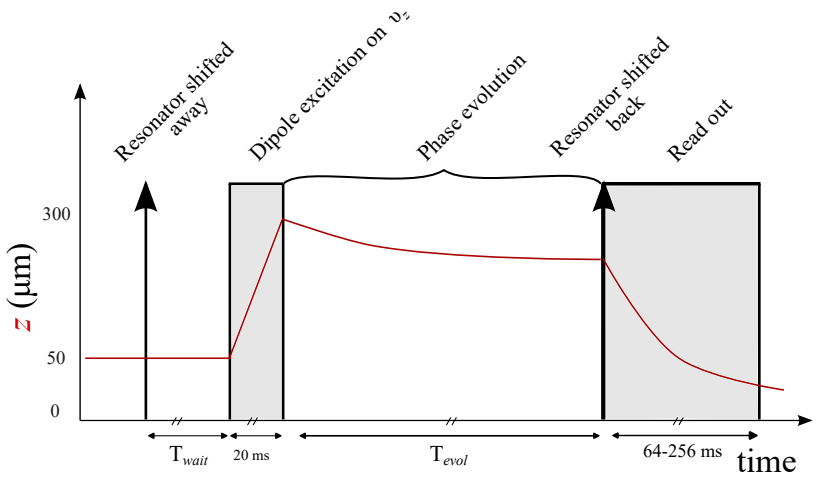

Figure 5.1. Schematic of the APS cycle. The progression of the axial amplitude, z, is shown in red. At the beginning of the cycle, the resonator is shifted by approximately 1.6 kHz away from the ion's axial frequency, ν_z. After the phase of the axial motion is imprinted by a dipolar excitation pulse, the phase evolves for an evolution time, T_{evol}, ranging from 10 ms to 1 s. Subsequently, the resonator is brought back to the ion's frequency, and the cooling peak signal is read out.

In the beginning, the resonator is shifted away from the ion's axial frequency by altering its effective capacitance through the application of voltage to the frequency switch of the cryogenic amplifier. After a waiting time of $T_{wait} \approx 100$ ms, the ion's axial motion is excited by a short dipole excitation pulse that simultaneously imprints the phase of the ion's motion. The axial phase then evolves freely at the axial frequency for a fixed time T_{evol}, which is set to either $T_{evol}^{min} = 10$ ms or $T_{evol}^{max} = 1$ s. Subsequently, the peak signal is read out and the phase is extracted from the complex Fourier spectrum. To extract the frequency, the phase difference $\Delta\varphi$ between two successive measurement cycles with different evolution times is considered. For a single ν_z measurement, five cycles are performed with T_{evol}^{min} and five cycles with T_{evol}^{max}. The phases corresponding to T_{evol}^{min} are averaged. The T_{evol}^{max} phases are unwrapped, and five ν_z^{single} are extracted and averaged to obtain final ν_z. The frequency ν_z must be corrected for the image current shift [66]. However, in APS measurements, the frequency difference between the particle and the resonator ($\Delta\nu > 1$ kHz) is sufficiently large that the impact of precise resonator frequency determination is strongly suppressed, see Fig. 2.4. This

contrasts with the dip measurement technique, where the uncertainty in ν_{res} is the primary limitation of the method.

The cryogenic switch (see Sec. 3.4), which toggles on and off to tune the resonator frequency to match the ion's frequency, is set differently for the two ions used in the measurement campaign. Thus, the switch states during the APS measurement are reversed for C^{4+} and $^3He^+$. To integrate the resonator switching into the measurement cycle, we designed a room-temperature switch board based on an 6N139 optocoupler. By applying a voltage controlled by the central trigger on the optocoupler, we were able to set the cryogenic switch to the state corresponding to the specific ion at the beginning of the APS cycle.

The strength of the dipole excitation signal must be optimized to minimize phase jitter. In other words, the signal should be strong enough to maximize the SNR of the detected signal, but not so strong that the residual anharmonicities of the trap potential begin to affect the measurement. To achieve this, we scan a range of excitation strengths, monitoring SNR of the detection peak and phase jitter, and select excitation strength corresponding to the minimum jitter.

5.2 Axial Amplitude Calibration

In order to evaluate the radius of the axial motion acquired by an ion after excitation, as well as to assess possible frequency shifts arising from field anharmonicities, we calibrate the radius in a manner analogous to the modified cyclotron radius calibration (see Sec. 4.3.1). For this measurement, in a trap with optimized B_2 and C_4, we introduce a C_4 on the order of $\mathcal{O}(10^{-4})$. In such a trap, the shifts in the axial frequency with increasing motional amplitude are caused by C_4 and residual C_6 [54]:

$$\frac{\Delta\nu_z}{\nu_z} = \frac{C_4}{C_2}\frac{3}{4d_{\text{char}}^2}z^2 + \frac{C_6}{C_2}\frac{15}{16d_{\text{char}}^4}z^4. \tag{5.1}$$

The C_6 after detuning can be calculated from the trap detuning parameter ΔT_{comb}. The radius of the axial motion is related to the excitation strength, $A = U \cdot t$, through the calibration constant, i.e., $z = \kappa_z A$. In the measurement, we perform APS measurements scanning a range of A values and record the axial phases, φ_z, for both T_{evol}^{min} and T_{evol}^{max}. Using ν_z^{dip} obtained from a dip measurement performed prior to the APS cycle, we unwrap the phases φ_z^{max} corresponding to T_{evol}^{max}.

Next, we calculate a set of expected phases, $\varphi_z^{max,exp}$, corresponding to the fixed C_4, a range of C_6 values around the expected value (calculated from ΔT_{comb}), and various amplitudes z determined by different calibration constants κ_z. By plotting the phase residuals, $\Delta\varphi_z = \varphi_z^{max,exp} - \varphi_z^{max}$, as a function of κ_z and C_6, we identify

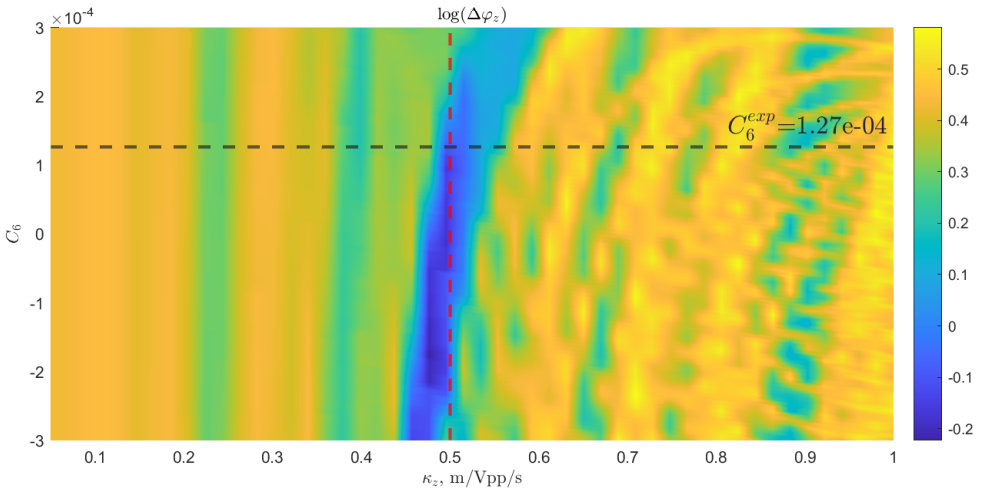

Figure 5.2. Axial amplitude calibration. APS measurements are performed with different excitation amplitudes in a trap with a deliberately introduced $C_4 = -1 \cdot 10^{-4}$. The phase differences, $\Delta\varphi_z$, defined as the difference between the unwrapped phases and the predicted phases (calculated based on the introduced C_4 and the expected C_6), are plotted as a function of the calibration constant κ_z and for a series of C_6 values near the expected value. The horizontal black dashed line corresponds to C_6^{exp}, as calculated for the ideal trap with the trap detuning parameter ΔT_{comb}. The minimum of $\Delta\varphi_z$ at C_6^{exp} corresponds to $\kappa_z = 0.50 \pm 0.05$ m/V$_{\text{pp}}$/s, as indicated by the vertical red dashed line.

the minimum of $\Delta\varphi_z$, which corresponds to the true value of κ_z. This procedure also confirms the predicted C_6 value. One exemplary measurement, done with carbon ion, is shown in Fig. 5.2. The procedure yields $\kappa_z = 0.50(5)$ m/V$_{\text{pp}}$/s.

Access to axial frequency measurements performed with a particle excited to an axial radius z offers the additional advantage of disentangling trap anharmonicities, namely C_4 and C_3, when combined with magnetron excitation scans (see Sec. 4.2.1). As mentioned there, the trap optimization process, which involves measuring axial frequency shifts due to the excitation of the particle's magnetron motion, results in a residual $C_4 = \frac{3C_3^2}{4C_2}$. In such a trap, an axial excitation scan produces shifted axial frequencies described by[1]:

$$\frac{\Delta\nu_z}{\nu_z} = \left(\frac{C_4}{C_2}\frac{3}{4d_{\text{char}}^2} - \frac{C_3^2}{C_2}\frac{15}{16d_{\text{char}}^2}\right) z^2 = -\frac{3}{8}\frac{C_3^2}{C_2^2 d_{\text{char}}^2} z^2. \tag{5.2}$$

Therefore, the combination of magnetron and axial excitation scans provides an additional tool to constrain trap anharmonicities and verify the consistency between measurement methods.

[1]Here, we assume that higher-order coefficients, such as C_6, are negligible.

5.3 Test Measurements

To test the APS measurement scheme and compare it with classical dip measurements, we performed an axial mass measurement. The idea is to measure the axial frequency ratio, R_z, of two ions and, using Eq. (2.7a), relate it to their mass ratio:

$$R_z = \frac{\nu_z(^{12}\mathrm{C}^{4+})}{\nu_z(^{3}\mathrm{He}^{+})} = \sqrt{\frac{4 \cdot m(^{3}\mathrm{He}^{+})}{m(^{12}\mathrm{C}^{4+})}}. \tag{5.3}$$

This approach allows us to identify potentially unnoticed systematic effects by comparing the R_z values measured with the APS and dip methods to the literature value [11] of the mass ratio.

The measurement sequence comprised recurring R_z measurements using both dip and APS techniques, repeated for a total of 70 cycles. The results of these measurements are plotted in Fig. 5.3. The data revealed that, while the APS measurement for the carbon ion is consistent with the dip technique, the axial frequency of the $^{3}\mathrm{He}^{+}$ ion, when measured with the APS technique, appears shifted relative to the dip measurement. Consequently, R_z^{APS} is significantly different from the ratio calculated using literature mass values, whereas R_z^{dip} is consistent with the literature data within uncertainty, given by the standard error of the mean.

Further investigation showed that the axial frequency shift $\Delta\nu_z = \nu_z^{\mathrm{APS}} - \nu_z^{\mathrm{dip}}$ depends on the voltage applied to the varactor diode of the cryogenic amplifier (see Sec. 3.4) and is the same for both ions when the voltage is set equally for them. Additionally, the shift decreases as the waiting time T_{wait} (see Fig. 5.1) between shifting the resonator and dipole ν_z excitation in the APS cycle increases. The dependency of $\Delta\nu_z$ on T_{wait} is illustrated in Fig. 5.4. The estimated decay time constant is ≈ 3 s. These observations suggest that the shift is caused by the switching of the varactor's bias voltage that couples through the coupling capacitors (see Fig. 3.8) and then discharges through the large trap biasing resistors.

In principle, with sufficient T_{wait}, the APS technique could be implemented alongside dip measurements in the mass measurement campaign. However, this would noticeably increase measurement time and negatively impact uncertainties associated with field drifts. Due to time constraints on further investigations, we decided to proceed with mass measurements using the classical dip measurement technique and suppress lineshape shifts analytically, as described in Sec. 6.5.6.

With this, the proof of principle was demonstrated by development of a phase-sensitive technique for axial frequency measurements. By ensuring the absence of parasitic voltage coupling during room temperature amplifier tests, this method can be implemented in next-generation Penning-trap experiments, overcoming the limitations

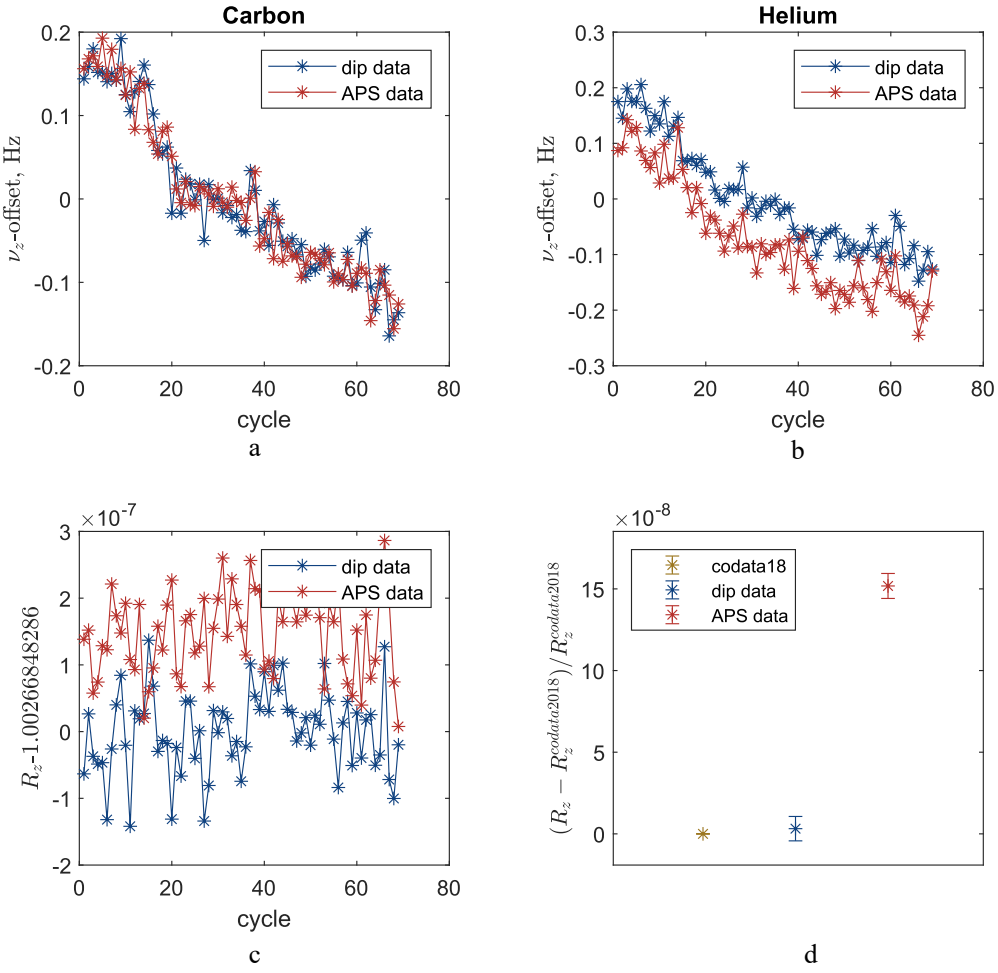

Figure 5.3. Measurement of the axial frequency ratio, R_z, performed with dip and APS techniques. Subfigures **a** and **b** show continuous ν_z measurements obtained with both methods for $^{12}C^{4+}$ and $^{3}He^{+}$ ions, respectively. Subfigure **c** presents a comparison of R_z measured using the dip and APS techniques, while subfigure **d** depicts mean R_z values compared to the R_z value calculated from literature CODATA mass values [11]. The measurement revealed that the axial frequency of the $^{3}He^{+}$ ion, when measured with the APS technique, appears to be shifted relative to that obtained via the dip measurement. Consequently, R_z measured with APS is significantly shifted from the literature value, whereas R_z extracted from the dip measurement is consistent with the literature data within uncertainty. See text for details.

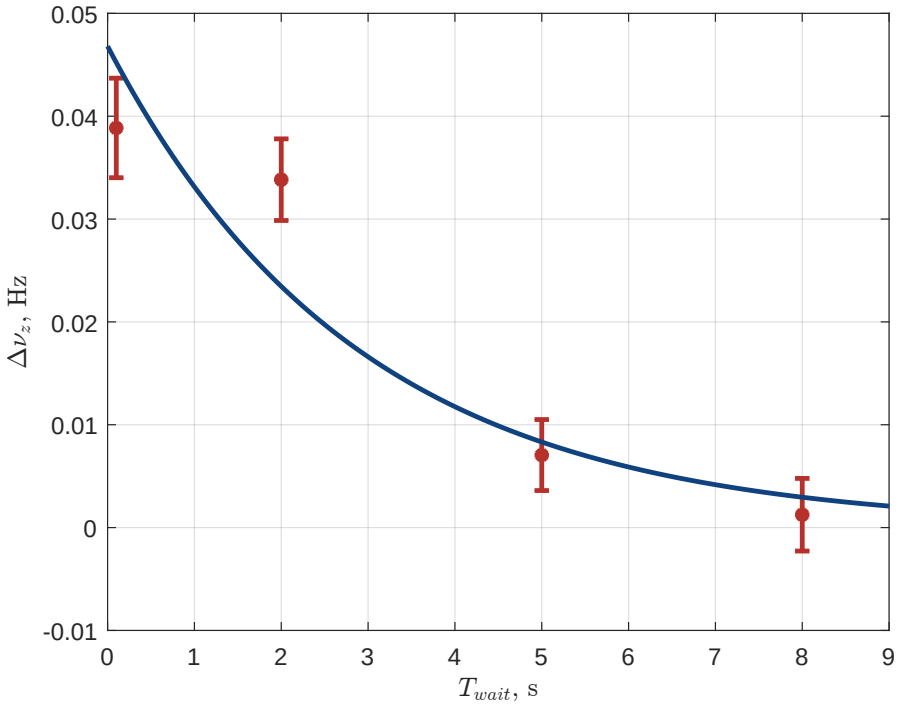

Figure 5.4. Axial frequency shift $\Delta\nu_z = \nu_z^{\mathrm{APS}} - \nu_z^{\mathrm{dip}}$ dependence on the waiting time T_{wait} between the shift of the resonator and the dipole ν_z excitation in the APS sequence. The data is fitted with exponential function. The decaying shift, with an estimated time constant of $\tau \approx 3$ s, suggests that it is caused by the switching of the varactor's bias voltage, which couples through the amplifier board's coupling capacitors and then discharges through the large trap biasing resistors.

of the lineshape model.

Chapter 6

^{3}He Mass Measurement

After completing the necessary trap preparation and characterisation measurements, the mass measurement begins. By this point, the pressure and temperature of the experiment are stabilised (see Sec. 3.1), ensuring maximal stability in the ion's frequencies.

6.1 Measurement Principle

Penning-trap mass spectrometry relies on measuring the cyclotron frequency of a charged particle in the trap: $\omega_c = \frac{qB}{m}$. To eliminate the magnetic field B in the equation, the ratio of cyclotron frequencies for two different species is measured. In LIONTRAP, the carbon ion serves as a reference due to its standardised mass in atomic mass units. To determine the mass of the particle of interest, such as $^3He^+$, with $^{12}C^{4+}$ as the reference, the following relation is employed:

$$m\left(^3\mathrm{He}^+\right) = m\left(^{12}\mathrm{C}^{4+}\right) \cdot \frac{\omega_c\left(^{12}\mathrm{C}^{4+}\right)}{\omega_c\left(^3\mathrm{He}^+\right)} \cdot \frac{1}{4}. \tag{6.1}$$

Here, a factor of $\frac{1}{4}$ corresponds to the charge ratio of helium and carbon ions. The charge states of the ions are selected such that the charge-to-mass ratio is nearly identical for both ions. This ensures the use of the same electrostatic potential for both particles, positioning them at the same location inside the trap and enabling the use of a single axial detector for both ions, since $\omega_z \propto \sqrt{\frac{q \cdot U_{\mathrm{ring}}}{m}}$. The remaining difference in frequencies is compensated for by fine-tuning the resonator's frequency using voltage-controlled capacitors. For $^3He^+$ and $^{12}C^{4+}$ and the constant ring voltage $U_{\mathrm{ring}} = -13.271$ V, the axial frequency difference is $\Delta\nu_z \approx 1328$ Hz. The approximate values of the eigenmode frequencies of ions in the PT are noted in Tab. 6.1.

Mass of the carbon atom is the standard of the atomic mass unit:

$$1\ \mathrm{u} = \frac{1}{12} m\left(^{12}\mathrm{C}\right). \tag{6.2}$$

Table 6.1. Approximate values of frequencies of the eigenmodes of ions, as well as the true cyclotron frequency, in the Precision Trap during the helium-3 mass measurement campaign. The ring voltage is set to U_{ring} =-13.271 V for both ions.

Ion	ν_m, Hz	ν_z, Hz	ν_+, Hz	ν_c, Hz
$^3\mathbf{He}^+$	6461	497594	19161572	19168033
$^{12}\mathbf{C}^{4+}$	6461	498922	19264007	19270468

Table 6.2. Electron binding energies B_i of carbon and helium-3 [87].

i	B_i (^{12}C), eV	B_i (^{3}He), eV
I	11.2602880(11)	24.58609272(14)
II	24.383143(12)	54.415324912(25)
III	47.88778(25)	
IV	64.49352(19)	

To calculate the mass of the ion $^{12}C^{4+}$, the mass of missing electrons [88] is subtracted and corresponding binding energies B_i are added:

$$m\left(^{12}\mathrm{C}^{4+}\right) = m\left(^{12}\mathrm{C}\right) - 4m_e + \sum_{i=1}^{4} B_i\left(^{12}\mathrm{C}\right). \tag{6.3}$$

Additionally, from the obtained $m\left(^3\mathbf{He}^+\right)$, the masses of neutral atom and nucleus are calculated using the following equations:

$$m\left(^3\mathrm{He}\right) = m\left(^3\mathrm{He}^+\right) + m_e - B_1\left(^3\mathrm{He}\right), \tag{6.4}$$

$$m\left(^3\mathrm{He}^{2+}\right) = m\left(^3\mathrm{He}^+\right) - m_e + B_2\left(^3\mathrm{He}\right). \tag{6.5}$$

The corresponding electron binding energies for carbon and helium are given in Tab. 6.2 [87]. For conversion of eV to u, the energy-mass equivalence principle is employed [88]:

$$(1\ \mathrm{eV})/c^2 = 1.07354410083(33) \times 10^{-9}\ \mathrm{u}. \tag{6.6}$$

6.2 Measurement Scheme

The measurement sequence comprises recurring cyclotron frequency ratio measurements:

$$R_{CF} = \frac{\omega_c\left(^{12}\mathrm{C}^{4+}\right)}{\omega_c\left(^3\mathrm{He}^+\right)}. \tag{6.7}$$

One measurement *cycle* yields one R_{CF}. These cycles are grouped into *runs*, which are temporally limited by the requirements of experiment maintenance, specifically the refilling of cryogenic liquids, nitrogen and helium, into the reservoirs of the magnet and experimental apparatus.

To measure one R_{CF}, the cyclotron frequencies of $^{3}He^{+}$ and $^{12}C^{4+}$ must be obtained. For this, the axial and modified cyclotron frequencies of each ion are measured during the cycle. Afterwards, using the invariance theorem (see Eq. (2.12)), the cyclotron frequencies of the two particles are calculated. The magnetron frequency, being the smallest of all the eigenfrequencies, is measured only occasionally throughout the entire measurement campaign, and its value for the invariance theorem is calculated from ω_+ and ω_z.

Ideally, cyclotron frequency measurements for both ions should be performed simultaneously at the same place to cancel out the effects of the drifting magnetic field. While this is not exactly possible due to the Coulomb repulsion of the ions, two ions of similar mass can be crystallised on a small common magnetron orbit [89, 34, 90]. However, due to the large mass mismatch of the $^{3}He^{+}$ and $^{12}C^{4+}$ combination, a fast shuttling technique is employed instead in this work. While the cyclotron frequency of one ion is being measured in the PT, the other ion is stored in one of the storage traps. The ions are then alternately shuttled between the precision and storage traps, so that the time between modified cyclotron frequency measurements for both ions is minimised.

One measurement run typically lasts a couple of days. The PnA excitation settings, namely the excitation radius r_+, are kept constant during a run but varied between runs to extrapolate the obtained R_{CF} to zero-excitation energy (see Sec. 6.3). Before the run, the experimental setup is prepared. The levels of cryogenic liquids in the apparatus are topped up to allow uninterrupted measurement for the maximum possible time. The experimental stabilisation system is activated: the pressure inside the apparatus, as well as the magnet, is stabilised, and the temperature around the magnet is kept constant. The filling process causes significant mechanical disturbances to the system; moreover, the sudden pressure change from this process leads to a temperature change in the experiment. Therefore, after the setup is prepared, a waiting time of 3 hours is set to allow the system to stabilise before measurements begin. Below, the steps of a measurement run, presented in Fig. 6.1, are described.

1. The resonator spectra are taken for each ion with two feedback settings: on and off. To do this, the ions are moved away from the resonator by adjusting the trap voltage. Afterwards, the trap voltages are restored to the optimal settings.

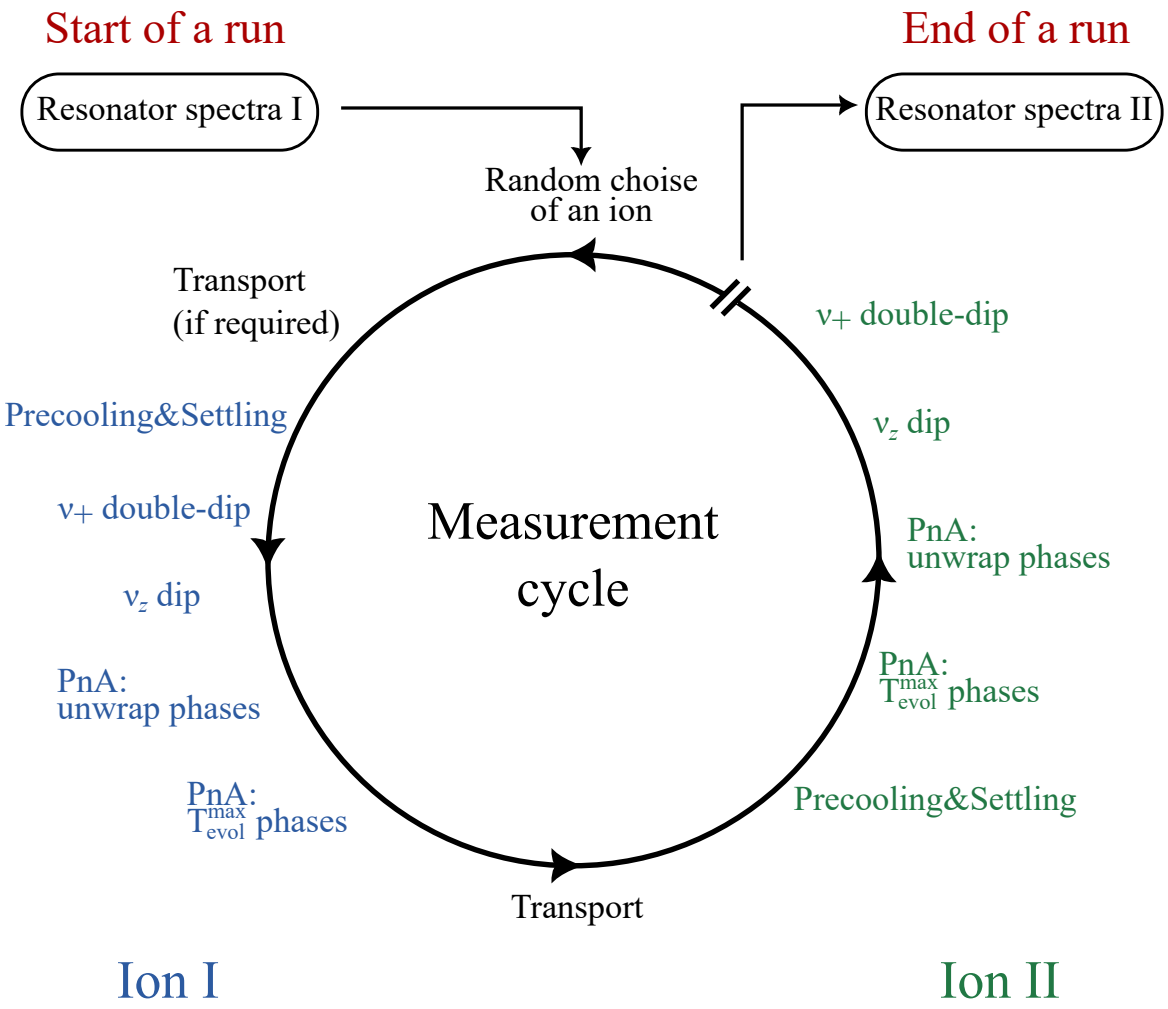

Figure 6.1. The diagram of the measurement run. At the start of a run the spectra of the empty resonators are taken. Afterwards, the measurement cycle begins with a random choice of the first ion (Ion I). If the chosen ion is in ST, it is being transported to PT, where its frequencies are measured after the motional modes are cooled and the voltage is settled after transport. Subsequently, the other ion (Ion II) is transported into the PT, and the measurements are performed in reversed order, so that the most critical ν_+ measurements are close together in time and the impact of magnetic field drifts is minimized. This cycle is repeated 30-40 times, typically until the cryogenic liquids needs to be filled into reservoirs of the experiment, which occurs every 2 days. At the end of a run, one more set of resonator spectra are taken. See text for details.

2. The ion whose cyclotron frequency is measured first is chosen randomly to avoid potential systematic shifts caused by magnetic field drift or voltage drifts in the trap. If the selected ion is already in the PT, no transport is required, and the measurement begins. Otherwise, the ions are shuttled so that the ion of interest (Ion I) is placed in the PT, while the other ion (Ion II) is stored in one of the storage traps (ST-I or ST-II). The eigenmodes of Ion I are cooled in the PT by coupling them to the axial resonator.

3. The modified cyclotron frequency ω_+ of Ion I is measured using the double-dip method. This value is not used to calculate ω_c for the cyclotron frequency ratio R_{CF}, but serves as an initial guess to unwrap phases in the PnA measurement, as well as to cross-check the PnA results.

4. The axial frequency ω_z is measured by taking the dip spectrum. The averaging time for both dip and double-dip measurements is set to 200 s, with a single spectrum acquisition time of 32.8 s, which corresponds to a bin width of approximately 30 mHz.

5. The PnA measurement of Ion I begins. Measurements with the shortest evolution time, T_{evol}^{min}, are performed first. This ensures that the measurements with the longest evolution time for both ions are conducted in close time proximity to each other. T_{evol}^{min} is varied between 100 and 200 ms in this campaign. A total of 6 PnA shots with the shortest evolution time are performed. Afterwards, measurements with the so-called unwrapping evolution times are conducted, with 1 PnA shot for each evolution time. The unwrapping evolution times in this measurement campaign are set to $T_{evol}^{unwrap} = \{0.5,\ 1,\ 2,\ 5,\ 10\}$ s. Finally, 6 PnA shots with the longest evolution time are performed. In this campaign, $T_{evol}^{max} = 20$ s.

6. The ions are shuttled so that Ion II is placed in the PT. After cooling the eigenmodes of Ion II, the PnA measurements are performed in reverse order: first with T_{evol}^{max}, then T_{evol}^{unwrap}, and finally T_{evol}^{min}.

7. The axial frequency ω_z of ion-2 is measured using the dip method.

8. The modified cyclotron frequency ω_+ of ion-2 is measured using the double-dip method. With this, one measurement cycle is complete. The procedure is then repeated starting from step 2 until it is time to refill the cryogenic liquids in the experiment.

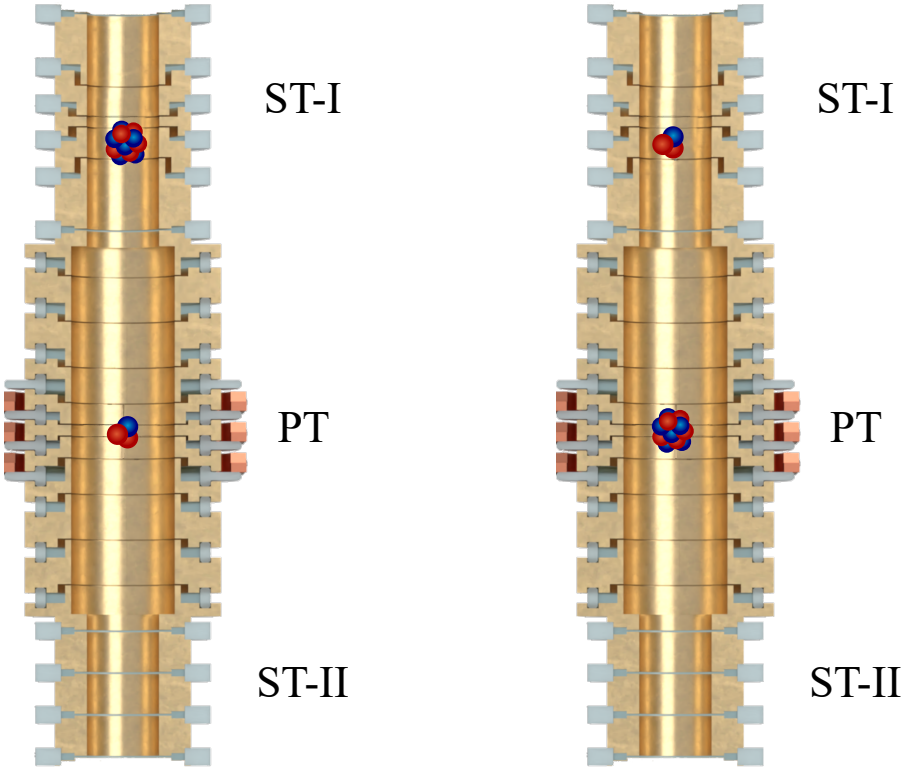

a Ion Pair I. Carbon is the upper ion. **b** Ion Pair II. Helium is the upper ion.

Figure 6.2. The mass measurement was performed with two different ion pairs. In (a), the first ion pair is shown, with the carbon ion positioned closer to the ST-II and referred to as the upper ion. In (b), for the second ion pair, the spatial arrangement of the ions in the trap is reversed, placing helium as the upper ion.

9. At the end of the measurement run, step 1 is repeated, namely obtaining the resonator spectra. This differs from previous mass measurement campaigns and is motivated by the fact that the uncertainty in ω_{res} was the dominant source of systematic error in those campaigns [58, 59].

The measurements were performed with two different ion pairs, each with a distinct spatial arrangement of ions in the trap (see Fig. 6.2). This approach is taken to avoid potential systematic effects arising from transport-associated voltage drifts, as well as from unnoticed contaminant ions. After the measurement with Ion Pair I, the experiment was briefly warmed up to 77 K due to a filling accident. It was subsequently cooled down back to 4 K, and the ions were produced anew, repeating the trap tuning and characterisation process described in Ch. 4.

6.3 Data Evaluation

The data analysis of the mass measurement campaign consists of several steps, which are described in this section.

6.3.1 Resonator Fit

The fit of the resonator spectrum allows for the extraction of several resonator parameters, which subsequently serve as input parameters in the fitting of dip and double-dip spectra. The fitted parameters include the quality factor Q, the resonance frequency ω_{res}, and the amplification factor A, which relates to the signal-to-noise ratio (SNR) of the resonator. Furthermore, the amplifier introduces an additional thermal noise term u_{off}, which is frequency-independent in first order.

The fit is performed by solving a non-linear least-squares curve fitting problem using the following function [55]:

$$\begin{aligned} u =& 10\log_{10}\left[A\cdot\mathrm{Re}\left(\frac{1}{1+iQ\left(\frac{\omega}{\omega_{res}}-\frac{\omega_{res}}{\omega}\right)}\right)+u_{off}^2\right]+ \\ &+\theta(\omega-\omega_{res})\ (\mathrm{dBVrms}). \end{aligned} \tag{6.8}$$

Here, the term θ is responsible for the slope of the transfer function. It is obtained independently by fitting the ends of the resonator spectra, with the resonator itself cut out, see Fig. 6.3a. These parameter is extracted for each spectra, and the mean value for the whole measurement campaign is set as a fixed input parameter for the subsequent resonator fits (see Fig. 6.3b). Other parameters, namely A, Q, ω_{res} and u_{off} are fitted for each run and used as input parameters for dip and double-dip fits in corresponding run.

The resonator spectra were taken twice during a run - in the beginning and at the end. For the first ion pair in the campaign the mean value of A, Q, ω_{res} and u_{off} for these two measurements is used as input parameter in dip fits. For the second ion pair, however, after the experiment was shortly warmed up to 77 K, a significant drift of the resonance frequency after the liquid helium filling process was recorded, as illustrated in Fig. 6.4.

The recorded frequency shift corresponds to a small parasitic capacitance of $C \approx 5$ fF. Although after about 1.5 hours after filling the drift is small, it is still not zero with within a timespan of a measurement run, which is typically a couple of days. Fig. 6.5 shows the difference of ν_{res} before and after a measurement run for two ion pairs. Although the mean $\bar{\Delta}\nu_{res}$ is also positive for the first ion pair, it can be compensated for by assigning a conservative error bar on the resonance frequency determination.

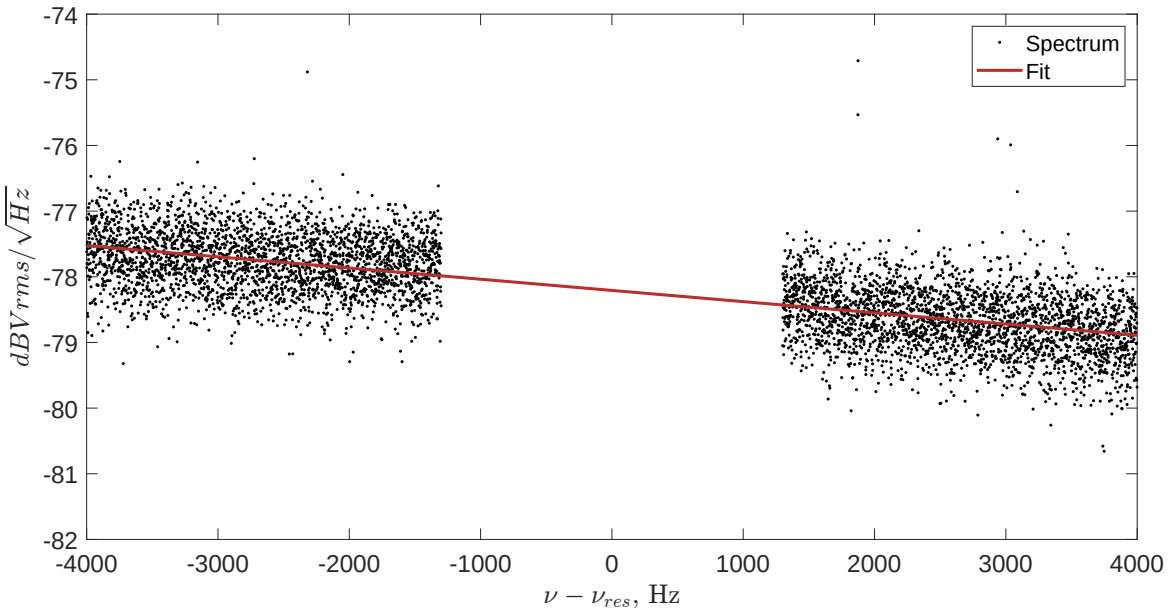

a Slope fit.

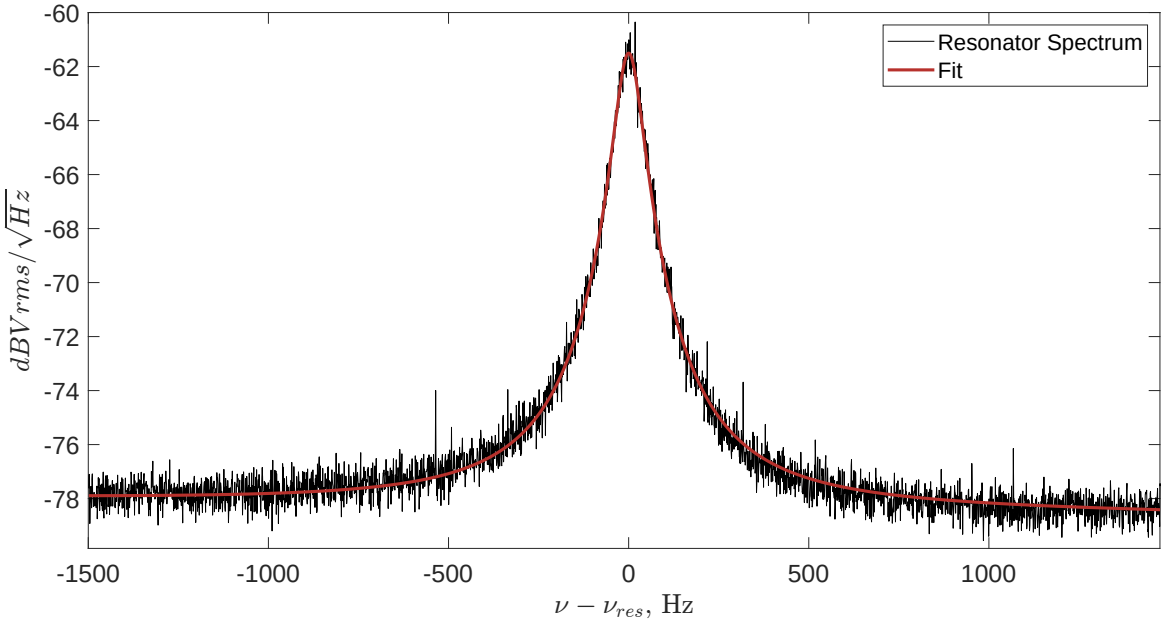

b Resonator fit.

Figure 6.3. Fit of resonator parameters. Subfigure **a** shows the extraction of the linear slope θ of the transfer function of the amplifier by fitting the resonator spectrum with the resonator cut out. Subfigure **b** shows the extraction of paramters A, Q, ω_{res} and u_{off} by fitting the resonance spectrum with a function from Eq. (6.8)

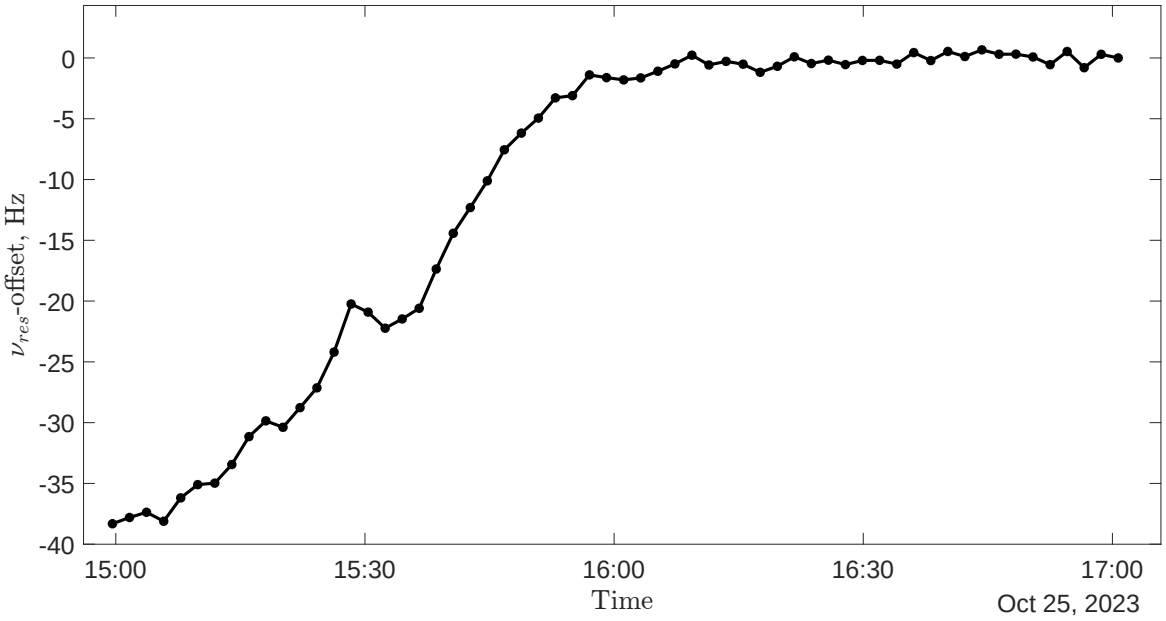

Figure 6.4. Resonator frequency drift after the filling of liquid helium to the apparatus of the experiment. The filling took place approximately 30 minutes before the start of the measurement.

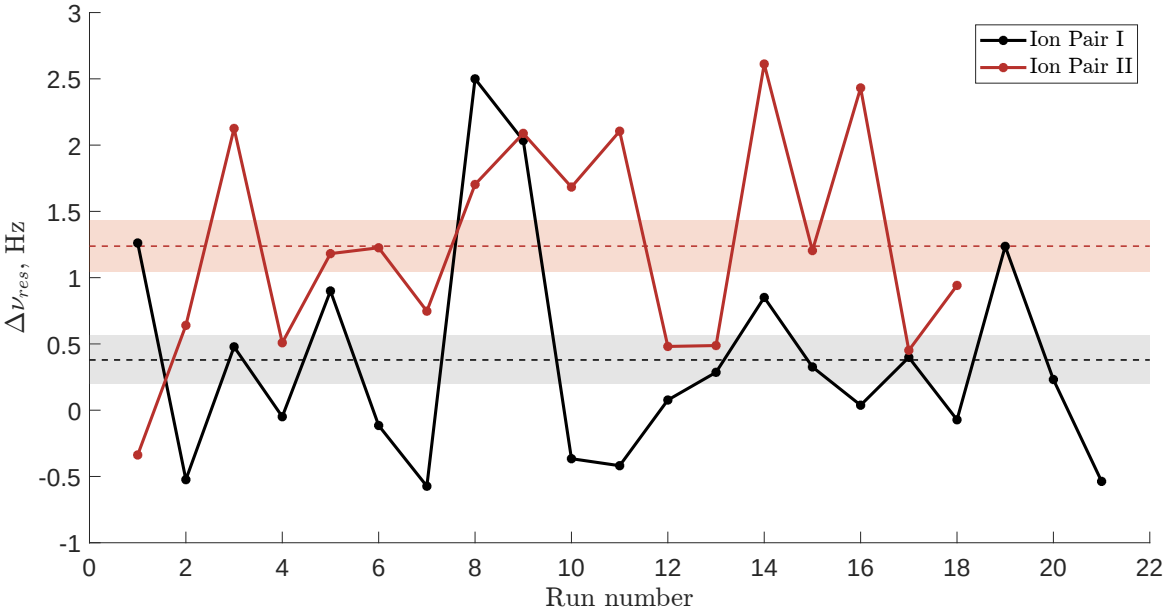

Figure 6.5. Shift of the resonator frequency $\Delta\nu_{res}$ between the beginning and the end of a run for two ion pairs used in the measurement campaign. Gray and red bands indicate the mean $\Delta\nu_{res}$ value for the Ion Pair I and II respectively, with the width of the band representing the standard error of the mean. $\bar{\Delta}\nu_{res}^{\text{IP-I}} = 0.4(2)$ Hz, $\bar{\Delta}\nu_{res}^{\text{IP-II}} = 1.2(2)$ Hz.

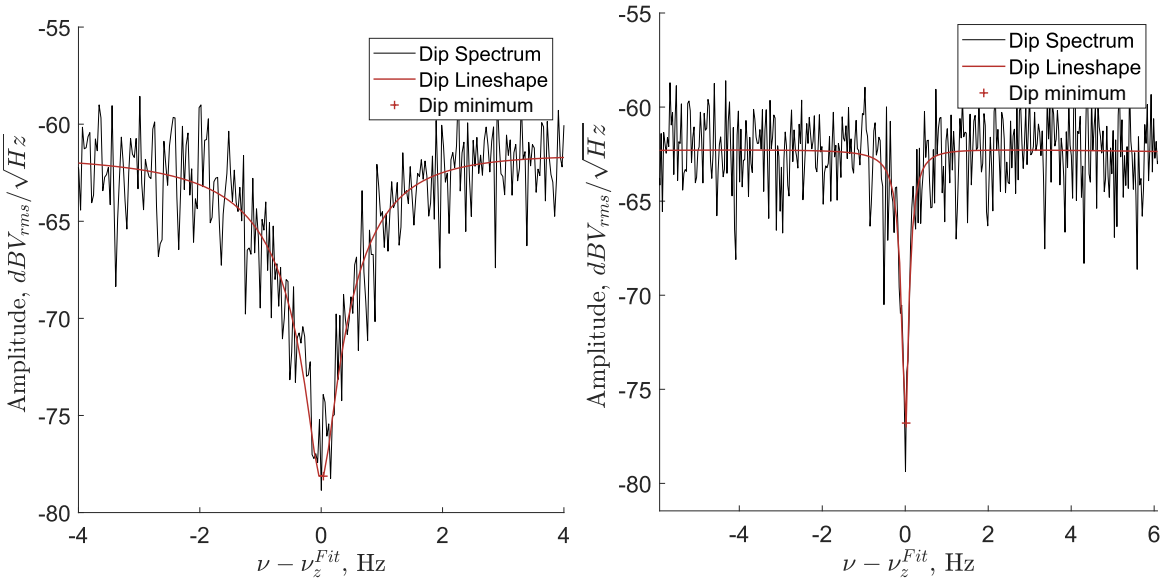

(a) Carbon Dip (b) Helium Dip

Figure 6.6. Axial dip spectra of $^{12}C^{4+}$ (a) and $^{3}He^{+}$ (b). The axial frequency is obtained by finding the minimum of the lineshape model (red), which uses A, Q, ω_{res}, u_{off} and θ extracted from the resonator fit as input parameters.

For the second ion pair, in order to determine the resonance frequency at the time of the dip or double-dip measurement, we interpolate ν_{res} by fitting a linear function through two points - the resonance frequencies measured at the start and at the end of a run. Finally, we prescribe a combined uncertainty on the resonance frequency $\delta\nu_{res} = 1.5$ Hz.

6.3.2 Dip and Double-Dip Fit

The next step in the data evaluation process is to fit dip and double-dip spectra. Dip fit allows the extraction of ω_z and double-dip fit is used to approximate ω_+ to provide an initial guess of the modified cyclotron frequency for the unwrapping procedure of the PnA. Although with dip fits we obtain ω_z for both particles in the ion pair, for the final cyclotron frequency ratio calculation the axial frequency, extracted from the dip fit, is used for only one ion. For the other, the value is calculated from the axial frequency of the first ion, see Sec. 6.5.6 for details. This approach allows the significant reduction of the image-current systematic effect. The exemplary dip spectra and corresponding lineshape model fits are plotted in Fig. 6.6.

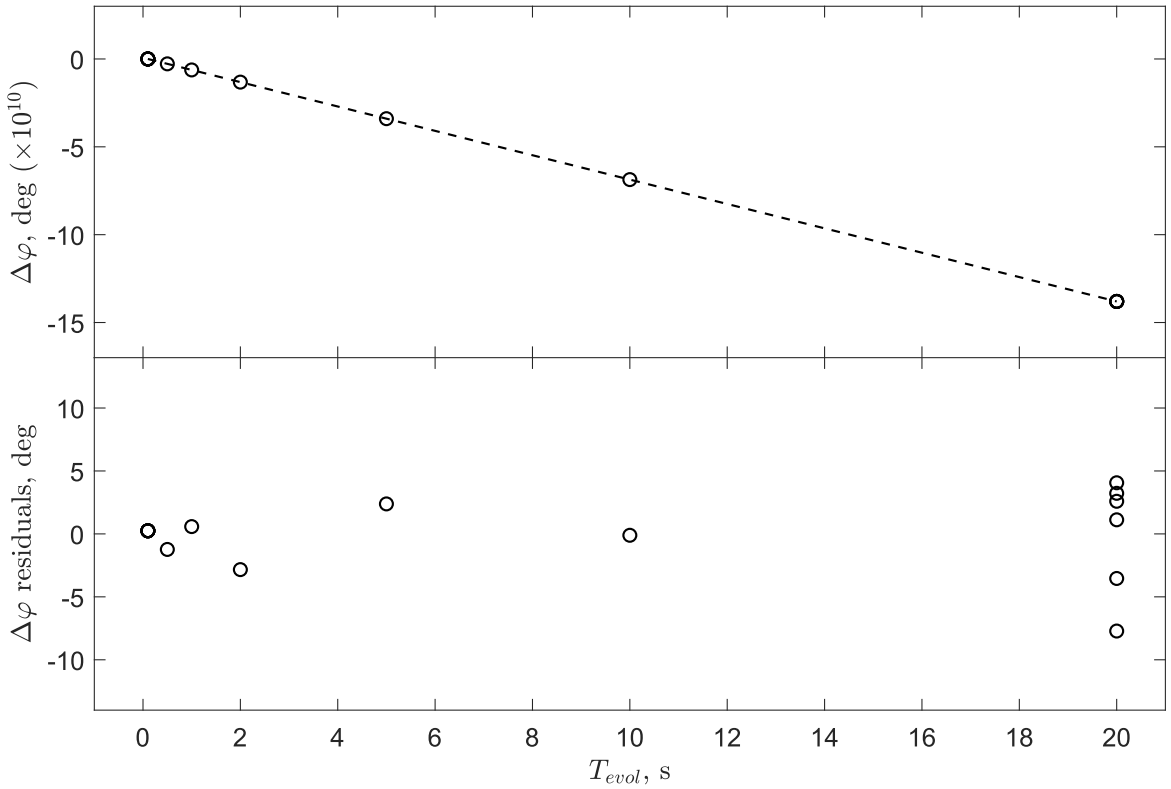

Figure 6.7. Unwrapping process of the PnA measurement. The phase φ_+ is measured at different evolution times T_{evol}. By comparing the predicted phase, calculated using the frequency ω_+^{DD} from the double-dip, with the measured phases, the latter are unwrapped. The linear slope is fitted though phases corresponding to minimal and maximal evolution times, resulting in determination of the modified cyclotron frequency ω_+.

6.3.3 PnA Unwrap

The PnA measurement results in a number of modified cyclotron phases for different evolution times T_{evol}. During a measurement cycle, 6 phases for the $T_{evol}^{min} = 0.1 \vee 0.2$ s are recorded, one phase for each unwrap time $T_{evol}^{unwrap} = \{0.5,\ 1,\ 2,\ 5,\ 10\}$ s and 6 phases for the maximal measurement time $T_{evol}^{max} = 20$ s.

In order to extract corresponding ω_+, the phases have to be unwrapped as they are detected modulo 2π, meaning the integer of revolusions of the ion after the T_{evol} has to be determined:

$$n(T_{\text{evol}}) = \left(\bar{\varphi}_{min} + \omega_+^{DD}(T_{evol} - T_{evol}^{min})\right)/2\pi. \tag{6.9}$$

Here, $\bar{\varphi}_{min}$ corresponds to the averaged phase of the minimal evolution time T_{evol}^{min}, and ω_+^{DD} - frequency measured with the double-dip.

The linear function is fitted through the unwrapped phases, see Fig. 6.7. For the evolution times $T_{evol} \geq 2$ s the slope of the fit function instead of the measured

ω_+^{DD} frequency is used to calculate the predicted phase. Finally, we obtain 6 ω_+^{single} frequencies by fitting 6 linear polynomials through all 6 φ_{min} and each individual φ_{max}. The resulting cyclotron frequency is calculated as an average of 6 ω_+^{single}. Hence, unwrapping phases φ_{unwrap} don't enter the resulting cyclotron frequency. An exclusion of particular ω_+^{single}, e.g. the ones measured in the closest time proximity to the transport of ions, from the average serves as a cross-check for voltage drifts associated with transport. For the final analysis, for $^3He^+$ ion phases corresponding to T_{evol}^{min} were excluded from consideration and a phase corresponding to $T_{evol} = 0.5$ s was used as φ_{min} instead. The cause was insufficient time for thermalisation of the axial motion of an ion with the tank circuit for the T_{evol}^{min}, which resulted in an increased jitter of the φ_{min}, see Sec. 6.7 for details.

6.4 Statistical Evaluation

The measurement campaign results in a number of cyclotron frequency ratios R_{CF} (see Eq. (6.7)). This section describes the statistical treatment of the data, including cuts and extrapolation of the cyclotron frequency ratio to the zero-excitation energy limit.

6.4.1 Data Cuts

Despite a carefully conducted trap optimisation process and ambient pressure and temperature stabilisation of the system, a number of R_{CF} are excluded from the data evaluation due to high error probability. We use a number of automatic filters to exclude faulty cycles, as well as manual cuts. The causes of data exclusion are reviewed below.

- **Noisy spectra.** Great precautions are taken to avoid parasitic electrical noise in the experimental 'signal' line. Those include, for example, having generally noisy devices, such as vacuum pumps, connected on separate power lines from the sensitive devices, such as high-precision voltage sources, signal analysers an others. USB connections to measurement PCs, which are often the source of significant noise, are established with cables providing galvanic electrical isolation of USB devices from the controller PC. Surfaces that might act as antennas transmitting parasitic RF noise are carefully grounded. Nevertheless, it is often very challenging to identify all noise sources. Fig. 6.8a illustrates the resonance spectrum with a broad 'walking' noise peak on the right side. Several times throughout the campaign the so-called noise-hunting process was conducted,

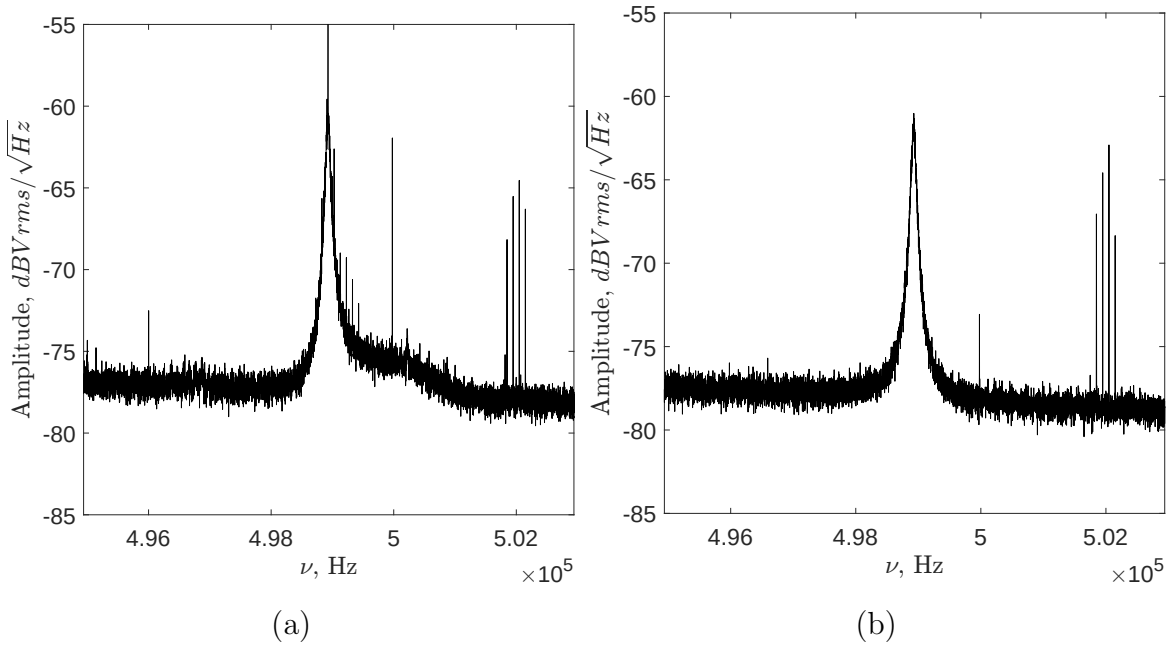

Figure 6.8. Resonance spectra. In (a), the broad noise peak is visible on the right side of the resonator. in (b), the spectrum is plotted after reconnecting the majority of the electrical devices to the experiment one at a time and reviewing the grounding of the experimental surfaces. The measurement cycles affected by the noise peaks are excluded from the analysis.

consisting of disconnecting the majority of the devices from the experiment and connecting them one by one, simultaneously monitoring the spectra in order to identify the noise source. In this campaign we observed that sending signal lines through the the BNC connector feed-through patch panel, which is mounted on the aluminium device rack, introduced a significant noise and had to be bypassed. Additionally, a careful isolation and grounding of the feedback line, including frequency mixer, attenuators and corresponding BNC cables had do be established. Despite all precautions, noise peaks appeared periodically and the affected measurements were excluded from the final data analysis.

- **PnA unwrapping errors.** Automatic data cuts are performed if the jitter (standard deviation) of the measured phase, corresponding to the longest evolution time $T_{evol}^{max} = 20$ s, exceeds 55°. This measure prevents the errors in ω_+ due to unwrapping problems. 2π unwrapping error causes fixed shift in the obtained frequency of ≈ 50 mHz. The resulting frequency is then notably shifted compared to an array of ω_+ measured during the run, and is cut out manually if it is not done by the automatic cuts.

- **Strong magnetic field drifts.** The stability of the magnetic field is greatly en-

hanced by the pressure stabilisation in the cryogenic reservoirs and temperature stabilisation of the area surrounding the magnet [58]. Nevertheless, the changes in the liquid helium and nitrogen levels, as well as mechanical disturbances during the cryogenic liquid filling process lead to increased non-deterministic magnetic field drifts. Although the magnetic field drift doesn't shift the final measured R_{CF} because of the randomised order of ions in the measurement cycle, large drifts are excluded from the data evaluation due to an increased jitter of the R_{CF}.

6.4.2 Planar Fit

In various runs, the nominal amplitudes r_+ of the modified cyclotron motion during the PnA pulse evolution for both ions are varied between 14.6 and 83.4 μm. These amplitudes depend on the excitation strength A: $r_+ = \kappa_+ A$, where κ_+ is a calibration constant, see Sec. 4.3.1, and A is the product of the duration t and amplitude U of the dipolar excitation pulse on ω_+ frequency. The variation of the amplitudes allows for the extrapolation of energy-dependent PnA shifts to the zero energy limit by performing a three-parameter *planar* fit to a number of combinations $A_{j,k} = \{A_j(^{12}\mathrm{C}^{4+}), A_k(^3\mathrm{He}^+)\}$ and corresponding cyclotron frequency ratios $R_{CF}^{A_{j,k}}$ [6]. The three-parametric fit has a following form:

$$R_{CF}^{A_{j,k}} = R_{CF}^{stat} + a \cdot A_j^2 + b \cdot A_k^2. \tag{6.10}$$

In total, there are 1000 individual cyclotron frequency ratios R_{CF} after cuts considered. The ratios with equal excitation parameters are grouped together and the mean value $R_{CF}^{A_{j,k}}$ serves as an input data point for the planar fit. The uncertainty of the point $\delta R_{CF}^{A_{j,k}}$ is given by the standard error of the mean. After grouping, 9 points $R_{CF}^{A_{j,k}}$ and corresponding excitation parameters enter the planar fit. The $R_{CF}^{A_{j,k}}$, $\delta R_{CF}^{A_{j,k}}$ and corresponding $A_{j,k}$ are given in Tab. 6.3.

The planar fit is illustrated in Fig. 6.9. The intersection of the fitted plane with the line corresponding to $A(^{12}\mathrm{C}) = 0$ Vpp $\cdot$ s and $A(^3\mathrm{He}) = 0$ Vpp $\cdot$ s, yields a statistical value for the cyclotron frequency ratio R_{CF}^{stat}, marked red. A more comprehensive interpretation of the plot is depicted in Fig. 6.10. There, the individual ratios $R_{CF}^{A_{j,k}}$ are corrected for the excitation energy and the residuals are plotted. The zero-line denotes the result of the planar fit R_{CF}^{stat} and the grey band represents the corresponding uncertainty.

The data undergoes a goodness of fit test, namely a test of the hypothesis that the data ($R_{CF}^{A_{j,k}}$) is normally distributed with a 95% confidence level [91]. We obtain a reduced $\tilde{\chi}^2 = \chi^2/d$ value, where d=6 is the number of degrees of freedom of the

Table 6.3. Input data of the planar fit. A_j and A_k denote the excitation strength of the PnA, and $R_{CF}^{A_{j,k}}$ - the mean of the cyclotron frequency ratios with the corresponding excitation parameters. The uncertainty of the ratio $\delta R_{CF}^{A_{j,k}}$ (in brackets) is given by the standard error of the mean.

$A_j(^{12}C^{4+}), \mathrm{Vpp}\cdot\mathrm{s}$	$A_k(^3He^+), \mathrm{Vpp}\cdot\mathrm{s}$	$R_{CF}^{A_{j,k}}$
0.0017	0.0017	1.005 344 079 956 4(119)
0.0097	0.0017	1.005 344 079 398 4(245)
0.0029	0.0029	1.005 344 079 970 6(219)
0.0073	0.0029	1.005 344 079 661 6(237)
0.0051	0.0051	1.005 344 079 961 8(134)
0.0029	0.0073	1.005 344 080 276 9(150)
0.0073	0.0073	1.005 344 079 938 5(131)
0.0017	0.0097	1.005 344 080 530 5(210)
0.0097	0.0097	1.005 344 079 943 5(210)

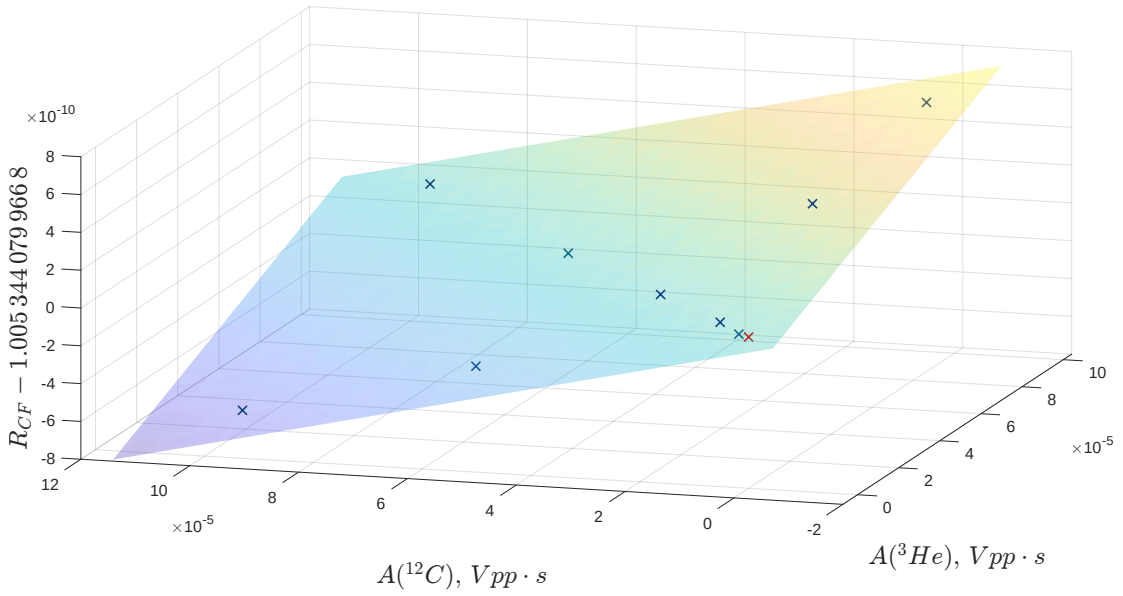

Figure 6.9. Planar fit. Cyclotron frequency ratios $R_{CF}^{A_{j,k}}$ for corresponding PnA excitation strengths $A(^{12}\mathrm{C})$ and $A(^3\mathrm{He})$ are marked blue. The result of the planar fit, R_{CF}^{stat}, corresponding to $A(^{12}\mathrm{C}) = 0$ Vpp$\cdot$s and $A(^3\mathrm{He}) = 0$ Vpp$\cdot$s is marked red. The error bars of the points are omitted due to their smallness on the scale of the plot.

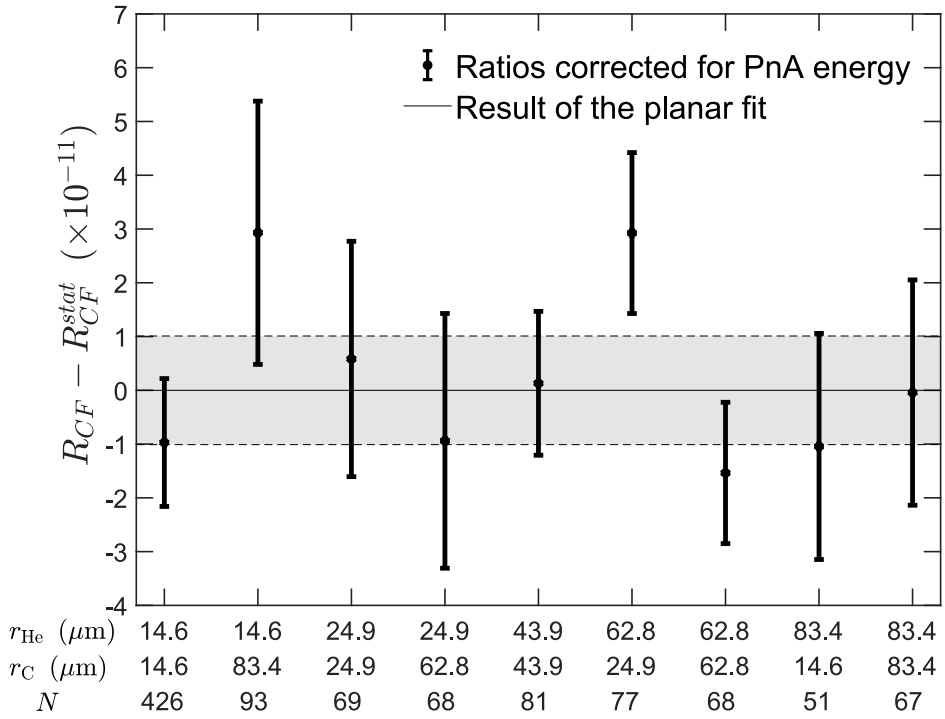

Figure 6.10. The averaged R_{CF} residuals, grouped by equal excitation strength. A 3-parameter fit allows the correction of R_{CF} to zero-excitation amplitude. On the x-axis, the corresponding excited cyclotron radii of helium (r_{He}), carbon (r_{C}) and the number of cyclotron ratios (N) in each data point are given. The error bars denote the standard error of the mean. The grey band denotes 1 σ uncertainty for the fitted frequency ratio.

Table 6.4. Excitation calibration constant κ_+ extracted from the planar fit and from direct measurements as described in Sec. 4.3.1.

Ion	Slope coefficient $1/\mathrm{Vpp}^2/\mathrm{s}^2$	κ_+ planar fit m/Vpp/s	κ_+ direct m/Vpp/s
$^{12}C^{4+}$	$-6.5(2) \times 10^{-6}$	0.0090(2)	0.0086(2)
$^{3}He^{+}$	$6.3(2) \times 10^{-6}$	0.0088(2)	0.0086(2)

fit. Is the assumed distribution is correct, $\tilde{\chi}^2$ should be of order of 1. The obtained $\tilde{\chi}^2 = 1.295$, and the probability of observing a value greater than that is 26% [92].

Additionally, the Kolmogorov-Smirnov goodness-of-fit hypothesis test is performed using the built-in Matlab function *kstest* [91]. The test does not reject the hypothesis that the data sample comes from a standard normal distribution at the 5% significance level.

The planar fit yields a statistical value of the cyclotron frequency ratio:

$$R_{CF}^{stat} = 1.005\,344\,079\,966\,8(101). \tag{6.11}$$

The planar fit additionally yilds the slope coefficients a and b, see Eq. (6.10). These coefficients provides new values for κ_+. We can, therefore, compare the newly extracted κ_+ with values obtained in independent measurements, see Sec. 4.3.1. The comparison is performed in Tab. 6.4. All values reasonably agree within their uncertainty. This shows that the utilisation of the same excitation line and function generator for both ions, as well as the proximity of the frequencies of these ions, justifies the usage of the combined $\kappa_+ = 0.0086(2)$ m/Vpp/s value in the analysis.

6.5 Systematic Effects

The extrapolated value R_{CF}^{stat} accounts for excitation energy shifts but still requires correction for various systematic effects, described in this section and summarized in Tab. 6.5.

6.5.1 Image Charge

The largest shift originates from the back-action of charges induced by the ion on the electrodes, resulting in shifted radial frequencies. This phenomenon, known as the image charge effect, has been extensively studied in [69], where a numerical simulation for the LIONTRAP trap geometry was compared to experimental measurements. The

Table 6.5. Relative shifts and uncertainties in R_{CF} due to various systematic effects. R_{CF}^{corr} denotes the ratio corrected for systematic shifts.

Effect	Rel. shift in ν_c ^{12}C (in ppt)	Rel. shift in ν_c ^{3}He (in ppt)	Rel. shift in R_{CF} $\left(\frac{R_{CF}^{corr}-R_{CF}^{stat}}{R_{CF}^{stat}}\right)$ (in ppt)	Rel. uncertainty (in ppt)
Image charge	-98.68	-24.80	73.88	3.69
Relativistic	-0.39	-1.53	-1.15	0.27
Magnetic inh.	0.06	0.24	0.18	0.92
Electrostatic anh.	0	0	0	0.16
Axial frequency	0	0	0	4.02
Total	-99.01	-26.09	72.91	5.54

simulation yields an relation between the shift in cyclotron frequency due to the image charge effect and the charge of the corresponding ion q:

$$\Delta\nu_c^{ICS} = -475.4(2.1) \cdot q \text{ (Hz)}. \tag{6.12}$$

The measurements comprised the determination of the magnetron frequencies of two ions with different charge states, $^{12}C^{6+}$ and p, using a phase-sensitive Ramsey-like technique. Both simulation and measurement showed an agreement within 5%. Later, the similar experimental measurement was repeated at LIONTRAP with $^{12}C^{6+}$ and d ions [59]. It was performed after the installation of the tilting mechanism and the B_2 compensation shim coil. The measurement showed an agreement with the simulations at a relative precision of 3.2%. Despite the agreement, the precision had not improved significantly compared to the previous ICS measurement[69], with the limiting factor being the uncertainty in the measured axial frequency ratio. For this work, we calculate the ICS using the simulation results (6.12) and give a conservative uncertainty of 5%. The resulting relative shift in the cyclotron frequency ratio is 74(4) ppt.

6.5.2 Relativistic Effect

Another systematic shift arises from the finite temperature of the ion, resulting in a relativistic increase in mass, see Sec. 2.4.1. Prior to each cycle the ions' axial motion is cooled through thermalization with the tank circuit. This temperature, equal to that of the surrounding cryogenic environment, is further reduced through negative electronic feedback. This way, the axial temperature of ions amounts to $T_z = 1.3(3)$ K. The temperature of the modified cyclotron motion, which mainly

contributes to the relativistic shift, is decreased by coupling it to the axial mode with a radio-frequency excitation drive [68]. The relativistic shift, which relatively scales with q/m^2, is particularly pronounced for the light ^{3}He ion. From the measured temperature we calculate the relative shift of R_{CF} to be -1.15(27) ppt.

6.5.3 Magnetic Inhomogeneity

The axial temperature mainly contributes to the frequency shift due to the residual quadratic component of the magnetic field. The utilization of the superconducting shim coil [7] minimizes the uncertainty of R_{CF} due to magnetic field inhomogeneity. Despite the partial discharge of the compensation coil (see Sec. 4.3.2) observed in this campaign, the regular monitoring of the B_2 inhomogeneity and recharging of the coil enabled the reduction of the relative uncertainty of R_{CF} down to 0.9×10^{-12}.

6.5.4 Electrostatic Anharmonicity

The seven-electrode design of the precision trap enables the achievement of an extremely harmonic electrostatic potential, effectively cancelling out the leading-order anharmonicities [6] (see Sec. 4.2.1). Consequently, the associated uncertainties are in the order of 10^{-13} on R_{CF}.

6.5.5 Magnetron Frequency Determination

The measurement of the magnetron frequency was conducted a few times throughout the entire campaign (see Sec. 4.5). Being the smallest of the eigenfrequencies (see Tab. 6.1), its uncertainty has the least impact on the cyclotron frequency. For the final R_{CF} value, magnetron frequencies of both ions are calculated from their axial and modified cyclotron frequencies: $\omega_- = \frac{\omega_z^2}{2\omega_+}$. Although this relationship holds true only for the ideal trap, not accounting for imperfections such as ellipticity and tilt of the experiment, the measured and calculated values deviate by less than 150 mHz, contributing only 10^{-14} to R_{CF}.

6.5.6 Axial Frequency Determination

The dominant systematic uncertainty in the recent LIONTRAP mass measurement campaigns has been the image current effect, also known as the "dip lineshape" [7, 8]. This effect stems from the interaction of an ion with the LC-circuit. If the detection circuit is not perfectly tuned to the ion's axial frequency, the latter is "pushed", resulting in a systematic shift. While this effect is nominally corrected for by the

lineshape model employed to fit the dip spectra, the model needs the exact frequency of the resonator ν_{res} as an input parameter. The uncertainty of the resonance frequency of the detection circuit introduces an error in the extracted axial frequency, which is subsequently transferred to the cyclotron frequency via the invariance theorem.

The uncertainty of the resonance frequency $\Delta\nu_{res} = 1.5$ Hz, established in Sec. 6.3.1, can be translated to the uncertainty of the axial frequency by tracking the shift in the ν_z extracted from a dip by varying the ν_{res}, which serves as an input parameter of the dip fit. From this, we extract the relative shift $\Delta\nu_z/\Delta\nu_{res}$, which equals to 1.3(2) mHz/Hz for $^3He^+$ and 4.9(1) mHz/Hz for $^{12}C^{4+}$. From this, using the invariance theorem, we calculate the uncertainty of the cyclotron frequency and subsequently the cyclotron frequency ratio: $(\delta R_{CF}/R_{CF})^{lineshape} = 1.02 \times 10^{-11}$.

In order to minimise the uncertainty associated with the axial frequency, a new analysis approach was implemented, which takes advantage of the similarity of the charge-to-mass ratios of both ions. Initially, R_{CF} is determined by obtaining ν_z of both particles through fitting the dip spectra:

$$R_{CF} = \sqrt{\frac{\nu_{+,\mathrm{C}}^2 + \nu_{m,\mathrm{C}}^2 + (\nu_{z,\mathrm{C}}^{dip})^2}{\nu_{+,\mathrm{He}}^2 + \nu_{m,\mathrm{He}}^2 + (\nu_{z,\mathrm{He}}^{dip})^2}}. \tag{6.13}$$

Subsequently, the obtained ratio is used to calculate a new set of $\tilde{R}_{CF}$, where ν_z of one arbitrary chosen particle is still obtained from the dip measurement (ν_z^{ion1}), while for the other particle, it is calculated from the initial cyclotron frequency ratio and ν_z^{ion1} via the equation:

$$\nu_z^{ion2} = \nu_z^{ion1}\sqrt{\frac{\nu_c^{ion2}}{\nu_c^{ion1}}}. \tag{6.14}$$

In order to show that such calculation allows us a significant suppression of the lineshape systematic effect[1], let us first consider the case, where the axial frequency of carbon is obtained from the dip measurement, and the one of helium is calculated using Eg. (6.14). We then show that the influence of choice of an ion is negligible. Considering Eg. (6.13) and Eg. (6.14), we obtain:

$$\tilde{R}_{CF} = \sqrt{\frac{\nu_{+,\mathrm{C}}^2 + \nu_{m,\mathrm{C}}^2 + (\nu_{z,\mathrm{C}}^{dip})^2}{\nu_{+,\mathrm{He}}^2 + \nu_{m,\mathrm{He}}^2 + \frac{1}{R_{CF}}(\nu_{z,\mathrm{C}}^{dip})^2}}. \tag{6.15}$$

Let R_{CF}^*, ν_z^* and ν_c^* be the 'true' (unaffected by the lineshape and a trap tilt) cyclotron frequency ratio, axial and cyclotron frequency respectively. Then, the axial frequency, obtained from a dip measurement can be expressed as:

[1] In addition to the lineshape, the multiplicative contributions of tilt and ellipticity imperfections add extra errors to ν_z^{dip}. However, they do not depend on a particle and drop out perfectly in the considered scaling method.

$$\nu_z^{dip} = \nu_z^* + \epsilon,\ \epsilon < \begin{cases} 7.4 \text{ mHz for C} \\ 2.0 \text{ mHz for He} \end{cases} . \tag{6.16}$$

Here, ϵ is calculated from $\Delta\nu_z/\Delta\nu_{res}$ obtained for each ion and the uncertainty of the resonance frequency $\Delta\nu_{res} = 1.5$ Hz. We also introduce the value

$$\delta = \frac{\left(\nu_z^{dip}\right)^2 - \left(\nu_z^*\right)^2}{\left(\nu_c^*\right)^2} = \frac{2\nu_z^*\epsilon + \epsilon^2}{\left(\nu_c^*\right)^2} = \begin{cases} 2.0 \cdot 10^{-11} \text{ for C} \\ 5.4 \cdot 10^{-12} \text{ for He} \end{cases} . \tag{6.17}$$

Now, considering Eq. (6.16) and Eq. (6.17), $\tilde{R}_{CF}$ can be expressed as:

$$\tilde{R}_{CF} \approx R_{CF}^* \sqrt{\frac{1+\delta_{\mathrm{C}}}{1+\delta_{\mathrm{C}} \cdot R_{CF}}}. \tag{6.18}$$

Here, δ_{C} corresponds to the carbon ion. The relative uncertainty of the obtained ratio is then:

$$\begin{aligned} \tilde{s} = \frac{R_{CF}^* - \tilde{R}_{CF}}{R_{CF}^*} = 1 - \sqrt{\frac{1+\delta_{\mathrm{C}}}{1+\underbrace{\delta_{\mathrm{C}} \cdot R_{CF}}_{\ll 1}}} \approx 1 - \sqrt{(1+\delta_{\mathrm{C}})(1-\delta_{\mathrm{C}} \cdot R_{CF})} \approx \\ \approx 1 - \sqrt{1+\underbrace{\delta_{\mathrm{C}}(1-R_{CF})}_{\ll 1}} \approx \frac{\delta_{\mathrm{C}} \cdot (R_{CF}-1)}{2}. \end{aligned} \tag{6.19}$$

Hence, a new analysis approach allows the suppression of the lineshape systematic by the factor:

$$\tilde{k} = \frac{\left(\delta R_{CF}/R_{CF}\right)^{lineshape}}{s} \approx 188. \tag{6.20}$$

Following the same logic, if the frequency of carbon is calculated, we obtain:

$$\tilde{\tilde{R}}_{CF} \approx R_{CF}^* \sqrt{\frac{1+\delta_{\mathrm{He}}\frac{1}{R_{CF}}}{1+\delta_{\mathrm{He}}}} \approx R_{CF}^* \left(1 + \frac{\delta_{\mathrm{He}}(1-R_{CF})}{2R_{CF}}\right). \tag{6.21}$$

$\tilde{\tilde{R}}_{CF}$ differs from $\tilde{R}_{CF}$ only in 10^{-14} order, therefore the choice of ion, which axial frequency is calculated, is arbitrary. In the final analysis we calculate the axial frequency of the carbon ion.

The relation from Eq. eq: ax1 is valid under the assumption that both ions are placed in the same electrostatic potential. R_{CF} and $\tilde{R}_{CF}$ agree within their uncertainties. To support this approach, we make sure that there were no significant trap voltage drifts present during the measurement. To do that, we evaluate modified cyclotron frequency data by excluding a number of phase measurements performed in a close time proximity to the transport of ions, when the trap voltages are being changed.

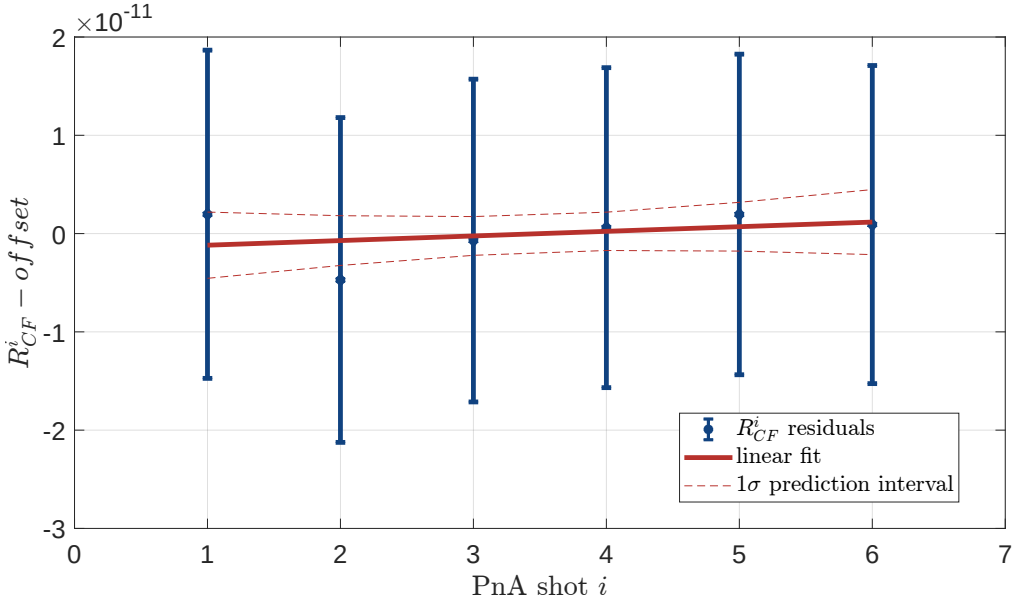

Figure 6.11. Influence of the voltage drifts on the cyclotron frequency ratio. The ratios R^i_{CF} are obtained by considering individual PnA shots (corresponding to T^{max}_{evol}) for $^{12}C^{4+}$ ion and averaged 6 PnA shots for $^{3}He^{+}$. The shot $i = 6$ is the closest to the transport, and $i = 1$ is the farthest. By fitting the data array linearly, the uncertainty of the R_{CF} due to potential voltage drifts is extracted from the 1 σ prediction interval of the linear fit. See text for details.

Such analysis is illustrated in Fig. 6.11. As mentioned in Sec. 6.2, during the PnA, the phase measurement shots with the longest evolution time T_{evol}^{max} for both ions are performed in the close time proximity, separated by the transport of ions (30s) and the cooling of the second ion's motion modes (1 min). If the transport process causes a voltage drift, by exclusion of the PnA shots closest to transport an effect on the R_{CF} can be detected. In order to reach sufficient statistical precision, we look at the individual PnA shots for $^{12}C^{4+}$ ion and averaged 6 shots of $^{3}He^{+}$. By that, we form a 1000×6 matrix of cyclotron frequency ratios, not corrected for the PnA excitation energy. By averaging the ratios, corresponding to a particular PnA shot of the $^{12}C^{4+}$ ion, we obtain 6 R_{CF}^{i}, where i - number of the used PnA shot. $i = 6$ is the shot, closest to the transport, and $i = 1$ - farthest. By linearly fitting the R_{CF}^{i} array we extract a 1 σ confidence interval, which is used to give uncertainty on the cyclotron frequency ratio due to potential voltage drifts: 4×10^{-12}.

6.6 Mass Value

Given the systematic shifts and uncertainties considered, the final corrected cyclotron frequency ratio is:

$$R_{CF}^{fin} = 1.005\,344\,080\,040\,1(101)_{\text{stat}}(56)_{\text{sys}}(115)_{\text{tot}}. \tag{6.22}$$

Using equation (6.1), we now derive the mass of the $^{3}He^{+}$:

$$m\left(^{3}\text{He}^{+}\right) = 3.015\,480\,768\,496(30)_{\text{stat}}(17)_{\text{sys}}(35)_{\text{tot}}\ \text{u}. \tag{6.23}$$

The mass of the atomic nucleus $^{3}He^{2+}$ and the neutral atom can be calculated using the electron mass [88] and electron binding energies [87] without loss of precision:

$$m\left(^{3}\text{He}^{2+}\right) = 3.014\,932\,247\,004(30)_{\text{stat}}(17)_{\text{sys}}(35)_{\text{tot}}\ \text{u}, \tag{6.24}$$

$$m\left(^{3}\text{He}\right) = 3.016\,029\,322\,011(30)_{\text{stat}}(17)_{\text{sys}}(35)_{\text{tot}}\ \text{u}. \tag{6.25}$$

The comparison of the mass of the neutral atom ^{3}He, as measured by different experiments, is depicted in Fig. 6.12. While the LIONTRAP result agrees well with the FSU results [27, 32, 28], recalculated using the latest proton's and deuteron's masses [88], it reveals a 6.1 σ deviation from the UW result [29, 30]. The literature CODATA2022 value [88], primarily given by the corrected FSU2017 measurement [32] is in agreement with the result of this work.

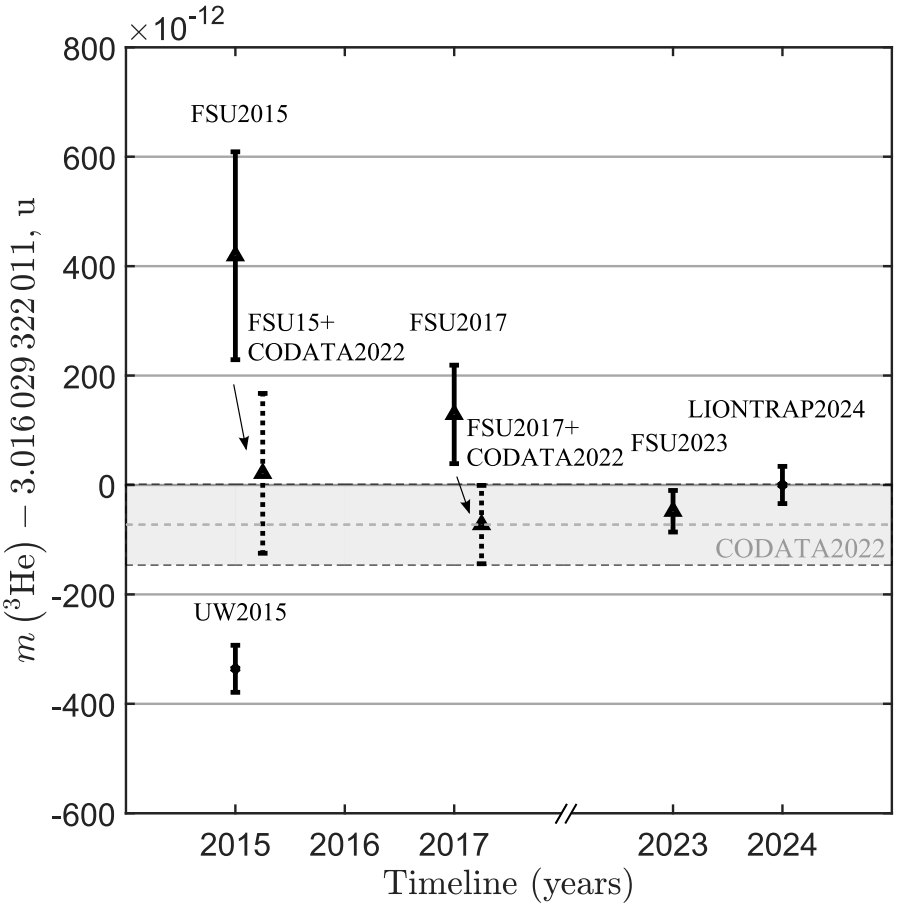

Figure 6.12. High-precision values of the atomic mass of ^{3}He. The initial discrepancy between FSU2015 [27] and UW2015 [30] is 3.9 σ. The result FSU2017 is obtained using the $m\,(^3\mathrm{He})\,/m\,(\mathrm{HD})$ ratio from [32], the $m\,(\mathrm{T})\,/m\,(^3\mathrm{He})$ ratio from [27], the deuteron mass from [30], and the proton mass from [31]. The FSU2017 and the FSU2015 results are also recalculated using current literature values for m_p and m_d from CODATA2022 [88]. The corrected FSU2015 and FSU2017 values, as well as the latest measurement FSU2023 [28], are consistent with the result of this work LIONTRAP2024. The results LIONTRAP2024 and UW2015 show a discrepancy of 6.1 σ.

6.7 Constraints of the Campaign

The precision of the obtained mass value is limited by the statical resolution. In total, 1000 cycles were used in the analysis, which resulted in 10^{-12} relative precision. In this section, the main sources of the R_{CF} jitter are investigated.

6.7.1 PnA Resolution

The significant constraint on the statistical precision of the R_{CF} comes from the resolution of the PnA technique used for the measurement of the ν_+ frequency. The resolution of the frequency $\delta\nu_+$ is limited by the jitter of the measured phase $\delta\varphi$:

$$\frac{\delta\nu_+}{\nu_+} = \frac{\delta\varphi}{360^\circ \cdot \Delta T_{evol} \cdot \nu_+}. \tag{6.26}$$

The phase jitter is obtained as a standard deviation of the difference of the subsequently measured phases (φ_i and φ_{i+1}), divided by the square root of two, often refereed to as Allan deviation:

$$\delta\varphi = \frac{\sigma(\{\varphi_{i+1} - \varphi_i\})}{\sqrt{2}}, \tag{6.27}$$

where σ is the standard deviation. The sources of the phase jitter in the PnA measurement are considered below.

1. **Imprinting the phase.** Due to the final thermal distribution of an ions modified cyclotron mode in the beginning of the PnA cycle, the inprinted phase after the fist PnA pulse, which excites the ion on a cyclotron radius, will jitter with $\delta\varphi_{therm}$ with approximately normal distribution for a small dipole excitation of $r_{exc} = 10$ μm [93]. This jitter reduces if the excitation radius r_{exc} gets higher, however at large radius various unwanted systematic shifts due to field imperfections and relativistic mass increase start to play a role. Typically, an amplitude equal to $3r_{therm}$ is used as a minimal excitation amplitude to get a small enough imprinting jitter. For the cyclotron temperature $T_+ = 50(11)$ K (see Sec. 4.4), achieved with the cooling method applied at LIONTRAP, the thermal radius $r_{therm} = \sqrt{< r_+^2 >}$ of an ion can be calculated using Eq. (2.15) from:

$$\frac{m\omega_+^2 r_+^2}{2} = k_B T_+, \tag{6.28}$$

resulting in $r_{therm} = 4(2)$ μm (for the helium ion). The minimal excitation amplitude used in the PnA measurement was 14.6 μm (see Sec. 6.4.2). Reducing the temperature of an ion is therefore a favourable method of reducing the imprinting jitter.

2. **Jitter during the phase evolution.** Here, several effects can be considered. The jitter is entailed by the initial thermal distribution of the modified cyclotron energy and caused by the relativistic mass increase, magnetic inhomogeneity and electrostatic anharmonicity. Since the PT is optimised so that the field imperfections are minimized (see Ch. 4), the jitter is dominated by relativistic effects. For ions excited to the same amplitude, the corresponding jitter decreases for increasing mass. The phase jitter increases linearly with the evolution time, although for small excitation amplitudes the jitter arising from the relativistic and field anharmonicity effects can be neglected. The magnetic field fluctuations during the phase evolution time cause a frequency jitter from shot to shot and pose limitations on the maximal phase evolution time. The magnetic field related effects are detailed in Sec. 6.7.2.

3. **The transfer to the axial motion.** The second pulse of the PnA sequence couples the modified cyclotron motion to the axial via a quadrupole excitation. The phase-spread of the thermal axial distribution will lead to an additional modified cyclotron phase jitter.

4. **Residual dipolar excitation of the second PnA pulse.** The second quadrupolar PnA pulse is executed through the excitation line connected to one half of the split correction electrode, which features dipole components in radial and axial directions, see Sec. 3.2. Therefore, the resonant quadrupole excitation at the frequency $\nu_+ + \nu_z$ competes with an off-resonant dipole excitation at ν_+ [55]. As a result, the phase relation between the modified cyclotron phase of the ion and the starting phase of the second PnA pulse leads to a systematic shift in the read-out phase. In order to prevent this, the phase of the first PnA pulse is chosen randomly in every cycle, so that the potential phase shift is translated in a phase jitter, which can also be neglected in comparison to other jitter sources [58].

5. **An intrinsic 'technical' readout phase jitter.** This jitter, originating from the limited SNR of the peak signal, is independent[1] from the ion's motion and had been studied by inducing an artificial peak signal with several kHz offset from the axial resonator, validating the numerical simulations of the effect [55]. The induced signal exponentially decreased with time, simulating a thermalizing excited ion. The effect scales with the signal-to-noise ratio of the peak signal.

[1] This is a non-trivial consequence of FFT being performed more than one inverse bandwidth after the quadrupolar excitation pulse.

When the amplitude of the second pulse is increased, the read-out jitter is reduced. However, the field imperfections start introducing an additional jitter if the amplitudes become big enough. For this reason, prior to the mass measurement the strength of the second PnA pulse is tuned to achieve the minimal jitter.

Table 6.6. The measured and Monte-Carlo simulated[2] phase jitter $\delta\varphi$ and signal-to-noise ratios (SNR) of the corresponding axial peak signal for $^3He^+$ and $^{12}C^{4+}$ ions at the smallest and largest excited radius r_+^{exc} for different phase evolution times T_{evol}. All phase jitters are given in degrees.

Ion	r_{exc}, µm	SNR, dB	Measurement		Simulation					
			$\delta\varphi_{\text{meas}}$ @ T_{evol}		$\delta\varphi_{\text{tech}}$	$\delta\varphi_{\text{therm}}$	$\delta\varphi_{\text{rel}}$ @ T_{evol}		$\delta\varphi_{\text{tot}}$ @ T_{evol}	
			0.1 s	20 s			0.1 s	20 s	0.1 s	20 s
$^3He^+$	14.6	13.9(4)	33(1)	26(1)	16(1)	18(2)	<0.1	1.1(1)	24(2)	24(2)
	83.4	20.4(4)	9(1)	11(1)	9(1)	3(1)	<0.1	6.1(3)	9(1)	11(1)
$^{12}C^{4+}$	14.6	22(1)	12(1)	14(1)	8(1)	9(1)	<0.1	1.0(1)	12(1)	12(1)
	83.4	23(1)	9(2)	11(1)	7(1)	1.5(2)	<0.1	2.9(3)	7(1)	8(1)

The measured and Monte-Carlo simulated jitters for both ions are listed in Tab. 6.6. As mentioned above, a number of effects, such as jitter due to the relativistic mass increase or due to magnetic field drifts, scale with phase evolution time. Subsequently, the total expected jitter is slightly larger for longer T_{evol}. However, during the measurement campaign we've noticed that for $^3He^{1+}$ ion the phase jitter corresponding to the smallest excited radius $r_+^{exc} = 14.6$ µm and phase evolution time $T_{evol}^{min} = 0.1$ s is larger than that one of the long $T_{evol}^{max} = 20$ s, and significantly exceeds the value expected from numerical simulations. The cause of this effect was shown to be an insufficient waiting time T_{wait} between the switching on of the electronic feedback and the PnA pulse, see Fig. 6.13. The waiting time was set to 1 second for the most measurements in the campaign. The cooling time constant $\tau = 0.3$ s (corresponding to the -3 dB dip-width of 0.52 Hz) is larger for ligher helium ion. In principle, 1 second should be still enough for the ion to thermalise with the axial detector, however due to delay times of the feedback system the time was shown to be insufficient. The measurements with longer phase evolution times $T_{evol} \geq 0.5$ s were unaffected by this because during longer evolution times the axial mode of the ion was able to thermilise with the tank circuit. It should also be noted, that this problem only affected axial

[2]The simulation for the long evolution times $T_{evol} = 20$ s doesn't include the effect of the drifting magnetic field, discussed in Sec. 6.7.2.

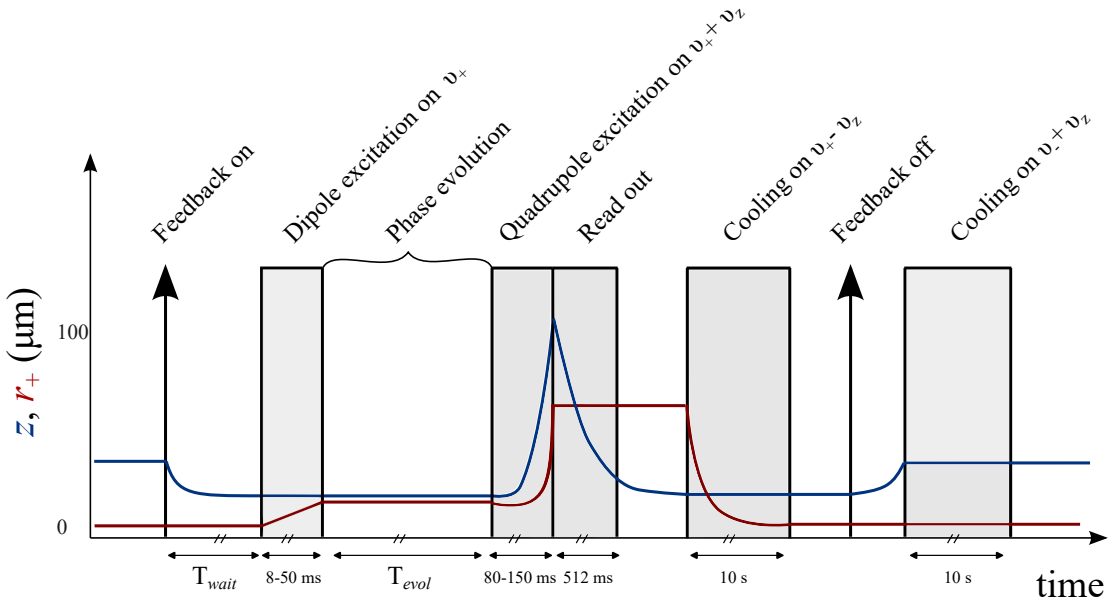

Figure 6.13. Schematic of the PnA-cycle. The plot shows the progressions of the axial amplitude z (blue line) and the modified cyclotron radius r_+ (red line). The waiting time between switching on the electronic feedback and the first PnA pulse T_{wait} was set to 1 second during the majority of the measurements. That was later shown to be insufficient for the cooling of the axial motion of $^3He^+$ ion and resulted in an increased phase jitter of helium for smallest excitation amplitudes, see text for details.

temperature, and not the modified cyclotron one, since the latter was cooled earlier, when the feedback was on for a long time. The described effect was discovered at the end of the measurement campaign. In order to avoid potential systematic shifts due to increased axial temperature of one ion, we excluded phases corresponding to the smallest evolution times for $^3He^{1+}$ ion from the analysis, using one of the 'unwrapping' phases corresponding to $T_{evol} = 0.5$ s instead. Since 6 PnA shots were performed with $T_{evol}^{min} = 0.1$ s and only one with that one of 0.5 s (see Sec. 6.3.3), the statistical precision of the method decreased slightly by factor of $\sqrt{\frac{12}{7}}$ =1.3.

In order to further support the obtained results and make sure that the discovered axial cooling problem didn't cause the significant shift of the R_{CF}, we compare its value obtained with different minimal phase evolution times for $^3He^+$, see Fig. 6.14. T_{evol}^{min} for $^{12}C^{4+}$ is kept constant at 100 ms. On the level of the statistical precision no significant shift in R_{CF} is observed, which further strengthens trust in the final values.

The expected resolution of the PnA method can be estimated from measured phase jitters given in Tab. 6.6. For the minimal excitation amplitude $r_{exc} = 14.6$ µm for $^3He^+$ the uncertainty of the 0.5 s phase is approximately 26°. For the long evolution

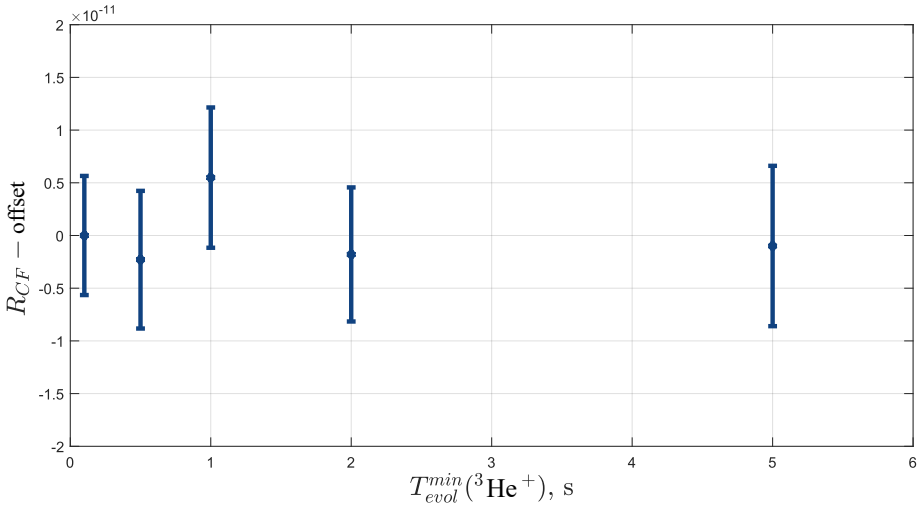

Figure 6.14. Comparison of the cyclotron frequency ratios R_{CF} with different minimal phase evolution times T_{evol}^{min} used for $^3\mathrm{He}^+$ in the analysis of the PnA measurement. T_{evol}^{min} for $^{12}\mathrm{C}^{4+}$ is kept constant at 100 ms. The values are calculated as the mean of the ratios, shifted in accordance with PnA excitation energy, and the errorbars of the points denote the standard error of the mean, meaning the depicted analysis is performed without a planar fit (see Sec. 6.4.2). The absence of significant shifts in the extracted ratios strengthen the certainty in extracted values. For the final analysis $T_{evol}^{min} = 0.5$ s is used as minimal phase evolution time for $^3\mathrm{He}^+$ ion, see text for details.

time, which was measured 6 times, the uncertainty is reduced and equals $26°/\sqrt{6}$=11°. This results in a resolution for the modified cyclotron frequency of $\delta\nu_+/\nu_+ \approx 2\cdot10^{-10}$. Likewise, for carbon the phase jitter results in $\delta\nu_+/\nu_+ \approx 5\cdot10^{-11}$. Finally, the uncertainties for two ions can be added in squares, assuming their independence, resulting in cyclotron frequency resolution:

$$\left(\frac{\delta R_{CF}}{R_{CF}}\right)_{\text{PnA, 14.6 µm}} \approx 2.1\cdot10^{-10}. \tag{6.29}$$

The observed jitter is, however, slightly higher: $2.5\cdot10^{-10}$. Therefore, other factors contributing to the statistical limitation of the frequency ratio have to be considered.

6.7.2 Magnetic Field Jitter and Drifts

The magnetic field jitter might add to the simulated phase jitter for the long phase evolution times. In order to estimate the effect, the $\delta\varphi_{\text{meas}}$ values for the phase evolution times 0.1 s and 20 s are compared. For the $^{12}C^{4+}$ ion, at $r_{\text{exc}} = 14.6$ µm the additional jitter during T_{evol} equals $\sqrt{(14°)^2-(12°)^2} = 7.2°$. Considering the simulated jitter, which stems from the relativistic effect at long evolution time $\delta\varphi_{\text{rel}} = 1°$, the jitter arising from magnetic field fluctuations is estimated $\varphi_{\text{magn}} = \sqrt{(7.2°)^2-(1°)^2} \approx 7.1°$. This translates to a shot-to-shot magnetic field stability $\frac{\delta B}{B} = 5.2\cdot10^{-11}$. For helium, the measurements with increased waiting time between switching on the feedback and PnA cycle showed that at $r_{\text{exc}} = 14.6$ µm the jitter is almost equal for long and small evolution times, meaning that the effect of the jittering magnetic field doesn't contribute to the final precision and one averages mostly over the thermal energy distribution of the ion.

In turn, in the above consideration the effect of slow magnetic field drifts during the PnA cycles is suppressed, because the jitter is calculated from considering differences of two adjacent phases. Nevertheless, drifts play a role for the R_{CF} resolution. The NMR magnets are known for exhibiting decaying magnetic field, observed, for example, in the experiment PENTATRAP [94], that is likely happens due to flux-creep and diffusion, particularly for multi-filament magnets. For the LIONTRAP setup, however, this effect of the decaying field is not observed, but the field still drifts noticeably during a run, see Fig. 6.15. Additionally, jumps of the cyclotron frequency in-between runs denote the sudden change in the magnetic field, which is likely caused by mechanical disturbances during filling of the cryogenic reservoirs. The most likely explanation of the drifts are long term effects of the thermalization of the setup, and other effects such as the changing level of the cryo-liquids in the reservoirs. The typical cyclotron frequency drift between two cycles for the ion is 8 mHz. The center times

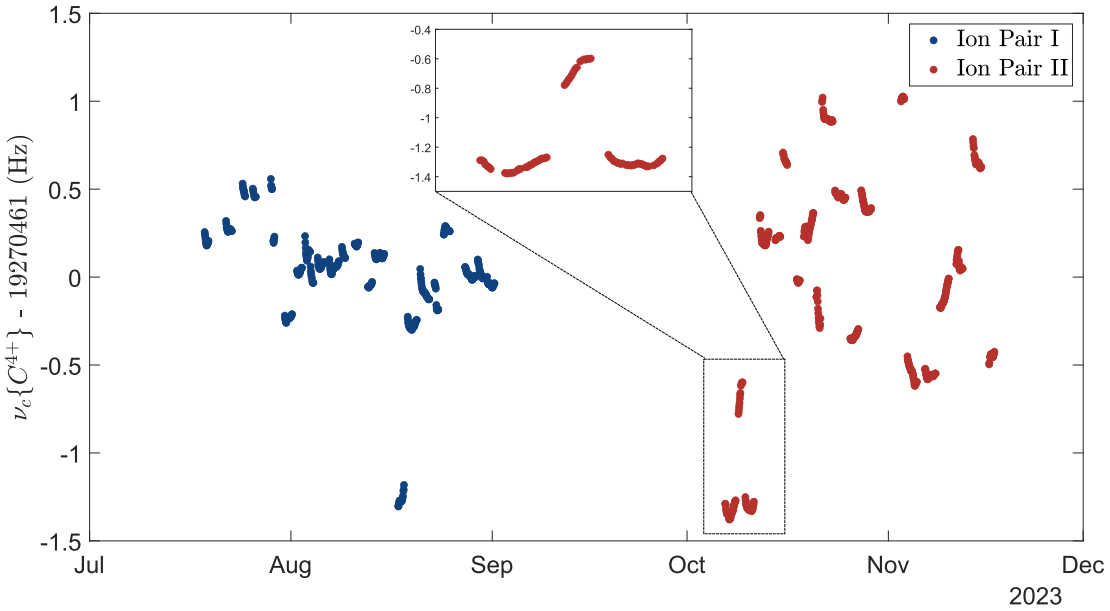

Figure 6.15. Drifts of the magnetic field. Plotted are the cyclotron frequencies of $^{12}C^{4+}$ throughout the measurement campaign, corrected for the PnA excitation energy. Blue and red datapoints denote ion pairs I and II, respectively. ν_c scatters within about 2 Hz, corresponding to $\delta B/B \approx 1 \cdot 10^{-7}$. A linear drift characteristic to freshly charged magnets is not visible. The inset shows a zoom-in to a part of the data. The magnetic field jumps in the gaps between runs where filling occurs, and otherwise exhibits smooth drifts.

of the used PnA cycles for two ions are apart approximately 1/4 of the total time of a measurement cycle [58]. Taking this into account, one arrives at the magnetic field drift of approximately $\delta B/B \approx 1 \cdot 10^{-10}$ between the measurements of helium and carbon. Since the order of ions is randomised during the campaign, the effect doesn't lead to a systematic shift, but results in jitter of the cyclotron frequency ratio:

$$\left(\frac{\delta R_{CF}}{R_{CF}}\right)_{\text{magn drift}} \approx 1 \cdot 10^{-10}. \tag{6.30}$$

6.7.3 Voltage Drifts

Voltage drifts have been discussed in the context of systematic uncertainties caused by the axial frequency determination, see Sec. 6.5.6. They can also play a role in the statistical precision of the cyclotron frequency ratio, however, the effect is largely suppressed by the invariance theorem. Moreover, if the voltage change happens only during the transport, there is no effect on the cyclotron frequency ratio, because the modified cyclotron frequency is changed accordingly. The typical drift of axial

frequency between measurement cycles is 35 mHz for carbon and 30 mHz for helium. The similarity of these numbers, combined with the fact that the dip width for two ions differs by a factor of 6, hints that these drifts are caused by voltage drifts. Considered uncorrelated, the drifts of axial frequency lead to a jitter of the frequency ratio:

$$\left(\frac{\delta R_{CF}}{R_{CF}}\right)_{\text{voltage drift}} \approx 6.2 \cdot 10^{-11}. \tag{6.31}$$

6.7.4 Conclusion on the Limitations and Possible Improvements

The main contributions to the statistical precision of the R_{CF} have been considered in this chapter - the resolution of the PnA, magnetic and electrical field drifts. Assumed uncorrelated and summed in squares, they result in total expected jitter $(\delta R_{CF}/R_{CF})_{\text{tot}} \approx 2.4 \cdot 10^{-10}$ for $r^{+}_{exc} = 14.6$ µm, which is only slightly lower than the measured $(\delta R_{CF}/R_{CF})_{\text{measured}} = 2.5 \cdot 10^{-10}$. There are several possible ways of improving the achievable precision. The elimination of the feedback delay problem during the PnA cycle would result in a slightly increased PnA resolution: $(\delta R_{CF}/R_{CF})_{\text{PnA, 14.6 µm}} = 1.2 \cdot 10^{-10}$.

Further improvements of the PnA resolution would be possible by decreasing the temperature of the ion. This would allow the usage of lower excitation amplitudes due to reduced phase imprinting jitter $\delta\varphi_{\text{therm}}$ and result in the lower relativistic shift. The temperature can be reduced, for example, by utilisation of the cyclotron resonator in order to resistevly cool the modified cyclotron motion of an ion down to 4 K. It is challenging to achieve a high Q-value (and thus low cooling times) at the cyclotron frequency with classical helical resonators. Besides, the Q-value can unpredictably vary inbetween cooldown phases due to potential imperfections in the wiring and different meterial compressibilies in the design. To bypass this problem and lower the form factor of cyclotron resonators, a new planar coil design was developed and implemented at the ALPHATRAP experiment [95]. The new design uses the high temperature Yttrium-Barium-Copper-Oxide (YBCO) superconductor, which can be deposited as a thin film on wafers and different substrates. This makes it possible to use lithographical methods to construct a planar coil and ensure reproducibility of the coil parameters. In addition to the resonator, a largely tunable mechanical varactor (LTMV) has been designed, allowing the adjustment of the cyclotron resonator frequency in larger range without a significant loss in the Q-value of the system [96].

Further improvements in the statistical precision of the experiment can be achieved by improving stability of the magnetic field. The superconducting magnets exhibit a shielding effect, since external field changes are partially compensated by the coils

inside the magnet [97]. Additional superconducting self-shielding coil, wound around, for example, the trap chamber, can strongly suppress the effect of external magnetic field fluctuations in the trap [98]. Another approach is to use a cylinder made from superconducting bulk material instead of a coil. For example, the trap chamber itself can be made from the NbTi. This makes it possible to screen a large volume within the cylinder, since the magnetic flux is conserved by the currents induced in the cylinder through every closed loop within the shield. Such method was tested at ALPHATRAP, indicating an increase of shielding factor by about 9 [96].

Several experimental improvements can be implemented to decrease systematic and statistic uncertainties associated with axial frequency stability and measurement methods. First of all, implementation of the axial phase sensitive method, investigated in this work, can potentially decrease the measurement time, benefiting the accumulation of the statistical precision. Moreover, the systematic effects, associated with dip measurement, such as lineshape, could be avoided with the corresponding peak detection. Although the phase sensitive method would introduce new systematic effects caused by ions excited amplitude, with the present trap optimisation methods and achievable limits on anharmonisity coefficients, these effects can be well characterised. Apart from measurement technique, more stable voltage sources can benefit the statistical precision if the magnetic stability is improved. The possibility of using ultra-stable (low-noise and low-drift) programmable voltage source based on Josephson junctions (PJVS) is investigated at the µTEX experiment at MPIK [99]. Such sources are presently used in metrology for the voltage standard [100]. In the test measurements where two channels of the voltage supply were measured differentially against each other, the stability of the UM1-14 voltage source was compared to PJVS, indicating that the relative voltage stability of the PJVS is at least a factor of 9 better than the UM1-14 stability at the typical trap voltages and averaging times [101]. Another question of voltage stability concerns the voltage drifts related to the transport of ions, when the voltages on the trap electrodes are changed for a short period of time. This effect has been especially pronounced at the ALPHATRAP setup in the past measurements [102, 103, 96]. Here, two causes of drifts can be considered. First of all, the voltage source can produce a slightly shifted value after internally switching the voltage. In order to bypass this effect, at ALPHATRAP the room-temperature switching unit was implemented, which allowed for switching voltage sources for the transport purpose, leaving the channels of precision voltage source unchanged. However, this implementation didn't show a positive effect on the axial frequency drift observed after transport [104]. Another effect relates to the RC-filters used in the DC electrode biasing wiring for the noise filtering purposes. Here, the capacitors have to

be selected with great care due to the polarization (soakage) effects of the dielectric materials in the capacitor. After a voltage discharge, the charges stored in the dielectric material in a capacitor are partly recovered over minute long time scales. This effect causes a built-up of charges in the poles of the capacitor, which subsequently discharge through the RC filters lines connected to electrodes. The current would therefore cause a voltage drop over the resistance and shift the voltage on the trap electrode. In the room-temperature tests at ALPHATRAP it was shown, that the capacitors of the Polypropylene or PTFE type show favourable behaviour compared to the C0G (NP0) type. This also aligns with the fact, that the voltage drifts were more pronounced at ALPHATRAP, where C0G capacitors were used, than at LIONTRAP, where the PPS (Polyphenylene sulfide) capacitors are used in the filters.

Finally, a large improvement in the achievable precision can be realised with the two-ion balance method. It was initially developed at MIT [105, 106], and later implemented for the cyclotron frequency ratio measurements of H_2^+ and D^+ in FSU [34] and measurements of g-factor difference of $^{20}Ne^{9+}$ and $^{22}Ne^{9+}$ isotopes at MPIK [90]. There, two ions are co-trapped at one common magnetron orbit. That way, the magnetic field fluctuations can be strongly suppressed in the measurement of the cyclotron frequency ratio of two ions, since the two ions are only separated by a few hundred µm and magnetic field fluctuations are highly correlated in such configuration. The schematic of ions motion on a common magnetron orbit is depicted in Fig. 6.16. The Coulomb interaction between two ions results in mixed coupled magnetron mode consisting of two collective modes, common mode and separation mode. The radius of the common mode ρ_{com} is the distance between the centre of mass of two ions system and the electrostatic centre of the trap, and ρ_{sep} is the separation distance between ions. These amplitudes are approximately constant in time for ions with similar masses, and a residual modulation depends on the mass mismatch. Therefore, this method is suitable for the ion pairs with similar masses. However, if the masses are too close, it gets complicated to individually address the axial and modified cyclotron motion of the two ions, which are also too close. Moreover, the Coulomb interaction results in the resonant coupling of the cyclotron motions leading to significant frequency shifts. At LIONTRAP, where the mass measurements of light ions are performed relative to carbon ion, the main challenge of the technique arises from the large mass mismatch and subsequent significant modulation of the ρ_{com}. The method was, however, tested in our setup with the $^{12}C^{6+}$ and $^{14}N^{7+}$ ion pair as a proof of principle [59]. Two ions were parked on the common magnetron orbit and the simultaneous PnA measurement tested, indicating that the relative precision of about 3×10^{-12} is possible to achieve within a few hours of measurement, which is a significant improvement compared to

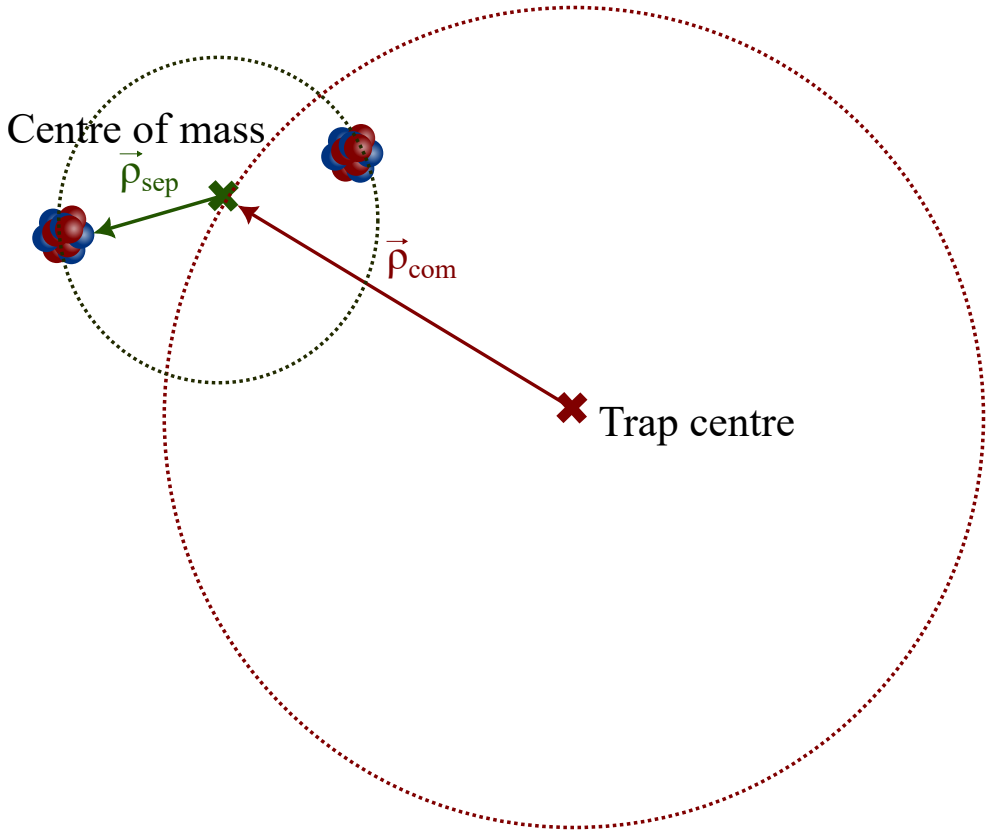

Figure 6.16. The coupled magnetron motion of the two ions in the trap. The scheme shows two ions parked with a non-zero common mode marked red, which results in each ion moving in and out of the trap centre. The green vector shows the separation radius ρ_{sep} between two ions. The ideal configuration for the cyclotron frequency ratio measurement is achieved at $\rho_{com} = 0$ and can be reasonably approximated if the mass difference of two ions is small: $\Delta m/m \leq 10^{-3}$ [59].

a traditional shuttling technique. However, further tests are needed to develop an unambiguous preparation of the coupled ion system and characterization of the related systematic effects.

Chapter 7

Discussions

The mass measurement of helium-3 concluded the series of measurements on light ion species performed at the mass spectrometer LIONTRAP. In the course of its existence (almost 10 years), the experiment has produced high-precision values for the masses of the proton, deuteron, HD, alpha particle, and, within this work, ^{3}He. With that, the experiment in Mainz has concluded and has been moved to Heidelberg, MPIK, where it has been largely repurposed for a new experiment.

In this final chapter, I present the result of the ^{3}He mass measurement campaign together with previous results from our group in the context of the 'Light Ion Mass Puzzle' - the discrepancy among the masses of ^{3}He obtained from various mass spectrometers, introduced in Ch. 1. Additionally, I briefly review the precision mass measurements of light ions planned at another Penning-trap mass spectrometer at MPIK - PENTATRAP. Lastly, I introduce a new Penning-trap experiment at MPIK - LSYM. This experiment has inherited a significant amount of hardware, most notably the cryogenic magnet, as well as experimental techniques developed at LIONTRAP, for the purpose of performing high-precision tests of lepton matter/antimatter symmetry.

7.1 Light Ion Mass Puzzle

The mass of the helium-3 nucleus, measured in this work relative to carbon, is the last missing link in the "Light Ion Mass Puzzle" and the primary candidate for the remaining discrepancy in the masses of the proton, deuteron, and helium-3, as presented in Ch. 1. This inconsistency is visualised by the variation in the mass combination $\Delta = m_p + m_d - m_{he}$ measured by different experiments and is visually represented in Fig. 7.1.

The bands on the left side of the figure represent different measurements from the FSU group [27, 32, 28], which exhibit mutual consistency. The data points on the right

side correspond to measurements performed directly against carbon - a combination of results from LIONTRAP [6, 7] and UW [29, 30]. The diagram on the right indicates the group responsible for measuring the mass of the respective ion in the combination Δ.

Analysis of various measurements suggests that the results from LIONTRAP and FSU are mutually consistent but deviate from those obtained by the UW group. This interpretation is further supported by the measurement of the mass of ^{4}He, which, although not directly part of the puzzle, follows the same trend [8].

It is worth pointing out that the gradual reduction in the absolute difference between the results of the FSU group and the 'carbon' experiments, observed when sequentially replacing the UW measurements with those of LIONTRAP, is a non-trivial consequence of the fact that the discrepancies between the UW and LIONTRAP results do not always have the same sign. While the masses measured by LIONTRAP of the proton [6] and deuteron [7] are lighter than those reported by the UW group, the mass of ^{3}He (as well as that of the α-particle [8]) is higher.

The UW mass spectrometer was moved to Germany, MPIK, in 2008, and its magnet was repurposed for the experiment now known as µTex. After such a long time, it is difficult to pinpoint potential issues with the results of the UW group. In their measurements, R_{CF} was determined by sweeping a weak continuous dipole drive across the cyclotron resonance and observing the drive frequency at which excitation occurred. Excitation of the cyclotron mode was detected by monitoring the resulting shift in ν_z in a slightly anharmonic trap. The axial frequency was made dependent on the cyclotron radius by detuning the trap to produce a nonzero C_4. The ion's axial motion was continuously driven on a sideband and phase-locked to a stable oscillator. The cyclotron excitation was detected as a shift in the phase-error signal. The cyclotron frequency was swept in both directions across the resonance, and ν_c was obtained by extrapolating the shift in phase error for both sweeps to their crossing point. The axial frequency, ν_z, was determined by the frequency of the reference oscillator to which the axial motion was phase-locked.

After the experiment was moved to MPIK, the first measurements were carried out in 2009. However, due to a number of technical difficulties, the measurement technique was never tested with sufficient precision necessary to quantify and resolve potential problems [107]. In modern precision Penning-trap mass spectrometers, field anharmonicities such as B_2 and C_4 are avoided and minimized to ensure the absence of frequency shifts. More advanced trap designs allow for the compensation of electrostatic anharmonicities to a high degree, and compensation coils are used to minimize B_2 components. The characterization of residual anharmonicities ensures the absence

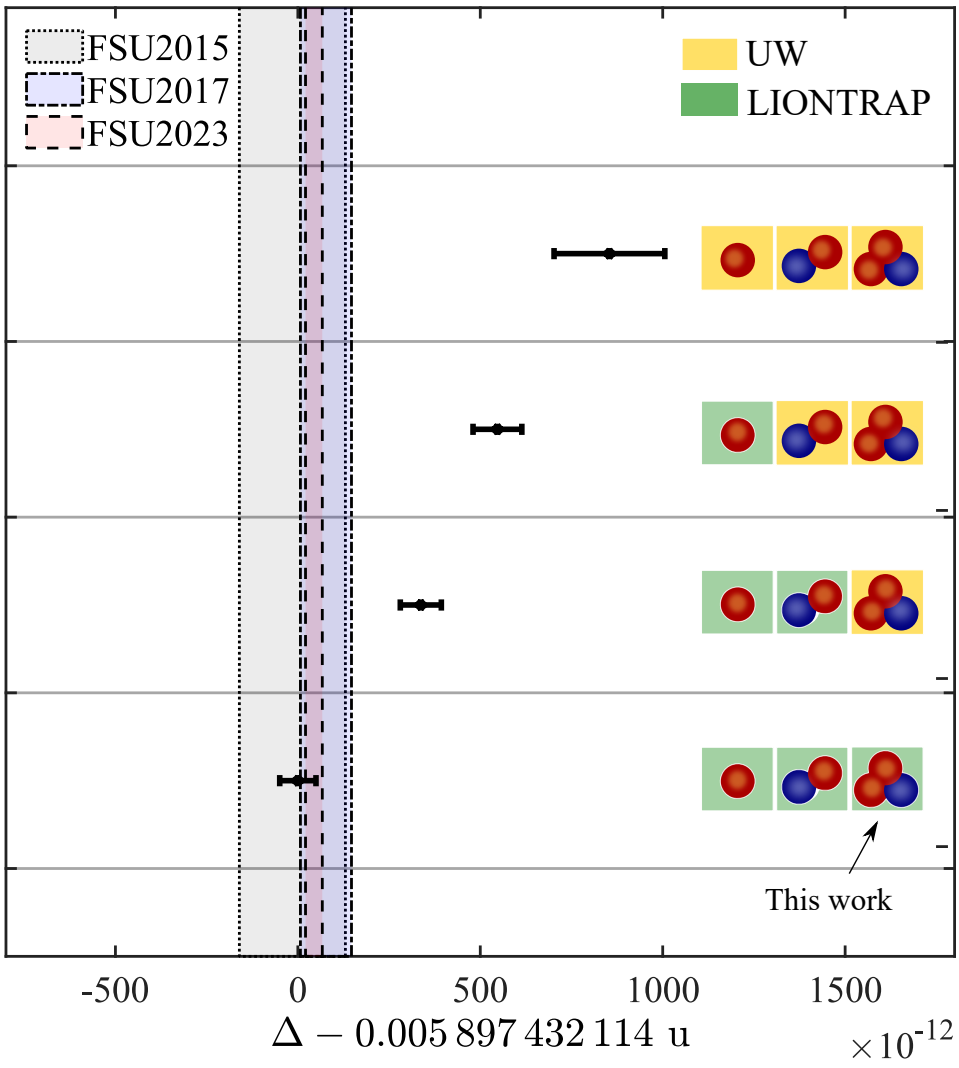

Figure 7.1. The value of $\Delta = m_p + m_d - m_{he}$, obtained by different groups. Points with error bars represent the measurements with ^{12}C as a reference ion. The diagram on the right side indicates the group, which measured the mass of the respective ion (yellow - UW [29, 30], green - LIONTRAP [6, 7]). Grey, blue and red bands are results of the FSU group from 2015, 2017 and 2023, respectively [27, 32, 28]. The combination of m_p, m_d [31, 7] and m_{he}, measured in this work, is in agreement with the FSU group's results within 1 σ.

of unwanted systematic shifts.

The results of this work, which enabled the resolution of the ion mass puzzle, illustrate the consistency of the LIONTRAP results. This is further supported by the measurement of the HD molecular mass, which confirmed the consistency of the proton and deuteron results. Additionally, a reasonable agreement with spectroscopy experiments, which use an entirely different technique, strengthens confidence in the Penning-trap values.

Nevertheless, independent measurements are required to further validate these findings. For example, new measurements of the α-particle mass are planned at the FSU experiment using ratio measurements of ^{4}He to the D_2 molecule [108]. Furthermore, measurements of helium-4 against carbon are planned at the PENTATRAP experiment - a Penning-trap spectrometer at MPIK, which until now has focused on heavy-ion systems and is currently being prepared for light-ion measurements at the ppt level of precision, as discussed in the next section.

7.2 Light Ion Mass Measurements at Pentatrap

The PENTATRAP [109] experiment is a five-Penning-trap mass spectrometer at the MPIK. Its primary focus until recently has been on long-lived highly charged ions. Among the measurements performed with this setup are determinations of long-lived low-lying metastable electronic state in $^{208}Pb^{41+}$[110], masses of $^{20}Ne^{9+}$ and $^{22}Ne^{9+}$[111], mass of ^{238}U[112] and mass ratios of Yb^{42+}[113]. All of these measurements were performed with relative uncertainties at the ppt level, making them one of the most precise relative mass measurements to date.

Since the setup is designed for highly charged ions, it has the advantage of facilitated ion production, namely a broader selection of desired species, as the experiment is online with external EBIT sources. The ions extracted from the EBITs are selected according to the desired charge-to-mass ratio using a 90° bender magnet and transported through the beamline to the Penning traps.

On the other hand, unlike the nearly perfect vacuum of the sealed LIONTRAP setup, this configuration imposes limitations on the achievable vacuum and, consequently, on ion storage times, which are restricted by charge exchange with residual gas atoms. For example, in recent campaigns, the ion lifetime was limited to two days [94]. In the newly installed iteration of the cryogenic setup, vacuum conditions are expected to improve by installing a cryovalve to separate the cryogenically cooled trap from the room-temperature beamline [114].

Another upgrade required for working with lighter systems is the implementation

of cyclotron cooling to reduce the shift caused by relativistic mass increase. Until now, coupling the ions' cyclotron motion to the axial motion, which is cooled to an effective detector temperature of 7(2) K, has been sufficient to achieve a shift of $\mathcal{O}(10^{-13})$ in R_{CF} and the corresponding uncertainty [94]. However, for ^{4}He, this temperature would result in a shift of $\mathcal{O}(10^{-12})$. To address this, the implementation of electronic feedback is planned at PENTATRAP to achieve $T_z \approx 1$ K.

Lastly, alongside the phase-sensitive PnP method that has been used at PENTATRAP until now, the PnA measurement scheme is being implemented to achieve a high SNR of the detected signal for relatively low excitation amplitudes [114].

7.3 New Penning Trap Experiment - LSYM

At the beginning of 2024, the helium-3 measurement campaign was completed. The experimental lab was relocated from the Institute of Mainz to MPIK in Heidelberg. The most exciting part of the process was discharging the magnet for transportation. The magnet had been charged in 1995 and had not been recharged since. With the help of a specialist on NMR Oxford Instruments Magnets, Andy Hield, the magnet was safely discharged, transported to MPIK, and subsequently recharged to $B \approx 5$ T.

At MPIK, a new experiment, LSym, led by Prof. S. Sturm, has been established to perform g-factor and charge-to-mass ratio comparisons of the electron and positron. With a targeted fractional precision of $5 \cdot 10^{-14}$, the experiment aims to provide a stringent test of CPT symmetry in the lepton sector [115].

The idea of the experiment is to simultaneously co-trap positron e^+ and electron e^- in one Penning trap and measure the difference of their spin precession (Larmor) frequencies ω_L. From that, the ratio of the g-factors and charge-to-mass ratios can be probed:

$$\omega_L^- - \omega_L^+ \approx \omega_L^- \left[\left(-\frac{q_e^-}{m_e^-} \frac{m_e^+}{q_e^+} - 1 \right) + \frac{g_e^- - g_e^+}{g_e^-} \right]. \tag{7.1}$$

Since e^- and e^+ have opposite charges, an electron bound to a helium-4 nucleus will be used instead of a free electron to enable co-trapping in the same electrostatic potential. The associated shifts to the electron's g-factor, and therefore ω_L^-, can be calculated from quantum electrodynamics (QED) theory to the targeted precision. The spin precessions of both particles (in the same magnetic field) exhibit a slow beat, which can be accurately measured using a dual-Ramsey measurement sequence. This sequence projects the coherent beat frequency onto the correlation of the spin quantum states of the two particles. Any deviation of this beat frequency from the theoretical prediction would indicate a CPT violation.

For the positrons, a ^{22}Na β^+ emitter placed outside the trap chamber will serve as the source. The first tests with the original LIONTRAP trap tower successfully demonstrated positron trapping [116].

One of the main experimental challenges of LSym is the large relativistic shifts affecting the light positron. To mitigate this, the positron should be cooled to the ground state of both cyclotron and axial motion. This will be achieved by cooling the trap chamber and, subsequently, a special cavity trap to below 400 mK using a commercially available 300 mK refrigerator. The particles in the trap will thermalize to the black-body temperature, and their axial motion will be cooled via the cavity-assisted sideband cooling technique.

7.4 Outlook

In this thesis, I have detailed the experimental modifications, measurements, and analytical techniques that led to the precise determination of the atomic mass of helium-3. The experiment has been upgraded resulting in succesfull production of ^{3}He ions for the first time in the setup of the LIONTRAP experiment. Additionally, a new detection system with improved characteristics has been installed. A new analysis approach was introduced that effectively suppressed the dominant systematic lineshape effect by factor of more than 100. Additionally, a phase-sensitive technique for measuring the axial frequency was developed, showing potential for improving the statistical precision of next generation Penning-trap experiments.

With a relative uncertainty of 12×10^{-12}, this measurement is the most accurate helium-3 mass determination to date. It effectively resolves the 'Light Ion Mass Puzzle', which highlights inconsistencies in the measured masses of light nuclei, such as proton, deuteron, and helium-3, as reported by different Penning-trap mass spectrometers in the past.

By establishing consistency between the results from LIONTRAP and those from the Florida State University group, while identifying discrepancies with the measurements from the University of Washington, this work suggests that the latter may have underestimated the uncertainties in their results. Consequently, the findings of this thesis contribute to restoring confidence in Penning-trap mass spectrometry of light ions, whose masses serve as fundamental constants for testing the Standard Model.

Publications

[1] O. Bezrodnova, S. Sasidharan, W. Quint, S. Sturm, and K. Blaum. "Penning-trap mass measurement of ^{3}He". In: *Phys. Rev. A* 111 (4 Apr. 2025), p. L040801.

[2] S. Sasidharan, O. Bezrodnova, S. Rau, W. Quint, S. Sturm, and K. Blaum. "Penning-Trap Mass Measurement of Helium-4". In: *Phys. Rev. Lett.* 131 (9 Aug. 2023).

Bibliography

[3] Mary K. Gaillard, Paul D. Grannis, and Frank J. Sciulli. "The standard model of particle physics". In: *Rev. Mod. Phys.* 71 (2 Mar. 1999), S96–S111.

[4] Edmund G. Myers. "Progress in High-Precision Mass Measurements of Light Ions". In: *Atoms* 12.2 (2024). ISSN: 2218-2004.

[5] E. G. Myers. "High-precision atomic mass measurements for fundamental constants". In: *Atoms* 7 (2019).

[6] F. Heiße, S. Rau, F. Köhler-Langes, W. Quint, G. Werth, S. Sturm, and K. Blaum. "High-precision mass spectrometer for light ions". In: *Phys. Rev. A* 100 (2 Aug. 2019), p. 022518.

[7] S. Rau et al. "Penning trap mass measurements of the deuteron and the HD^+ molecular ion". In: *Nature* 585 (2020).

[8] S. Sasidharan, O. Bezrodnova, S. Rau, W. Quint, S. Sturm, and K. Blaum. "Penning-Trap Mass Measurement of Helium-4". In: *Phys. Rev. Lett.* 131 (9 Aug. 2023), p. 093201.

[9] S. G. Karshenboim and V. G. Ivanov. "Quantum electrodynamics, high-resolution spectroscopy and fundamental constants". In: *Appl. Phys. B* 123 (2017), p. 8.

[10] S. Sturm, F. Köhler, J. Zatorski, A. Wagner, Z. Harman, G. Werth, W. Quint, C. Keitel, and K. Blaum. "High-precision measurement of the atomic mass of the electron". In: *Nature* 506 (2014), pp. 467–470.

[11] Eite Tiesinga, Peter J. Mohr, David B. Newell, and Barry N. Taylor. "CODATA recommended values of the fundamental physical constants: 2018". In: *Rev. Mod. Phys.* 93 (2 June 2021), p. 025010.

[12] J. Zatorski, B. Sikora, S. G. Karshenboim, S. Sturm, F. Köhler-Langes, K. Blaum, C. H. Keitel, and Z. Harman. "Extraction of the electron mass from g-factor measurements on light hydrogenlike ions". In: *Phys. Rev. A* 96 (1 July 2017), p. 012502.

[13] M. Müller. Personal Communication. Jan. 2025.

[14] E.G. Kessler Jr, M.S. Dewey, R.D. Deslattes, A. Henins, H.G. Börner, M. Jentschel, C. Doll, and H. Lehmann. "The deuteron binding energy and the neutron mass". In: *Physics Letters A* 255.4 (1999), pp. 221–229. ISSN: 0375-9601.

[15] Y. Fukuda et al. "Evidence for Oscillation of Atmospheric Neutrinos". In: *Phys. Rev. Lett.* 81 (8 Aug. 1998), pp. 1562–1567.

[16] Q. R. Ahmad et al. "Direct Evidence for Neutrino Flavor Transformation from Neutral-Current Interactions in the Sudbury Neutrino Observatory". In: *Phys. Rev. Lett.* 89 (1 June 2002), p. 011301.

[17] Julien Lesgourgues and Sergio Pastor. "Neutrino Mass from Cosmology". In: *Advances in High Energy Physics* 2012.1 (2012), p. 608515.

[18] A. S. Barabash. *Brief review of double beta decay experiments*. 2017. arXiv: 1702.06340 [nucl-ex].

[19] E W Otten and C Weinheimer. "Neutrino mass limit from tritium β decay". In: *Reports on Progress in Physics* 71.8 (July 2008), p. 086201.

[20] G. Drexlin. "Direct neutrino mass searches". In: *Nuclear Physics B - Proceedings Supplements* 138 (2005). Proceedings of the Eighth International Workshop on Topics in Astroparticle and Undeground Physics, pp. 282–288. ISSN: 0920-5632.

[21] A. De Rujula and M. Lusignoli. "Calorimetric measurements of 163holmium decay as tools to determine the electron neutrino mass". In: *Physics Letters B* 118.4 (1982), pp. 429–434. ISSN: 0370-2693.

[22] M. Aker et al. "Direct neutrino-mass measurement with sub-electronvolt sensitivity". In: *Nature Physics* 18 (2022), pp. 160–166.

[23] M. Aker et al. *Direct neutrino-mass measurement based on 259 days of KATRIN data*. 2024.

[24] A. A. Esfahani et al. "Tritium Beta Spectrum Measurement and Neutrino Mass Limit from Cyclotron Radiation Emission Spectroscopy". In: *Phys. Rev. Lett.* 131 (10 Sept. 2023), p. 102502.

[25] M. Aker et al. "The design, construction, and commissioning of the KATRIN experiment". In: *Journal of Instrumentation* 16.08 (Aug. 2021), T08015. ISSN: 1748-0221. DOI: 10.1088/1748-0221/16/08/t08015. URL: http://dx.doi.org/10.1088/1748-0221/16/08/T08015.

[26] Alexander Marsteller et al. "Operation modes of the KATRIN experiment Tritium Loop System using 83mKr". In: *Journal of Instrumentation* 17.12 (Dec. 2022), P12010.

[27] E. G. Myers, A. Wagner, H. Kracke, and B. A. Wesson. "Atomic Masses of Tritium and Helium-3". In: *Phys. Rev. Lett.* 114 (1 Jan. 2015), p. 013003.

[28] Moisés Medina Restrepo and Edmund G. Myers. "Mass Difference of Tritium and Helium-3". In: *Phys. Rev. Lett.* 131 (24 Dec. 2023), p. 243002.

[29] R. S. Van Dyck Jr., D. L. Farnham, S. L. Zafonte, and P. B. Schwinberg. "High precision Penning trap mass spectroscopy and a new measurement of the proton's "atomic mass"". In: *AIP Conference Proceedings* 457.1 (Jan. 1999), pp. 101–110. ISSN: 0094-243X.

[30] S. L. Zafonte and R. S. Van Dyck Jr. "Ultra-precise single-ion atomic mass measurements on deuterium and helium-3". In: *Metrologia* 52.2 (Mar. 2015), p. 280.

[31] F. Heiße et al. "High-Precision Measurement of the Proton's Atomic Mass". In: *Phys. Rev. Lett.* 119 (3 July 2017), p. 033001.

[32] S. Hamzeloui, J. A. Smith, D. J. Fink, and E. G. Myers. "Precision mass ratio of $^3He^+$ to HD^+". In: *Phys. Rev. A* 96 (6 Dec. 2017), p. 060501.

[33] David J. Fink and Edmund G. Myers. "Deuteron-to-Proton Mass Ratio from the Cyclotron Frequency Ratio of H_2^+ to D^+ with H_2^+ in a Resolved Vibrational State". In: *Phys. Rev. Lett.* 124 (1 Jan. 2020), p. 013001.

[34] David J. Fink and Edmund G. Myers. "Deuteron-to-Proton Mass Ratio from Simultaneous Measurement of the Cyclotron Frequencies of H_2^+ and D^+". In: *Phys. Rev. Lett.* 127 (24 Dec. 2021), p. 243001.

[35] S. Alighanbari, G. Giri, F. Constantin, V. Korobov, and S. Schiller. "Precise test of quantum electrodynamics and determination of fundamental constants with HD^+ ions". In: *Nature* 581 (2020).

[36] Sayan Patra et al. "Proton-electron mass ratio from laser spectroscopy of HD^+ at the part-per-trillion level". In: *Science* 369.6508 (Sept. 2020), pp. 1238–1241. ISSN: 1095-9203.

[37] I. V. Kortunov, S. Alighanbari, M. G. Hansen, G. S. Giri, V. I. Korobov, and S. Schiller. "Proton–electron mass ratio by high-resolution optical spectroscopy of ion ensembles in the resolved-carrier regime". In: *Nature Physics* 17.5 (Feb. 2021), pp. 569–573. ISSN: 1745-2481.

[38] S. Alighanbari, I. V. Kortunov, G. S. Giri, and S. Schiller. "Test of charged baryon interaction with high-resolution vibrational spectroscopy of molecular hydrogen ions". In: *Nature Physics* 19 (2023).

[39] Robert S. Van Dyck, David B. Pinegar, Seth Van Liew, and Steven L. Zafonte. "The UW-PTMS: Systematic studies, measurement progress, and future improvements". In: *International Journal of Mass Spectrometry* 251.2 (2006), pp. 231–242. ISSN: 1387-3806.

[40] C. Smorra et al. "A reservoir trap for antiprotons". In: *International Journal of Mass Spectrometry* 389 (2015), pp. 10–13. ISSN: 1387-3806.

[41] MS. Earnshaw. "On the nature of the molecular forces which regulate the constitution of the luminiferous ether". In: *Camb. Phil. Soc. trans* 7 (1842).

[42] J. Clerk Maxwell. "A Dynamical Theory of the Electromagnetic Field". In: *Philosophical Transactions of the Royal Society of London* 155 (1865), pp. 459–512. ISSN: 02610523. (Visited on 03/17/2025).

[43] John R. Pierce. "Theory and Design of Electron Beams". In: 1954.

[44] Hans Dehmelt. "Experiments with an isolated subatomic particle at rest". In: *Rev. Mod. Phys.* 62 (3 July 1990), pp. 525–530.

[45] D. Wineland, P. Ekstrom, and H. Dehmelt. "Monoelectron Oscillator". In: *Phys. Rev. Lett.* 31 (21 Nov. 1973), pp. 1279–1282.

[46] Robert S. Van Dyck, Paul B. Schwinberg, and Hans G. Dehmelt. "New high-precision comparison of electron and positron g factors". In: *Phys. Rev. Lett.* 59 (1 July 1987), pp. 26–29.

[47] F.M. Penning. "Die glimmentladung bei niedrigem druck zwischen koaxialen zylindern in einem axialen magnetfeld". In: *Physica* 3.9 (1936), pp. 873–894. ISSN: 0031-8914.

[48] Klaus Blaum. "High-accuracy mass spectrometry with stored ions". In: *Physics Reports* 425.1 (2006), pp. 1–78. ISSN: 0370-1573.

[49] K. Blaum, Yu. N. Novikov, and G. Werth and. "Penning traps as a versatile tool for precise experiments in fundamental physics". In: *Contemporary Physics* 51.2 (2010), pp. 149–175.

[50] Lowell S. Brown and Gerald Gabrielse. "Geonium theory: Physics of a single electron or ion in a Penning trap". In: *Rev. Mod. Phys.* 58 (1 Jan. 1986), pp. 233–311.

[51] Gerald Gabrielse. "Relaxation calculation of the electrostatic properties of compensated Penning traps with hyperbolic electrodes". In: *Phys. Rev. A* 27 (5 May 1983), pp. 2277–2290.

[52] Randall D. Knight. "The general form of the quadrupole ion trap potential". In: *International Journal of Mass Spectrometry and Ion Physics* 51.1 (1983), pp. 127–131. ISSN: 0020-7381.

[53] Fouad G. Major, Viorica N. Gheorghe, and Günther Werth. "Charged Particle Traps: Physics and Techniques of Charged Particle Field Confinement". In: Springer Science & Business Media, 2005.

[54] Jochen Ketter, Tommi Eronen, Martin Höcker, Sebastian Streubel, and Klaus Blaum. "First-order perturbative calculation of the frequency-shifts caused by static cylindrically-symmetric electric and magnetic imperfections of a Penning trap". In: *International Journal of Mass Spectrometry* 358 (Jan. 2014), pp. 1–16. ISSN: 1387-3806.

[55] F. Köhler. "Bound-Electron g-Factor Measurements for the Determination of the Electron Mass and Isotope Shifts in Highly Charged Ions". PhD thesis. Heidelberg University, 2015.

[56] J. Goldman and G. Gabrielse. "Optimized planar Penning traps for quantum-information studies". In: *Phys. Rev. A* 81 (5 2010), p. 052335.

[57] Jochen Ketter. "Theoretical treatment of miscellaneous frequency-shifts in Penning traps with classical perturbation theory". PhD thesis. Heidelberg University, 2015.

[58] S. Rau. "High-precision measurement of the deuteron's atomic mass". PhD thesis. Heidelberg University, 2020.

[59] S. Sasidharan. "High-precision atomic mass measurement of helium-4". PhD thesis. Heidelberg University, 2023.

[60] Lowell S. Brown and Gerald Gabrielse. "Precision spectroscopy of a charged particle in an imperfect Penning trap". In: *Phys. Rev. A* 25 (4 Apr. 1982), pp. 2423–2425.

[61] W. Shockley. "Currents to Conductors Induced by a Moving Point Charge". In: *Journal of Applied Physics* 9.10 (Oct. 1938), pp. 635–636. ISSN: 0021-8979.

[62] J. B. Johnson. "Thermal Agitation of Electricity in Conductors". In: *Phys. Rev.* 32 (1 July 1928), pp. 97–109.

[63] H. Nyquist. "Thermal Agitation of Electric Charge in Conductors". In: *Phys. Rev.* 32 (1 July 1928), pp. 110–113.

[64] D. J. Wineland and H. G. Dehmelt. "Principles of the stored ion calorimeter". In: *Journal of Applied Physics* 46.2 (Feb. 1975), pp. 919–930. ISSN: 0021-8979.

[65] Vasant Natarajan. "Penning trap mass spectroscopy at 0.1 ppb". PhD thesis. Massachusetts Institute of Technology, 1993.

[66] S. Sturm. "The g-factor of the electron bound in $^{28}Si^{13+}$: The most stringent test of bound-state quantum electrodynamics". PhD thesis. Johannes Gutenberg-Universität Mainz, 2012.

[67] Ludwig Boltzmann. "Vorlesungen über Gastheorie". In: Leipzig: Johann Ambrosius Barth, 1896.

[68] Eric A. Cornell, Robert M. Weisskoff, Kevin R. Boyce, and David E. Pritchard. "Mode coupling in a Penning trap: π pulses and a classical avoided crossing". In: *Phys. Rev. A* 41 (1 Jan. 1990), pp. 312–315.

[69] M. Schuh et al. "Image charge shift in high-precision Penning traps". In: *Phys. Rev. A* 100 (2 Aug. 2019), p. 023411.

[70] F. Heiße. "High-precision measurement of the proton's atomic mass". PhD thesis. University of Heidelberg, 2019.

[71] B. Schabinger. "Ein Experiment zur Bestimmung des g-Faktors des gebundenen Elektrons in wasserstoff- und lithiumähnlichen mittelschweren Ionen". PhD thesis. Johannes Gutenberg-Universität Mainz, 2011.

[72] A. Wagner. "The g-factor of the valence electron bound in lithiumlike silicon $^{28}Si^{11+}$: The most stringent test of relativistic many-electron calculations in a magnetic field". PhD Thesis. the Ruperto-Carola university of Heidelberg, 2013.

[73] T. Sailer. "Aufbau einer Präzisionsspannungsquelle für das ALPHATRAP-Experiment". Bachelor thesis. Ruprecht Karl University, Heidelberg, 2015.

[74] B Schabinger, J Alonso, K Blaum, G Werth, H-J Kluge, W Quint, M Vogel, and S Stahl. "Towards a g-factor determination of the electron bound in highly-charged calcium ions". In: *Journal of Physics: Conference Series* 58.1 (Mar. 2007), p. 121.

[75] S Sturm, K Blaum, B Schabinger, A Wagner, W Quint, and G Werth. "On g-factor experiments with individual ions". In: *Journal of Physics B: Atomic, Molecular and Optical Physics* 43.7 (Mar. 2010), p. 074016.

[76] Isaura Vázquez, M. Patricia Russell, David R. Smith, and Ray Radebaugh. "Helium Adsorption on Activated Carbons at Temperatures between 4 and 76 K". In: *Advances in Cryogenic Engineering*. Ed. by R. W. Fast. Boston, MA: Springer US, 1988, pp. 1013–1021. ISBN: 978-1-4613-9874-5.

[77] A. Schneider. "Measurement of the g-factors and zero-field hyperfine splitting of $^3He^+$ in a Penning trap". PhD thesis. Heidelberg University, 2022.

[78] R. Haas, S. Lohse, Ch.E. Düllmann, K. Eberhardt, C. Mokry, and J. Runke. "Development and characterization of a Drop-on-Demand inkjet printing system for nuclear target fabrication". In: *Nuclear Instruments and Methods in Physics Research Section A: Accelerators, Spectrometers, Detectors and Associated Equipment* 874 (2017), pp. 43–49. ISSN: 0168-9002.

[79] S. Ulmer, C. C. Rodegheri, K. Blaum, H. Kracke, A. Mooser, W. Quint, and J. Walz. "Observation of Spin Flips with a Single Trapped Proton". In: *Phys. Rev. Lett.* 106 (25 June 2011), p. 253001.

[80] A. Mooser. "Der g-Faktor des Protons". PhD thesis. Johannes Gutenberg-Universität Mainz, 2013.

[81] C. Roux. "High-Resolution Mass Spectrometry: The Trap Design and Detection System of Pentatrap and New Q-Values for Neutrino Studies". PhD thesis. The Ruperto-Carola-University of Heidelberg, Germany, 2012.

[82] Markus Wiesinger. "Sympathetic Cooling of a Single Individually-Trapped Proton in a Cryogenic Penning Trap". PhD thesis. Heidelberg University, 2023.

[83] A.F. Podell. "A functional GaAs FET noise model". In: *IEEE Transactions on Electron Devices* 28.5 (1981), pp. 511–517.

[84] S. Ulmer, K. Blaum, H. Kracke, A. Mooser, W. Quint, C.C. Rodegheri, and J. Walz. "A cryogenic detection system at 28.9MHZ for the non-destructive observation of a single proton at low particle energy". In: *Nuclear Instruments and Methods in Physics Research Section A: Accelerators, Spectrometers, Detectors and Associated Equipment* 705 (2013), pp. 55–60. ISSN: 0168-9002.

[85] H.W.Ott. "Noise Reduction Techniques in Electronic Systems". In: Wiley-Interscience, 1988.

[86] J. Alonso et al. "A miniature electron-beam ion source for in-trap creation of highly charged ions". In: *Review of Scientific Instruments* 77.3 (Mar. 2006), 03A901. ISSN: 0034-6748.

[87] A. Kramida, Yu. Ralchenko, J. Reader, and and NIST ASD Team. NIST Atomic Spectra Database (ver. 5.11), [Online]. [2024, September 16]. National Institute of Standards and Technology, Gaithersburg, MD. 2023.

[88] Peter Mohr, David Newell, Barry Taylor, and Eite Tiesinga. *CODATA Recommended Values of the Fundamental Physical Constants: 2022*. 2024. eprint: 2409.03787.

[89] Simon Rainville, James K. Thompson, and David E. Pritchard. "An Ion Balance for Ultra-High-Precision Atomic Mass Measurements". In: *Science* 303.5656 (2004), pp. 334–338.

[90] Tim Sailer et al. "Measurement of the bound-electron g-factor difference in coupled ions". In: *Nature* 606.7914 (2022), pp. 479–483. ISSN: 1476-4687.

[91] The MathWorks Inc. *MATLAB version: 9.10.0.1602886 (R2021a)*. Natick, Massachusetts, United States, 2021.

[92] Taylor, John R. *An introduction to error analysis : the study of uncertainties in physical measurements*. Sausalito, California: University Science Books, 1997.

[93] F. Köhler, S. Sturm, A. Kracke, G. Werth, W. Quint, and K. Blaum. "The electron mass from g-factor measurements on hydrogen-like carbon $^{12}C^{5+}$". In: *Journal of Physics B: Atomic, Molecular and Optical Physics* 48.14 (2015).

[94] M. Door. "Precision Mass and Mass-Ratio Measurements of Neon and Ytterbium Isotopes for Tests of Fundamental Physics". PhD thesis. Heidelberg University, 2024.

[95] F. Raab. "Designing and Characterization of a Novel Cryogenic Cyclotron Resonator". Bachelor thesis. Heidelberg University, 2022.

[96] J. Morgner. "Stringent Test of Bound-State Quantum Electrodynamics with Highly Charged Tin". PhD thesis. Heidelberg University, 2024.

[97] Gerald Gabrielse and J. Tan. "Self-shielding superconducting solenoid systems". In: *Journal of Applied Physics* 63 (1988), pp. 5143–5148.

[98] Sven Sturm et al. "The ALPHATRAP experiment". In: *The European Physical Journal Special Topics* 227.13 (2019), pp. 1425–1491. ISSN: 1951-6401.

[99] A. Kaiser. "Characterization of an ultra-stable voltage supply and implementation of sympathetic laser cooling for the $^3He^{2+}$ g-factor measurement". PhD thesis. Heidelberg University, 2024.

[100] Ralf Behr, Oliver Kieler, Johannes Kohlmann, Franz Müller, and Luis Palafox. "Development and metrological applications of Josephson arrays at PTB". In: *Meas. Sci. Technol.* 23.12 (2012). ISSN: 124002.

[101] A. Kaiser et al. "Josephson voltage standards as ultra-stable low-noise voltage sources for precision Penning-trap experiments". In: *Applied Physics Letters* 124.22 (May 2024), p. 224002. ISSN: 0003-6951.

[102] Ioanna Arapoglou. "First measurement of the ground-state g-factor of boron-like argon $^{40}Ar^{13+}$ in Alphatrap ". PhD thesis. Heidelberg University, 2019.

[103] Tim Sailer. "Direct Bound-Electron g-Factor Difference Measurement of Coupled Ions at Alphatrap". PhD thesis. Heidelberg University, 2022.

[104] Charlotte König. Personal commuciation. 2025.

[105] S. Rainville. "A two-ion balance for high precision mass spectrometry". PhD thesis. Massachusetts Institute of Technology, 2003.

[106] J. K. Thompson. "Two-Ion Control and Polarization Forcesfor Precise Mass Comparisons". PhD thesis. Massachusetts Institute of Technology, 2003.

[107] C. Diehl. "First mass measurements with the MPIK/UW-PTMS". PhD thesis. Ruprecht Karl University, Heidelberg, 2011.

[108] E. Myers. "Precision mass ratio measurements of light ions at Florida State University". PSAS'2024 - International Conference on Precision Physics of Simple Atomic Systems. 2024.

[109] J. Repp et al. "PENTATRAP: a novel cryogenic multi-Penning-trap experiment for high-precision mass measurements on highly charged ions". In: *Applied Physics B* 107 (2012), pp. 983–996. DOI: 10.1007/s00340-011-4823-6.

[110] Kathrin Kromer et al. "Observation of a Low-Lying Metastable Electronic State in Highly Charged Lead by Penning-Trap Mass Spectrometry". In: *Phys. Rev. Lett.* 131 (22 Nov. 2023), p. 223002.

[111] F. Heiße et al. "High-Precision Determination of g Factors and Masses of $^{20}Ne^{9+}$ and $^{22}Ne^{9+}$". In: *Phys. Rev. Lett.* 131 (25 Dec. 2023), p. 253002.

[112] Kathrin Kromer et al. "Atomic mass determination of uranium-238". In: *Phys. Rev. C* 109 (2 Feb. 2024), p. L021301.

[113] Menno Door et al. "Probing New Bosons and Nuclear Structure with Ytterbium Isotope Shifts". In: *Phys. Rev. Lett.* 134 (6 Feb. 2025), p. 063002.

[114] S. Eliseev. *^{4}He Mass Measurement*. Meeting of the Stored and Cooled Ions Devision at MPIK. Feb. 2025.

[115] F. Raab. "Designing and characterization of a narrow microwave notch filter for the LSYM experiment in the 100 GHz regime". Master's thesis. Ruprecht Karl University, Heidelberg, 2024.

[116] M. Pasinetti. Personal Communication. Jan. 2025.

Acknowledgments

In conclusion, I would like to express my deep gratitude to everyone who made this work possible.

Dear Klaus, it has been an honour working with you all these years, starting from the COVID-19 outbreak when I got stuck in Germany during my Master's internship. With your help, I was able to complete my Master's thesis at MPIK and begin working in Mainz. You created a work environment that felt both secure and friendly, and your positive attitude and availability, despite a heavy workload, are the subject a great source of inspiration among us, your students. Thank you!

Dear Sven, your guidance has been irreplaceable, and I feel very fortunate to have worked with you. Your sharpness of thought, problem-solving approach, and exceptionally deep understanding and passion for the field have been truly inspiring over the years. Your example extends beyond the work environment - most importantly, in your sense of responsibility and clarity of mind. I learned a lot from you and I am truly grateful. Thank you so much!

Dear Yuri Nikolaevich, you were my first supervisor on my physics journey and the one who introduced me to the field. I still remember our first meeting almost ten years ago. You told me that you like to send your students abroad because "*the youth must travel, just like Goethe's Werther*!" Back then, you didn't specify how Werther's journeys ended... Luckily, things turned out somewhat better for me! Although the challenges of living abroad were certainly there, they taught me a lot about self-reliance. I've always admired your perspective on physics - deeply philosophical and intertwined with a love for nature and art. Thank you for everything!

Dear Sangeetha, over these years, I've spent the most time with you - often in the lab - together navigating not only the universal PhD challenges but also those of being international students. You are an incredible person, and I am very grateful to have had you as a colleague and to have you as a friend. Thank you!

Dear Sascha, you were a tremendous help, and I am grateful to have had the opportunity to work with such a talented physicist. Your organized nature and clarity of mind made you an incredible and reliable colleague. I still remember with a smile

your uplifted mood during Friday evening fillings and the many jokes that inevitably followed. Thank you!

I would like to thank my fellow Meenzer physicists from the proton g-factor group - Christian Smorra, Peter Micke, Christian Will, Markus Wiesinger, and Hüseyin Yildiz - for their help with filling the experiment, lending equipment, and all the lunch and corridor discussions we had. Thank you!

I would also like to thank all the members of the *Stored and Cooled Ions* division at MPIK. Meeting you at MATS Days and other group gatherings was always a great joy and inspiration. I am grateful to have met so many talented people.

I feel deeply grateful to have spontaneously and chaotically become part of the great musical band of talented physicists - Spontaneous Emission. I am especially grateful to our front man, Dima Budker, for showing that a passion for music does not have to be sacrificed for a passion for science.

Many friends have supported me along the way. Artur and Vanya, I am incredibly lucky to have you in my life. Without you, life abroad would have felt much lonelier. Dear Jakob, you were a significant part of this journey and a huge inspiration. Your support and care gave me the strength to keep moving forward. I am also grateful to my fellow students from SPbU with whom I have stayed in contact throughout the years - Zoia, Sasha, Maria, Anna, Dima, Pasha, Ilnur, Vlad, and Sergei. I feel fortunate to know people like you. Dear Nico, you are such a bright and inspiring person - thank you for all your support and encouragement. Dear Bastian, thank you for the humbling late-night chess games that helped me stay sane during the final stages of my thesis writing.

Эта работа была бы невозможна без безграничной и безоговорочной поддержки моей семьи. Вы всегда давали понять, что готовы помочь в любой ситуации, независимо от обстоятельств, и что, несмотря на расстояния, вы всегда рядом. Я люблю вас.

List of Figures

List of Tables